

**DEVELOPMENT AND FUNDAMENTAL CHARACTERIZATION OF
A NANO-ELECTROSPRAY IONIZATION ATMOSPHERIC
PRESSURE DRIFT TIME ION MOBILITY SPECTROMETER**

A Dissertation
Presented to
The Academic Faculty

by

Mark Kwasnik

In Partial Fulfillment
of the Requirements for the Degree
Doctor of Philosophy in the
School of Chemistry & Biochemistry

Georgia Institute of Technology

May 2010

**DEVELOPMENT AND FUNDAMENTAL CHARACTERIZATION OF
A NANO-ELECTROSPRAY IONIZATION ATMOSPHERIC
PRESSURE DRIFT TIME ION MOBILITY SPECTROMETER**

Approved by:

Dr. Facundo M. Fernández, Advisor
School of Chemistry & Biochemistry
Georgia Institute of Technology

Dr. Thomas M. Orlando
School of Chemistry & Biochemistry
Georgia Institute of Technology

Dr. Robert L. Whetten
School of Chemistry & Biochemistry
Georgia Institute of Technology

Dr. Boris Mizaikoff
School of Chemistry & Biochemistry
Georgia Institute of Technology

Dr. Ching-Hua Huang
School of Civil & Environmental
Engineering
Georgia Institute of Technology

Date Approved: March 19th, 2010

This is dedicated to...

my father, Bogdan Andrew Kwasnik (deceased)

Thank you for your unconditional love and support.

ACKNOWLEDGEMENTS

First and foremost, I would like to express my gratitude to my advisor, Dr. Facundo M. Fernández, for his guidance and support, whose mentorship has enabled me to grow as a scientist. It has been a privilege for me to have had the opportunity of working under his supervision and learn from his experience. In these 6 years of working with him at Georgia Tech, his wisdom has helped me grow exponentially in this dynamic field. I would like to also thank Dr. Robert Whetten, Dr. Thomas Orlando, Dr. Boris Mizaikoff and Dr. Ching-Hua Huang for their advisement and for serving in my committee.

I am appreciative to the collaborations provided by Dr. Katrin Fuhrer and Dr. Marc Gonin for the assistance in the development and construction of the ion mobility spectrometer. I also value the collaborations with Dr. Kathy Barbeau, Dr. Richard Zare, and Dr. Ignacio Zuleta for their assistance with marine siderophores and guidance in the area of multiplexing and instrumentation, respectively.

I would like to thank Sam Mize of the College of Science Machine Shop as well as Richard Bedell and José Fonts in the Electronic Shop in the School of Chemistry and Biochemistry for their various machining and electronic assistance.

Special thanks goes to all my group members, past and present, for all the insightful discussions and friendships over the past few years: Dr. Christina Hampton, Dr. Leonard Nyadong, Arti Navare, Krystyn Alter-Hall, Glenn Harris, Carrie Pierce, José Perez, Dana Hostetler, Dr. Manshui Zhu, Dr. Asiri Galhena, Joe Caramore, Kristin Johnson, Felicia Yang, Catherine Silvestri, and David Rizzo.

Finally, I will like to thank my family for their unconditional love and support that has helped to make me who I am today including my mom, Jolanta Kwasnik; my dad, Andrew Kwasnik; and my sister, Diane Kwasnik. Most importantly, I would like to express earnest gratitude to my wife, Nicole Kwasnik, for her unwavering love, support, and especially patience that has enabled me to reach this major milestone in my life.

TABLE OF CONTENTS

ACKNOWLEDGEMENTS	iv
LIST OF TABLES	x
LIST OF FIGURES	xi
LIST OF SYMBOLS	xvi
LIST OF ABBREVIATIONS	xviii
SUMMARY	xxi
CHAPTER 1. Ion Mobility Spectrometry	1
1.1. ABSTRACT.....	1
1.2. EARLY DEVELOPMENT OF ION MOBILITY SPECTROMETRY	1
1.2.1. Early Applications of IMS	2
1.2.2. Electrospray Ionization	3
1.2.3. Electrospray and Ion Mobility	5
1.2.4. Recent Advances and Applications in the Field of IMS	7
1.3. DRIFT TIME ION MOBILITY SPECTROMETRY	7
1.3.5. Modes of Operation	13
1.4. ASPIRATION ION MOBILITY SPECTROMETRY.....	16
1.5. DIFFERENTIAL MOBILITY SPECTROMETRY	17
1.6. TRAVELING-WAVE ION MOBILITY SPECTROMETRY	19
CHAPTER 2. Construction of a Prototype Nanoelectrospray Ionization Monolithic Resistive Glass Atmospheric Pressure Drift Time Ion Mobility Spectrometer	21
2.1. ABSTRACT.....	21
2.2. MOTIVATION BEHIND THE MONOLITHIC ION MOBILITY SPECTROMETER DESIGN.....	21

2.3. RESISTIVE GLASS ION MOBILITY SPECTROMETER	24
2.3.1. Instrument Configuration	24
2.3.2. Ion Source Configurations	29
2.3.3. Timing Scheme DTIMS Mode	31
2.3.4. Timing Scheme DTIMS-MS Mode	32
2.4. LABVIEW SOFTWARE FOR DTIMS, MULTIPLEXED DTIMS, AND DTIMS-MS OPERATION	35
2.4.5. Preliminary DTIMS-MS Data.....	41
2.4.6. Minimizing DTIMS-MS Packet Spreading	45
CHAPTER 3. Performance, Resolving Power and Radial Ion Distributions of a Prototype nanoElectrospray Ionization Monolithic Resistive Glass Atmospheric Pressure Drift Time Ion Mobility Spectrometer	47
3.1. ABSTRACT.....	47
3.2. INTRODUCTION	47
3.3. EXPERIMENTAL DETAILS	50
3.3.1. Samples and Reagents.....	50
3.3.2. High Performance Liquid Chromatography.....	50
3.4. RESULTS AND DISCUSSION	51
3.4.3. Temperature Effects in our Prototype DTIMS.....	52
3.4.4. Drift Gas Effects in our Prototype DTIMS	54
3.4.5. Anode-to-Anode Grid Distance Effects in our Prototype DTIMS.....	55
3.4.6. Ion Gate Pulse Width Effects in our Prototype DTIMS	58
3.4.7. Radial Ion Distributions in our Prototype DTIMS.....	61
3.4.8. Application to Commercially-Available Siderophores.....	64
3.5. CONCLUSIONS.....	67
CHAPTER 4. Digitally-Multiplexed nanoElectrospray Ionization Monolithic Resistive Glass Atmospheric Pressure Drift Time Ion Mobility Spectrometer	69

4.1. ABSTRACT.....	69
4.2. INTRODUCTION	70
4.2.1. Multiplexing in Analytical Applications.....	72
4.2.2. Weighing Designs	72
4.2.3. Types of Multiplexing and their Applications	74
4.2.4. Hadamard Multiplexing and the Fellgett Advantage.....	76
4.2.5. Examples of Multiplexing DTIMS and DTIMS-MS.....	82
4.3. EXPERIMENTAL DETAILS	88
4.3.6. Samples and Reagents.....	88
4.3.7. Digital Sequence Generation.....	88
4.3.8. Signal Acquisition and Processing.....	89
4.4. RESULTS AND DISCUSSION	90
4.4.1. Effects of Sequence Construction	91
4.4.2. Effects of Sequence Length and Modulation Width	95
4.4.3. Effects of Concentration on Sequence Performance.....	99
4.4.4. “Extended” Hadamard Sequences.....	101
4.4.5. Comparison of Hadamard and Arbitrary Multiplexing.....	104
4.5. CONCLUSIONS.....	106
CHAPTER 5. Theoretical and Experimental Study of the Achievable Separation Power in a nanoElectrospray Ionization Monolithic Resistive Glass Atmospheric Pressure Drift Time Ion Mobility Spectrometer.	107
5.1. ABSTRACT.....	107
5.2. INTRODUCTION	108
5.3. EXPERIMENTAL.....	111
5.3.1. Samples and Reagents.....	111
5.3.2. Instrumental Conditions.....	112

5.3.3. Variable Voltage Studies.....	112
5.4. RESULTS AND DISCUSSION.....	113
5.4.1. Comparison of Theoretical and Experimental Resolving Power.....	113
5.4.2. Evaluation of Parameters Affecting Separation Power.....	119
5.4.3. Theoretical Evaluation of Factors Affecting Instrumental Performance	123
5.5. CONCLUSIONS.....	130
CHAPTER 6. Conclusions and Outlook.....	132
6.1. ABSTRACT.....	132
6.2. ACCOMPLISHMENTS IN THE DEVELOPMENT AND CHARACTERIZATION OF A MONOLITHIC DTIMS	132
6.3. PROPOSED FUTURE DIRECTIONS.....	135
6.3.1. DTIMS-MS	135
6.3.2. DTIMS INSTRUMENTAL MODIFICATIONS.....	138
6.3.3. MULTIPLEXED DTIMS WORK	139
REFERENCES.....	141
LIST OF PUBLICATIONS	160
VITA.....	161

LIST OF TABLES

Table 2-1 Typical voltages applied to the different regions of the ion mobility spectrometer when utilizing nanoESI and corona discharge ion sources. All voltages reported in kV.....	26
Table 3-1 Resolving powers obtained from nanoESI DTIMS analysis of 15.5 fmol of reserpine showing the effects of varying the anode to aperture grid distance.	56
Table 3-2 Resolving power values recently reported for atmospheric pressure electrospray ion mobility spectrometers built with stacks of ring electrodes.....	60
Table 5-1 Summary of α values for all experimental conditions and ion gate widths reported with a 95 % confidence interval (confidence intervals not calculated for data sets with ≤ 4 points). Alpha values reported as $\times 10^2$ (V/K).	127

LIST OF FIGURES

Figure 2.1 Representation of electric field potential lines generated using both a stacked ring type conventional IMS and a monolithic IMS, and their effects on drag forces exerted on individual ions within the field.....	23
Figure 2.4 Photograph of the resistive glass monolithic ion mobility spectrometer with the protective Faraday cage removed.	27
Figure 2.5 Schematic showing the coupling of the DTIMS to a JEOL AccuTOF-MS.	29
Figure 2.6 Timing scheme used in DTIMS and multiplexed DTIMS modes for synchronizing ion gating and data acquisition using a National Instruments NI-5411 arbitrary waveform generator and a NI-6111 analog-to-digital data acquisition board.....	32
Figure 2.7 Timing scheme used in DTIMS-MS mode for synchronizing ion gating with the JEOL TOF pulser and data acquisition system using a NI-5411 arbitrary waveform generator, a NI-6602 counting board, and a FAST ComTec GmbH p7887 multiple-event time digitizer.....	34
Figure 2.8 Front panel of the VI used to control the arbitrary waveform generator.....	36
Figure 2.9 Wire diagram of the VI used to control the arbitrary waveform generator.	37
Figure 2.10 Front panel of the VI used to control the data acquisition system.	38
Figure 2.11 Wire diagram of the VI used to control the data acquisition system.....	38
Figure 2.12 Front panel of the VI used to control the counting board for generation of the nested triggering schemes required to synchronize the DTIMS ion gate, TOF pulser, and FAST ComTec P7887 TDC for DTIMS-MS.....	40
Figure 2.13 Wire diagram of the VI used to control the counting board for generation of the nested triggering schemes required to synchronize the DTIMS ion gate, TOF pulser, and FAST ComTec P7887 TDC for DTIMS-MS.....	41
Figure 2.14 1-D TOF spectrum collected with the FAST ComTec P7887 of a 1 μ M reserpine solution showing detailed isotopic structure with flight time in ns displayed on the x-axis and total ion counts displayed on the y-axis.	42
Figure 2.15 2-D TOF as a function of the drift time spectrum of a 1 μ M reserpine solution collected with the DTIMS-MS. Flight time in ns is displayed on the	

x-axis, ion counts are displayed on the y-axis, and drift time in ms is displayed on the z-axis.	43
Figure 2.16 2-D TOF as a function of the drift time spectrum of a 1 μ M reserpine solution collected with the DTIMS-MS after vacuum modifications. Flight time in ns is displayed on the x-axis, ion counts are displayed on the y-axis, and drift time in ms ($\times 10^1$) is displayed on the z-axis.	44
Figure 3.1 NanoESI ion mobility spectra produced by analysis of 80.0 fmol of reserpine showing the effect of temperature (155, 125, 95, 65, and 25 $^{\circ}$ C) on drift time and signal intensity of the solvent and reserpine species.....	53
Figure 3.2 NanoESI ion mobility spectra produced by analysis of 40.0 fmol of reserpine showing the effect of N ₂ drift gas flow rates (0.4, 0.77, 1.10 and 1.40 L \cdot min ⁻¹) on drift time and signal intensity of the solvent and reserpine species.	55
Figure 3.3 Typical DTIMS spectra obtained from the injection of a total of 16 fmol of reserpine into the drift tube, observed at anode grid-to-anode distances of 5.0, 1.5, and 0.7 mm. Resolving power values are reported in Table 3-1.	57
Figure 3.4 NanoESI ion mobility spectra produced by analysis of 31.0, 15.5 and 7.8 fmol of reserpine showing the effect of ion gate pulse length (400, 200 and 100 μ s) on the resolving power (indicated by arrows for each peak), for the solvent species (49.4 ms), reserpine (62.2 ms) and reserpine dimer (93.5 ms).	60
Figure 3.5 Radial ion density profiles within the resistive glass drift tube measured using detector plates with various radii and a corona discharge ion source. The inset shows ion density as a function of ion gate widths for different distances from the longitudinal symmetry axis of the spectrometer.....	63
Figure 3.6 NanoESI-DTIMS analysis of solutions containing DFOB and Fe(III)-DFOB. The spectra show the analysis of a blank, 42.0 fmol of DFOB, and 44.0 fmol of the Fe(III)-DFOB complex. The peak at 31.2 ms is a contaminant that is present in the Fe(III) solution, the peak at 57.3 ms corresponds to the Fe(III)-DFOB complex with a resolving power of 45 ms/ms while the peak at 77.6 ms corresponds to DFOB with a resolving power of 41 ms/ms.	65
Figure 3.7 HPLC chromatograms obtained for Fe(III)-DFOB (4.7 min) and DFOB (6.1 min) on a Waters Symmetry C-18 column. The peak at 1.8 min is an unknown compound that we hypothesize is a contaminant from the Fe (III) solution.....	66
Figure 4-1 Conventional SA DTIMS gating sequence and acquired spectrum. The gating sequence is shown with typical values, but these are generally user selectable.....	77

Figure 4-2 A representative multiplexed DTIMS gating sequence. The ion beam is modulated using a pseudorandom sequence (PRS) derived from a Simplex matrix which is applied to the BNG. This is mathematically expressed as a multiplication of the original ion mobility spectra (Ψ) by the Simplex matrix (S_m). The multiplexed spectrum (η) is collected at the detector. The deconvoluted data ($\hat{\Psi}$) is recovered by multiplication of the multiplexed spectrum (η) with the inverse of the Simplex matrix (S_m^{-1}). 81

Figure 4-3 (A) Conventional SA IMS spectrum of a 50 μ M TBA solution with a 0.02 % duty cycle and (B-D) deconvoluted arbitrary IMS spectra from an identical solution representing 3 different 1 % duty cycle A_{4096} sequences. Spectra B and C represent sequences generated by randomly distributed gating events while spectrum D represents a sequence generated by an evenly spaced distribution of the same number of events. 94

Figure 4-4 SNR gains observed for nanoESI of a 50 μ M TBA solution at 400, 200, 50, and 25 μ s ion gates as a function of the percent duty cycle of the ion gating sequence. Longer ion gating events (400 μ s) produced lower overall gains (2.4x) but can be operated in a wider range of duty cycles while maintaining a multiplex advantage while shorter gates (50 μ s) produced higher gains (6.3x) but result in a much narrower range of optimum duty cycles for which multiplexing is advantageous. 97

Figure 4-5 Concentration dependency of the observed multiplexing SNR gains observed for DFOB solutions at concentrations of 5, 25, 50, 100, 200, and 400 μ M as a function of percent duty cycle. Gains were highest for the lowest concentrations of DFOB with 5 μ M solution producing a maximum gain of 5.3x at a 5 % duty cycle. As the molar DFOB concentration was increased the overall SNR gains decreased and the dependence on optimum duty cycle became less pronounced. 101

Figure 4-6 Comparison of spectra obtained for a 5 μ M DFOB solution in (a) conventional signal averaging mode (0.05 % duty cycle), (b) 255-7 and (c) 1023-1 extended Hadamard sequences with 6.2 and 25 % duty cycles, and (d) standard Hadamard S_{2047} (50 % duty cycle). Standard Hadamard multiplexing resulted in a 9.1x SNR gain but suffered from spectral defects (echoes) appearing as a negative peak at 22 ms and a false positive peak at 85 ms. Extended Hadamard multiplexing sequences 255-7 and 1023-1 resulted in lower gains of 3.3x and 5.8x, respectively, but did not generate spectral defects to the same extent as with the standard Hadamard. 103

Figure 4-7 Comparison of the analysis of a 50 μ M TBA (left panel) using (a) conventional, (b) arbitrary, and (c) standard Hadamard sequences and 5 μ M DFOB (right panel) using (d) conventional, (e) arbitrary, and (f) standard Hadamard sequences. The DFOB $[M+H]^+$ peak appears at 75 ms. For both compounds, the SNR gains increase in the order conventional < arbitrary <

standard Hadamard. However, the Hadamard mobility spectrum suffers from spectral defects labeled with an (*). 105

Figure 5-1 Theoretical and experimental resolving power obtained for a 150 μM TBA and TEA solution using 800, 400, 200, and 100 μs ion gate widths and drift voltages in the range 5.84 - 11.58 kV for a 10 mm anode and a 5.0 mm AG distance instrumental configuration. The blue and green traces represent the theoretical R_p for TBA and TEA, respectively, while the red and black traces represent experimentally observed values. 114

Figure 5-2 Theoretical and experimental resolving power obtained for a 150 μM TBA and TEA solution using 800, 400, 200, and 100 μs ion gate widths and drift voltages in the range 5.84 - 11.58 kV for a 10 mm anode and a 0.7 mm anode grid distance instrumental configuration. The blue and green traces represent the theoretical R_p for TBA and TEA, respectively, while the red and black traces represent experimentally-observed values. 116

Figure 5-3 Experimental resolving power obtained for TEA using 800, 400, 200, and 100 μs ion gate widths and drift voltages in the range 5.84 - 11.58 kV for the following instrumental parameters: (black) 10 mm anode, 5.0 mm AG distance, 0.2 $\text{L}\cdot\text{min}^{-1}$ N_2 ; (blue) 10 mm anode, 0.7 mm AG distance, 0.2 $\text{L}\cdot\text{min}^{-1}$ N_2 ; (red) 30 mm anode, 5.0 mm AG distance, 0.2 $\text{L}\cdot\text{min}^{-1}$ N_2 ; (green) 30 mm anode, 5.0 mm AG distance, 1.5 $\text{L}\cdot\text{min}^{-1}$ N_2 . 118

Figure 5-4 Experimental resolving power obtained for TBA using 800, 400, 200, and 100 μs ion gate widths and drift voltages in the range 5.84 - 11.58 kV for the following instrumental parameters: (black) 10 mm anode, 5.0 mm AG distance, 0.2 $\text{L}\cdot\text{min}^{-1}$ N_2 ; (blue) 10 mm anode, 0.7 mm AG distance, 0.2 $\text{L}\cdot\text{min}^{-1}$ N_2 ; (red) 30 mm anode, 5.0 mm AG distance, 0.2 $\text{L}\cdot\text{min}^{-1}$ N_2 ; (green) 30 mm anode, 5.0 mm AG distance, 1.5 $\text{L}\cdot\text{min}^{-1}$ N_2 . 119

Figure 5-5 Chromatographic resolution obtained for an equimolar mixture of TBA and TEA using 800, 400, 200, and 100 μs ion gate widths and drift voltages in the range 6.63 - 11.58 kV for a 30 mm anode configuration employing a drift gas flow rate of 1.5 $\text{L}\cdot\text{min}^{-1}$ N_2 . 121

Figure 5-6 Chromatographic resolution obtained for an equimolar mixture of TBA and TEA using a drift gas flow rate of 0.2 $\text{L}\cdot\text{min}^{-1}$ N_2 , 800, 400, 200, and 100 μs ion gate widths and drift voltages in the range 6.63-11.58 kV for a 10 mm anode, 5.0 mm AG distance (top panel); 10 mm anode, 0.7 mm AG distance (center panel), and a 30 mm anode, 5.0 mm AG distance configuration (bottom panel). 122

Figure 5-7 Measured peak width squared as a function of the diffusion-dependent parameter for ion gate widths of 800, 400, 200, and 100 μs . The top panel shows results for TEA and the bottom panel shows results obtained for TBA. Alpha values are obtained from the slope of each trend line. 125

Figure 5-8 Measured peak width squared as a function of the ion gate width at voltages of 11.6, 10.7, 9.9, 9.1, and 8.3 kV. The top panel shows results obtained for TEA and the bottom panel shows results obtained for TBA. Beta values are obtained from the slope of each trend line..... 129

LIST OF SYMBOLS

A	Ampere
A/D	Analog-to-Digital
A-matrix	Arbitrary Matrix
Da	Dalton
H_n	Hadamard Matrix
Hz	Hertz
I	Current in amperes
i.d.	Internal Diameter
I_n	Identity Matrix
k	Boltzmann constant
K	Ion mobility constant
l_d	Length of drift tube
m	Mass of the drift gas
M	Mass of the ion
m/z	mass-to-charge ratio
N	Number density of the drift gas
o.d.	Outer Diameter
ppm	Parts-Per-Million
Q	Charge in Coulombs
q	Charge on an ion
S_n	Simplex Matrix

T	Absolute temperature
t	Time
t_d	Drift time
t_{diff}	Diffusional broadening of the ion packet
t_g	Initial shape of injected ion packet
V	Applied DC voltage
v/v	volume/volume ratio
w	Temporal peak width at half maximum
w_b	Temporal full peak width at the baseline
α	Alpha
β	Beta
γ	Gamma
Ω	Collisional cross-section

LIST OF ABBREVIATIONS

ADC	Analog-to-Digital Converter
AG	Anode-to-Anode Grid
AIMS	Aspiration Ion Mobility Spectrometry
AP	Atmospheric Pressure
BNC	Bayonet Neill-Concelman
BNG	Bradbury-Nielson Ion Gate
CV	Compensation Voltage
DFOB	Deferoxamine Mesylate
DMS	Differential Mobility Spectrometry
DTIMS	Drift Time Ion Mobility Spectrometry
DV	Dispersion Voltage
ESI	Electrospray Ionization
FAIMS	Field-Asymmetric Waveform Ion Mobility Spectrometry
FFT	Fast Fourier Transform
FT	Fourier Transform
FWHM	Full Width at Half Maximum
GC	Gas Chromatography
HPLC	High Performance Liquid Chromatography
HT	Hadamard Transform
IMS	Ion Mobility Spectrometry

IR	Infrared
LC	Liquid Chromatography
MALDI	Matrix-Assisted Laser Desorption
MCP	Microchannel Plate
MS	Mass Spectrometry
NMR	Nuclear Magnetic Resonance
PEEK	polyetheretherketones
PEG	Polyethylene Glycol
PFI	Programmable Function Interface
PLL	Phase-Locked Loop
PRS	Pseudorandom Sequence
R	Resolution
R_p	Resolving Power
RP	Reduced Pressure
RTSI	Real-Time System Integration
SA	Signal Averaging
SNR	Signal-to-Noise Ratio
TBA	Tetrabutylammonium
TEA	Tetraethylammonium
TOF	Time-of-Flight
TTL	Transistor-Transistor Logic
TWIMS	Traveling-Wave Ion Mobility Spectrometry
UHP	Ultra High Purity

UV-Vis

Ultraviolet-Visible

VIs

Virtual Instruments

SUMMARY

Drift time ion mobility spectrometry (DTIMS) is a rapid post ionization gas-phase separation technique that distinguishes between compounds based on their differences in reduced mass, charge and collisional cross-section while under a weak, time-invariant electric field. Standalone DTIMS is currently employed throughout the world for the detection of explosives,^{1, 2} drugs and chemical-warfare agents. The coupling of IMS to MS (IM-MS) has enabled the performance of time-nested multidimensional separations with high sample throughput and enhanced peak capacity, allowing for the separation of ions not only based on their mass/charge (m/z) ratios, but also their shape. This allows for the elucidation of valuable structural information that can be utilized for determining gas-phase ion conformation and differentiation between closely related ionic species. Over the past decade, these advances have transformed IM-MS applications and instrumental designs into one of the most rapidly growing areas of mass spectrometry.

The work presented in this thesis is aimed at the development and subsequent characterization of a novel high-resolution resistive-glass atmospheric pressure DTIMS, and the application of this prototype DTIMS to the detection of environmentally relevant compounds. A review of the different types of ion mobility spectrometers, their principles of operation, and the advantages and disadvantages of each type are presented in Chapter 1. Chapter 2 describes the design and development of our prototype resistive glass DTIMS. A detailed description of the IMS hardware, including the ion sources, custom-built control computer, pulsing electronics, data acquisition system, and the timing schemes developed to operate the instrument in

standalone DTIMS, multiplexed DTIMS, and IM-MS mode, are presented. Chapter 3 presents an initial characterization of the performance of a prototype resistive glass DTIMS under a wide range of instrumental parameters and also characterizes the radial ion distribution of the ions in the drift region of the spectrometer. Chapter 4 addresses the lack of sensitivity in DTIMS and explores ion trapping and multiplexing methods, introduces the principles of multiplexing and describes an extended multiplexing approach that encompasses arbitrary binary ion injection waveforms with variable duty cycles. Chapter 5 presents a detailed theoretical and experimental study of the separation power of our DTIMS and presents an evaluation of the field homogeneity and the performance of the ion gate.

CHAPTER 1. ION MOBILITY SPECTROMETRY

1.1. Abstract

Ion mobility spectrometry (IMS) is a rapid gas-phase separation technique that distinguishes between compounds based on their differences in reduced mass, charge and collisional cross-section, either directly or indirectly, while under the influence of an electric field. This section provides a review of the historical development of IMS and describes the four main types of ion mobility spectrometers that are in use in present day application: (1) drift-time ion mobility spectrometry (DTIMS), (2) aspiration ion mobility spectrometry (AIMS), (3) differential-mobility spectrometry (DMS), which is also called field-asymmetric waveform ion mobility spectrometry (FAIMS), and (4) traveling-wave ion mobility spectrometry (TWIMS). An emphasis is placed on the DT-IMS type of instrument and a brief introduction to electrospray ionization is also included.

1.2. Early Development of Ion Mobility Spectrometry

The IMS technology, first introduced as plasma chromatography in 1970,³ can trace its origins to mobility theory developed before 1910.⁴ The idea of correlating the amount of time it takes for an ion to travel through a reduced pressure “mobility” cell under a weak, time-invariant electric field, to the identity, mass, and mobility of the ions was developed in the 1960’s. This was the first time a mobility cell was coupled to a mass spectrometer for the purpose of studying ion-molecule reactions.⁵⁻⁷ These initial experiments provided the background for modern day mobility theory employed in IMS.

The demand for an instrument with a rapid response time that could monitor air quality and composition for defense purposes, accelerated the rate of research activity during the Cold War era of the late 1960's. Research performed at the Georgia Institute of Technology and Franklin GNO Corporation helped transform the field of IMS from a highly specialized research area for studying ion reactions at reduced pressures to a highly versatile and rapid atmospheric-pressure analytical technique for vapor phase analysis.⁸ The mass-mobility relationship that was discovered in preliminary IMS work, and the similarity in the operating principle between an IMS and a Time-of-Flight mass spectrometer (TOF-MS), led to the belief that this technology was a "poor man's mass spectrometer." Further research in the area of IMS, especially work utilizing IMS as a detector for gas chromatography (GC), revealed that although IMS cannot replace a MS,⁹ mass-mobility curves can be fitted to provide estimates of masses for unknown analytes.^{10, 11}

Cohen and Karasek introduced the first atmospheric pressure IMS reported in the literature under the name "plasma chromatography" in 1970.³ This introduction was rapidly followed by the release of the first commercial atmospheric pressure IMS built and distributed by Franklin GNO Corporation in 1972.¹² Work by Revercomb and Mason in 1975 expanded the knowledge of mobility theory and led to the development of the fundamental equations of ion mobility that are utilized in modern day IMS.¹³

1.2.1. Early Applications of IMS

Traditionally IMS was utilized as either a stand-alone rapid separation technique,^{13, 14} or as a detector for GC and liquid chromatography (LC)^{15, 16} for

vapor-phase and volatile analytes that were introduced into a heated ionization region equipped with either a radioactive ^{63}Ni or corona discharge ion source. Under these conditions, IMS is uniquely suited for the rapid detection of explosives,^{1, 2} chemical warfare agent degradation products,^{17, 18} narcotics,¹⁹ and environmental pollutants.²⁰ In the 1990's, IMS evolved as an analytical method that was amicable to non-volatile liquid and solid-phase samples with the coupling of electrospray ionization (ESI)^{21, 22} and matrix-assisted laser desorption ionization (MALDI)²³ ion sources to IMS. The utility of these sources has allowed for IMS to be applied to the analysis of proteins, polymers and carbohydrates.

1.2.2. Electrospray Ionization

The concept of electrospray ionization (ESI) was introduced by Chapman^{24, 25} in the late 1930's and later demonstrated in 1968 by Dole.²⁶ The power of ESI was demonstrated in the late 1980's by Fenn and coworkers²⁷⁻²⁹ and Aleksandrov and coworkers.³⁰⁻³² This was a major breakthrough that allowed for the routine analysis of biomolecules, and led to an explosion in popularity of the technique. In conventional ESI, the first step involves the transformation of a sample solution into a charged aerosol. This aerosol undergoes desolvation as droplets migrate against a countercurrent flow of N_2 into the high-vacuum regions of a mass spectrometer or the heated desolvation chamber of an ion mobility cell. The charged aerosol is generated by application of a potential to either the exterior of a conductive capillary, or directly to a solution via a conductive liquid-liquid junction. This potential induces charge separation in the solution and causes

charge to build up and migrate to the tip of the capillary, forming a Taylor cone and causing the ejection of charged droplets.³³

In 1988, John Fenn presented preliminary results at the American Society for Mass Spectrometry's 36th annual conference in San Francisco, detailing the interfacing of ESI with MS for the analysis of peptides and proteins of molecular weight up to 40 kDa.³⁴ The 40 kDa molecular weight limit on samples in solution was overcome by Fenn and co-workers the following year, allowing for samples up to 180 kDa to be analyzed by ESI.

Since the electrospray ionization process requires thorough solvent evaporation, typical ESI solutions are prepared by mixing a volatile organic solvent with water. Small amounts (0.1-1 % v/v) of a weak organic acid such as formic or acetic acid are typically added to the solution to facilitate formation of positively charged ions and to increase the conductivity of the solution. The charged aerosol generated by the Taylor cone is directed into the mass spectrometer, or desolvation region of a mobility cell in a reduced pressure IMS, through an orifice or heated capillary. In the case of an atmospheric pressure IMS, the charged aerosol is sprayed directly into a heated desolvation chamber. As the charged droplets progress on their path and are continually desolvated, a point is reached where the charge inside the droplet exceeds the surface tension holding the droplet together. At this point, droplets become unstable and undergo a process known as Columbic explosion, or Columbic fission, to generate multiple progeny droplets. This charge to surface tension limit is known as the Rayleigh limit. This cycle continues until the droplets are sufficiently desolvated and generate ions following one of two proposed mechanisms: (1) the ion evaporation model, which states that as droplets reach a certain

size, the charge of the ions within the droplet becomes so concentrated that the ions overcome the surface tension holding them within the droplet and are ejected, or “evaporate” from the droplet,³⁵ or (2) the charge residue model, which states that charged droplets undergo evaporation and explosion cycles, resulting in progeny droplets, which finally contain a single analyte molecule per droplet. The remaining solvent eventually evaporates, leaving behind the analyte carrying the charge initially present in the droplet.²⁶ It is believed that both processes occur in parallel and that smaller analytes generate ions by the ion evaporation mechanism, while larger analytes generate ions by the charge residue model.

Electrospray sources are typically operated with flow rates ranging between 0.1 - 1.0 mL/min however, they can also be operated with much lower flow rates. By decreasing the inner diameter of the conductive capillary used in the ESI source, flow rates as low as μL to nL/min can successfully be employed. Micro- and nano-ESI generate much smaller initial droplets; resulting in improved ionization efficiency due to the smaller initial droplet population, improved desolvation, increased tolerance to sample contamination, and a decrease in adduct formation.^{36,37}

1.2.3. Electrospray and Ion Mobility

The use of an ESI source for atmospheric pressure (AP-DTIMS) was first demonstrated by Shumate and Hill in 1989.²¹ Since an AP-DTIMS does not have the multi-stage vacuum system present on most modern mass spectrometers to assist in droplet desolvation and ion formation, modifications to the design and setup had to be made. In their development, a heated drift gas was introduced at the end of the drift tube,

flowing in the opposite direction of the injected ions, to facilitate desolvation. This setup allowed for the successful analysis of semi-volatile analytes by AP-DTIMS.

In 1994, this ESI source design was improved by introducing three further modifications to the ESI AP-DTIMS setup, allowing for analysis of nonvolatile analytes and large biomolecules such as Cytochrome C.²² First, the needle was removed from the desolvation region, reducing neutralization of charged droplets and ions with the walls of the ion mobility cell. Second, they insulated the tip of the electrospray capillary, resulting in an extended voltage range with which a stable spray could be achieved. Third, the electrospray capillary was cooled, eliminating problems associated with solvent volatilization caused by the heated drift gas. An additional modification proposed by Khayamian et al.³⁸ to further improve ionization, was the introduction of an additional gas into the desolvation region of the spectrometer directly before the ion gate. Further advances to the field of ESI-DTIMS were achieved with the implementation of nanoESI DTIMS in 2003.^{39, 40} This provided improved desolvation, an increased tolerance to sample contamination, and a decrease in adduct formation.^{36, 37} It also reduced the need for heated mobility cells and drift gasses, indirectly improving the resolving power of the instrument, due to a lowering of the Brownian motion within the drift space.

The advantage of using nanoESI for DTIMS is that non-volatiles and macromolecules could now be analyzed with ease without the fragmentation of the analyte because of the relative “softness” associated with ESI. This expanded the utility of DTIMS for biomolecule analysis, allowing the study of molecular complexes that have weak noncovalent interactions, such as protein-protein, enzyme-substrate, or protein-ligand complexes ranging in size from 100 Da to more than 1 MDa. Also, because of the

tendency of ESI to multiply charged ions when analyzing compounds with multiple ionization sites such as oligosaccharides, peptides, and proteins, changes in conformation under various experimental conditions could be explored.²²

1.2.4. Recent Advances and Applications in the Field of IMS

For the past decade, there has been a substantial increase in the development of new IMS technologies such as high-resolution instruments⁴¹⁻⁴³ and separations using different drift gas compositions to modify separation factors⁴⁴ enabling the rapid separation of isomeric compounds,^{45, 46} polymeric conformers,⁴⁷ and chiral compounds.⁴⁸ These new technologies can subsequently be coupled to a mass spectrometer for obtaining the elemental composition of unknown samples. Coupling DTIMS to a mass spectrometer adds a semi-orthogonal separation dimension that separates ions not only on their mass/charge (m/z) ratios, but also their shape, allowing for the elucidation of valuable structural information that can be utilized for determining gas-phase ion conformation⁴⁹⁻⁵² and differentiation between closely related ionic species.⁵³ Additionally, the use of IMS in multidimensional separations for comprehensive proteomic⁵⁴⁻⁵⁶ and metabolomic⁵⁷ experiments has led to a better understanding of complex biological systems.

1.3. Drift Time Ion Mobility Spectrometry

Drift time ion mobility spectrometry (DTIMS) is a rapid post-ionization gas-phase separation technique that separates compounds based on their differences in reduced mass, charge, and collisional cross-section under a weak, time-invariant electric field.

DTIMS provides the highest resolving power out of the four methods of ion mobility separation, and is the only method that directly measures collisional cross-sections.

The first types of instruments developed in the 1950's to the 1980's were all drift tube type instruments, and drift time instruments are the most common types of instruments in use today.⁵⁸ DTIMS measures the amount of time it takes an ion packet to migrate through a drift gas while under the influence of a weak, time-invariant electric field. In this type of setup, the amount of energy that is imparted upon the ions as they are “pulled” by the electric field is less than the thermal energy supplied to the ions as they collide with the neutral drift gas molecules. These thermal collisions cause diffusion like processes to dominant the behavior of ion packets within the drift space, with the velocity of the ions being directly proportional to the electric field strength. This relationship is expressed as the ion mobility constant (K), and is inversely proportional to an ion's collisional cross-section (Ω) as shown in Equation 1.1¹³ The parameters in Equation 1 represent the charge of the ion (q), the number density of the drift gas (N), the Boltzmann constant (k), the absolute temperature (T), the mass of the drift gas (m), and the mass of the ion (M)

$$K = \left(\frac{3q}{16N} \right) \left(\frac{2\pi}{kT} \right)^{1/2} \left(\frac{m+M}{mM} \right)^{1/2} \left(\frac{1}{\Omega} \right) \quad (\text{Eq.1.1})$$

Collisions between individual ions and drift gas molecules impede and scatter the motion of the ions within the ion packet as they are pulled through the drift tube resulting in a spreading of the ion packet which leads to a degradation in the resolving power (R_p) of the instrument. The ion separation capabilities of a DTIMS instrument are quantified

using either the resolving power (R_p) or the peak-to-peak resolution (R) definition. Both formalisms are taken from gas chromatography where the resolving power corresponds to the square root of the number of theoretical plates,⁵⁹ and the peak-to-peak resolution is an assessment of the peak separation between two adjacent peaks in the mobility spectrum.

Resolving power (R_p) is the most common formalism used to compare the performance of different DTIMS instruments, both atmospheric pressure and reduced pressure types. R_p is preferred when comparing two instruments because of the arbitrariness of peak-to-peak resolution with different sample mixtures. On the other hand, R is well suited when evaluating the chromatographic conditions that lead to unit resolution ($R = 1$), baseline-resolved peaks ($R = 1.5$), or the minimum acceptable resolution ($1.75 < R < 2.0$).^{60, 61}

IMS R_p is defined as the ratio between the drift time (t_d) and the temporal peak width at half maximum (w) as shown by Equation 1.2.^{62, 63} The peak-to-peak resolution is given by Equation 1.3^{64, 65} where (t_{d1}) and (t_{d2}) are the drift times for two adjacent ions in the mobility spectrum, and (w_{b1}) and (w_{b2}) are the temporal full peak width at the baseline of the same two peaks.

$$R_p = \frac{t_d}{w} \quad (\text{Eq.1.2})$$

$$R = \frac{t_{d2} - t_{d1}}{(w_{b1} + w_{b2})/2} \quad (\text{Eq.1.3})$$

Resolving power can also be related to specific instrumental conditions through simple mobility theory, which states that the drift time is proportional to the length of the drift tube (l_d) and inversely proportional to the drift tube voltage (V) by Equation 1.4. This relationship for drift time can then be substituted into Equation 1.2, resulting in a new equation for resolving power. Equation 1.5 indicates that resolving power of an IMS is improved by increasing the length of the drift tube, although this is not explicitly stated due to the dependence of R_p on w . At first glance, Equation 1.5 indicates that R_p is decreased by increasing the drift potential. Even though an inverse relationship exists between V and R_p , because of the dependence of w on V , which causes w to decrease with increasing V , this assumption is misleading. The relationship between voltage applied to the drift tube and its effect on both R and R_p will be explored further in chapter 5.

$$t_d = \frac{l_d^2}{KV} \quad (\text{Eq.1.4})$$

$$R_p = \frac{l_d^2}{wKV} \quad (\text{Eq.1.5})$$

The shape of a peak is determined by the initial shape of the ion packet injected (t_g) into the drift tube by the Bradbury-Nielson ion gate (BNG)⁶⁶ and any diffusional broadening (t_{diff}) for the ion packet as it travels through the drift space to the detector. (i.e. $w^2 = t_g^2 + t_{\text{diff}}^2$). This simplified equation treats the ion packet as an infinitely narrow pulse so as to account for diffusion and collection of a real ion packet, the t_{diff}^2 parameter was expanded by Revercomb and Mason (Eq. 1.6).¹³

$$t_{diff}^2 = \frac{16 \ln 2 k T t_d^2}{qV} \quad (\text{Eq. 1.6})$$

Even after accounting for diffusion, fitting experimental data to this model consistently underestimated experimental peak widths. Possible reasons for larger than expected experimental peak widths are: (1) electrostatic repulsions of neighboring ions in the initially injected ion cloud,^{67, 68} (2) longitudinal diffusion due to excess energy transferred to the ions by the electric field as they travel through the drift tube,⁶⁷ (3) distortions of the electric field created as the ion gate is pulsed “open” and “closed”,⁶⁹⁻⁷³ (4) distortions in the ion packet periphery cause by inhomogeneous electric fields generate near the segmented guard rings of the mobility cell,⁶³ (5) distortions in the ion packet created by non-uniform fields and image currents generated between the aperture grid and the detector, and (6) contributions from transverse diffusion resulting in an increased drift time of certain portions of the ion cloud.

Some of these theories have been the subject of much debate. For example, Schummers et al. observed that the transverse diffusion coefficient affects only the amplitude of the mobility peak and not its width.^{74, 75} These observations were consistent with work by Mason et al. and the two-temperature model in ion mobility.⁷⁶ Spangler⁷⁷ observed that the ion density was not sufficiently concentrated in the injected ion packet to cause significant electrostatic repulsion effects, and this hypothesis was later supported by Eiceman et al.⁷⁸ This work was controversial, and it was later proven that Coulombic effects play an important role in the behavior of an ion packet as it travels down the drift tube and results in a spatial dispersion of the ions. This distortion is greatly exasperated

for ion populations of $> 10,000$ elementary charges.⁷⁹ Work by Siems et al. calculated that the Townsend energy factor should be approximately 1.0, not 2.7 as proposed by Spangler and Collins.⁶⁷ They hypothesized that the ions should be very close to thermal energies and therefore, any energy transferred to the ions as they travel down the drift tube is negligible.⁶³ Wu et al. were able to dramatically improve their resolving power of their stacked-ring mobility cell by decreasing the ion transmission area of their aperture grid, however, this decrease resulted in a marked reduction in sensitivity.² Work by Albritton et al. theorized that radial inhomogeneities in stacked ring-type DTIMS were negligible, with variations in the 1- 2 % range at the periphery of the drift tube and extending up to 33 % of the internal diameter of the drift tube. These variations were believed to deteriorate rapidly beyond 33 % of the diameter due to the exponential nature of the Bessel function.⁸⁰ Also, work by Carrico investigated the performance of an IMS built with uniformly inlaid ceramic resistors coated with a thick film conductor from DuPont. Their results showed no significant improvement in resolution when compared to a stacked ring drift tube design. This 1st generation monolithic DTIMS instrument was shown to produce inconsistent results. These inconsistencies were believed to originate from changes in resistance of the coating material over time, and may have masked the significance of a homogeneous electric field in the drift region.⁶⁴ Contrary to popular belief at the time, calculations by Siems et al. revealed that radial inhomogeneities contributed significantly to measured peak widths.⁶³ Our 2nd generation monolithic DTIMS built with resistive glass desolvation and drift regions, which has been shown to produce very homogeneous electric fields via Kelvin probe measurements, will be used to evaluate the contributions of radial field inhomogeneities on measured peak widths.

1.3.5. Modes of Operation

A DTIMS instrument can be operated either at atmospheric pressure (AP-DTIMS) or under a reduced pressure (RP-DTIMS) regime. RP-DTIMS was the first type of DTIMS that was developed. In a RP-DTIMS setup, the mobility cell is placed inside the vacuum region of a mass spectrometer, before the mass analyzer. A needle valve is then used to leak in a low, continuous flow of an inert drift gas into the mobility cell until pressures of a few Torr are achieved.^{6, 12, 74, 75} The advantage of RP-DTIMS is that pressures in the mobility cell and the mass analyzer are in similar regimes, which allows not only for thorough desolvation and rapid separations, but also for efficient transfer of ions from the mobility cell to the ion optics of the spectrometer.

An alternate configuration for RP-DTIMS involves mounting the mobility cell after the mass analyzer, where information about the collisional cross-sections of mass selected ions can be acquired.⁸¹⁻⁸³ This configuration allows for the probing of changes in conformation and fragmentation of a mass selected ion under different mobility cell conditions. The selection of specific ions also allows for ion-ion⁸⁴ and ion-molecule⁸⁵ reactions to be performed in the desolvation/reaction region of the mobility cell prior to separation in the drift region of the RP-DTIMS.

Atmospheric pressure (AP-DTIMS) is the mode of operation utilized by stand alone research and portable field monitoring ion mobility spectrometers. AP-DTIMS are employed by the military for rapid screening of battlefields for chemical warfare agents and explosives^{1, 15}. They are also commonly used by airport security personnel to screen not only for warfare agents and explosives, but also for narcotics and other contraband.¹⁹

⁸⁶⁻⁸⁸ Recently, AP-DTIMS has been adopted for rapid screening of pharmaceuticals^{89, 90} as a quality control application to help screen for unknown and unwanted contaminants or reaction byproducts, and also to screen for pharmaceuticals in biological samples such as human serum^{54, 91, 92}. Another application for stand-alone AP-DTIMS is as a detector for GC, LC and supercritical fluid chromatography^{54, 93, 94}

The advantage of AP-DTIMS is that instrument is capable of much greater separation efficiency and produces a much higher resolving power (R_p) when compared to its reduced pressure counterpart. These improvements are a direct result of the increased frequency of interactions of the individual ions within the ion pack with the drift gas molecules. The ion-molecule interactions facilitate greater separation selectivity, however, AP-DTIMS instruments are typically less sensitive than RP-DTIMS, especially when coupled to a mass spectrometer. When coupled to MS, the ions must be transferred from the atmospheric pressure region through a series of orifices and pumped vacuum regions through the ion transfer optics of the MS. This transfer requires a $10^7 - 10^8$ fold pressure reduction to preserving the mean free path of the ions,⁹⁵ in addition to the need for adequate desolvation when working with liquid samples and an electrospray source. This can be achieved by sampling the ions from the center of the atmospheric pressure region at the end of the drift tube directly into high vacuum using either a relatively small orifice (10 - 25 μm) or a very high pumping capacity ($> 100,000$ L/s).⁹⁶ The preferred, but more instrumentally complex approach, uses a multi-stage differential pumping system. In this approach, ions are first drawn into the sampling orifice from the center of the atmospheric pressure region at the end of the drift tube at pressures ≥ 760 Torr into a first chamber that is pumped down to approximately 1 - 4 Torr by a rotary pump. Next,

part of the expanding beam of gas and ions is sampled by a second orifice into a second chamber pumped down to 10^{-3} Torr or less, at which point most of the drift gas and solvent molecules have been pumped away. Finally, the ion optics transfer the desolvated and declustered ions to the mass analyzer region of the MS. Between the loss of ions that occurs because only a small portion of the incoming ion cloud is sampled by the 1st mass spectrometer's orifice, and the less-than-perfect transfer of the sampled ions through multiple ion optics and vacuum regions of different pressures, > 99 % of the initial ions are lost before they can be injected in the mass analyzer.^{41,97}

Both atmospheric pressure and reduced pressure DTIMS instruments typically utilize a continuous ionization source such as ^{63}Ni , corona discharge, photo or electrospray ionization (ESI). However, since DTIMS uses time-domain separations to resolve chemical species, an optical element such as a Bradbury-Nielson ion gate (BNG)⁶⁶ or a Tyndall ion gate⁹⁸ is utilized to inject a discrete packet of ions into the drift region. Once the ion packet reaches the end of the drift tube and is detected, the next gating event is initiated. However, the time scale of these events is disproportionate, with a typical injection time of 25 - 400 μs and a typical analysis time of 25 - 100 ms, resulting in an experimental duty cycle of $\sim 0.04 - 1.0\%$. The sensitivity exhibited by DTIMS is thus limited by this intrinsically low duty cycle.

Although DTIMS is a very powerful technique that can provide a plethora of unique information, especially when coupled to a MS, the lack of sensitivity associated with the technique is a major challenge. Of the ions generated by the ion source, independent of the type of ion source the instrument may be utilizing, only 0.04 - 1.0 % of those ions are ever injected and analyzed by the DT-IMS. This problem is further

compounded when a DTIMS, especially an AP-DTIMS, is coupled to a MS. Of the 0.04 - 1.0 % of the initial ions that are injected into the mobility cell, > 99 % of them are lost before they are detected by the mass analyzer.^{41, 97}

Ion trapping methods utilizing quadrupole and octopole ion traps,^{83, 99, 100} as well as electrodynamic ion funnels¹⁰¹ have been employed to accumulate and inject ions efficiently from the ion source to increase the sensitivity of DTIMS. Multiplexing approaches via Hadamard^{102, 103} and Fourier-type^{88, 104} gating techniques have also been utilized for increasing the sensitivity of DTIMS, by increasing the frequency of ion injection events and thus increasing the quantity of ions injected into the DTIMS.

In chapter 4, we will discuss the different approaches that have been developed to improving DTIMS sensitivity. We will also address the sensitivity issues in DTIMS via a novel multiplexing method developed in our lab that we named “digital multiplexing.” This method is an extended multiplexing approach which encompasses arbitrary binary ion injection waveforms with variable duty cycles ranging from 0.5 to 50%. In this approach, ion mobility spectra can be collected using conventional signal averaging, arbitrary, standard Hadamard and/or “extended” Hadamard operation modes.

1.4. Aspiration Ion Mobility Spectrometry

Aspiration Ion Mobility Spectrometry (AIMS) is a rapid post-ionization gas-phase separation technique used to resolve ionized compounds under atmospheric pressure conditions. In AIMS, ions are continuously injected into the mobility cell with a constant flow of drift gas. The buffer gas containing the ions is directed perpendicular to the direction of the applied electric field. The ions travel with the gas through this transverse

electric field, which forces them towards a number of segmented detector electrodes. In AIMS, ionic species with different ion mobilities are collected on the different detector electrodes. Pattern recognition software is then applied to the measured ion currents of each individual electrode for ion identification. The advantage of AIMS is that the mobility cells are simple to design, inexpensive to fabricate, have small dimensions, and have low power and gas consumption. Also, both positive and negative ions can be monitored simultaneously if the AIMS mobility cell is equipped with two sets of opposing polarity segmented electrodes. The drawback of AIMS is that it suffers from low resolving power, and the pattern recognition software requires “immense training sets” that are instrument and analyte specific.¹⁰⁵ The field of AIMS was greatly advanced with the advent of swept-field AIMS instrumentation.^{106, 107} These types of aspiration condensers use a variable electric drift field to move all ion species across a single detector electrode. A voltage scan with multiple discrete steps is used instead of multiple detector elements. The resulting current vs. voltage plot is then transformed into an ion mobility spectrum by applying a discrete inverse Tammet Transform.¹⁰⁸ This allows for ion identification by determining the location of the peak in the mobility spectrum, similar to peak identification in a DTIMS spectrum, and eliminates the need for pattern recognition to identify unknowns. AIMS are sold commercially under the trade name IMCell.

1.5. Differential Mobility Spectrometry

Differential mobility spectrometry (DMS), also known as field-asymmetric waveform ion mobility spectrometry (FAIMS), is a rapid atmospheric pressure

post-ionization gas-phase separation technique. DMS is related to, but fundamentally different from DTIMS. Instead of separating ions based on the collisional cross-section under a time-invariant electric field, DMS separates ions based on changes in the collisional cross-section as the ion clusters and declusters, as a function of electric field strength. In DMS, ions are continuously injected into DMS, similar to AIMS. A buffer gas is then mixed with the ions before they are introduced into the mobility cell of the DMS. This buffer gas containing the ions is passed between either two flat parallel electrodes, or two concentric cylindrical electrodes.¹⁰⁹ Both planar and coaxial geometries have been implemented in commercial products: planar “SVAC” by Sionex and coaxial “Selectra” by Thermo Fisher. Unlike an AIMS mobility cell, the electrodes are not segment and an alternating step wise electric field is generated between the two electrodes. The alternating electric field causes ions to move perpendicular to the flow of gas in alternating directions. Ion movement favors one of the electrodes, depending not only on the properties of the ion, but also on the properties of the ion-ion clusters.¹¹⁰ The separation field in a DMS must be such that its average value over a full stepwise waveform sweep, or period, is zero. However, the positive half-period of the sweep is not equal in intensity, or amplitude, to the negative half-period of the waveform. For example, in one direction the field is twice as strong, but is applied only for half the time it is applied in the opposite direction.¹¹¹ Unlike DTIMS, the high electric field generated between the two electrodes is such that the ionic mobility is no longer directly proportional to the electric field. In this type of setup, the ions undergo fast oscillations in response to the stepwise changes in field strength. The ions experience different displacement during the positive and negative half-period of the waveform because of

unequal mobilities when exposed to alternating high and low-fields, causing the ions to drift, or disperse, toward one of the electrodes according to their differential mobility. Thus, the voltage used to create the asymmetric field is called the dispersion voltage (DV). Ions pass between the two electrodes only if their transverse drift velocity is zero, otherwise they strike one of the two electrodes and are neutralized. Particular ions with similar characteristics can be restored to the center of the two electrodes, with no net drift, by applying a low strength constant compensation voltage (CV) to one of the electrodes. Ions with different differential mobilities can be passed between the two electrodes at a different CV.

A DMS can be operated in one of two ways: (1) the CV can be scanned, which produces a spectrum of all the ions with different mobilities within the ionic mixture, similar to a DTIMS spectrum, with the drift time replaced by the CV value at specific time intervals, or (2) the CV can be left at a constant value during the DV waveform sweep and the DMS will act as a “filter”, only allowing ions of similar mobilities to pass between the plates.¹¹² This “filter” mode of operation is typically used when the DMS is interfaced to a MS to remove background signals and improve the signal-to-noise ratio (SNR).¹¹³ “If the traditional drift-time method for ion mobility spectrometry is analogous to time-of-flight mass spectrometry then the differential-mobility method is analogous to a quadrupole mass spectrometer.”⁵⁸

1.6. Traveling-Wave Ion Mobility Spectrometry

“Traveling-wave” ion mobility spectrometry (TW-IMS) is a rapid reduced pressure post-ionization gas-phase separation technique that has the lowest resolving power of all

the ion mobility approaches. It is a novel method of ion mobility that was introduced by Giles et al.^{114, 115} in 2004 as a radio-frequency-only stacked ring ion guide and was incorporated in a commercial orthogonal acceleration TOF-MS with upfront ion accumulation (Waters Synapt HDMS) in 2007.¹¹⁶ Because of the availability of the TW-IMS on a readily available commercial platform, interest in the field of IMS has grown exponentially over the last few years. The Synapt HDMS has transformed the field of IMS-MS from a niche research field, and has made it attractive for practical routine analyses. Research in areas such as structural biology¹¹⁷⁻¹²⁰ and complex separations of biological¹²¹ and polymer⁸⁵ mixtures are rapidly expanding.

In TW-IMS, a high-electric field is applied to one segment of the mobility cell and swept throughout the mobility cell one segment at a time, in the direction of ion migration. A sequence of symmetric potential waves continually propagating through a “stacked-ring” segmented type mobility cell propels ions along at a velocity that is dependent on the mobility (K), with different species traveling through the tube at different drift times. TW-IMS separates ions similarly to DTIMS, therefore multiple species can be measured simultaneously. This simultaneous analysis provides a major advantage over techniques like DMS and FAIMS, which provide good transmission for select species when operated in “filter” mode, but not in an analysis of a mixture where the CV must be scanned.

CHAPTER 2. CONSTRUCTION OF A PROTOTYPE NANOELECTROSPRAY IONIZATION MONOLITHIC RESISTIVE GLASS ATMOSPHERIC PRESSURE DRIFT TIME ION MOBILITY SPECTROMETER

2.1. Abstract

This chapter describes the design and development of our prototype resistive glass DTIMS. A detailed description of the IMS hardware including the interchangeable nanoESI and corona discharge ion sources, custom-built control computer, pulsing electronics, data acquisition system, and the timing schemes developed to operate the instrument in standalone DTIMS, multiplexed DTIMS, and DTIMS-MS mode coupled to our JEOL TOF-MS are provided. Preliminary DTIMS-MS data collected with the modified ultra-fast multiple-event time digitizer data acquisition system on the JEOL TOF mass spectrometer is also presented.

2.2. Motivation Behind the Monolithic Ion Mobility Spectrometer Design

As with any other separation technique, the ability of ESI-IMS to resolve closely spaced peaks is of paramount importance. In this line of thought, Hill and co-workers studied the effects of several experimental variables on the resolving power of atmospheric pressure IMS. Their results consistently showed that peaks in IMS spectra were wider than predicted, even after accounting for differences in instrument design,

initial pulse width and thermal ion diffusion. In order to rationalize these differences, they proposed that Coulombic repulsions and electric field inhomogeneities within the drift tube were responsible for the lower than ideal resolving powers observed.⁶³

In order to investigate if radial electrical field variations within the ion mobility drift tube can be mitigated by the use of new drift tube building materials, we designed and built a new type of high-resolution atmospheric pressure drift time ion mobility spectrometer based on resistive glass technology. Thus far, almost all ion mobility spectrometers, both designed and developed in the research setting and sold commercially, are based on the same design. They utilize a drift region built with a stack of high precision-machined ring electrodes, each pair separated by insulating spacers and connected through a series of resistors, to generate a uniform potential gradient. In contrast, our prototype is furnished with resistive glass monolithic desolvation and drift chambers. Resistive glass is lead silicate glass that has been reduced in a hydrogen atmosphere to make its surface a semiconductor.¹²² Kelvin probe measurements show that resistive glass produces highly uniform electrical fields.¹²³ It has been proposed that structures and assemblies made from resistive glass can be used as reflectrons,¹²⁴ ion mobility drift cells,¹²⁵ and as a way to control the energy of externally-generated ions prior to injection into miniature ion traps,¹²⁶ but no performance data for a DTIMS has yet been reported in the peer-reviewed literature. The use of resistive glass for building ion mobility spectrometers has four advantages: (1) the radial inhomogeneities in the drift tube electric field are minimized (Fig. 2.1), (2) the construction of the ion mobility spectrometer is simplified, eliminating the need for machining several ring electrodes and using resistor chains to generate the potential gradient, (3) the complexity of periodic

cleaning and maintenance is reduced, and (4) the resistive glass is rugged making it amicable for field applications while maintaining mechanical integrity.

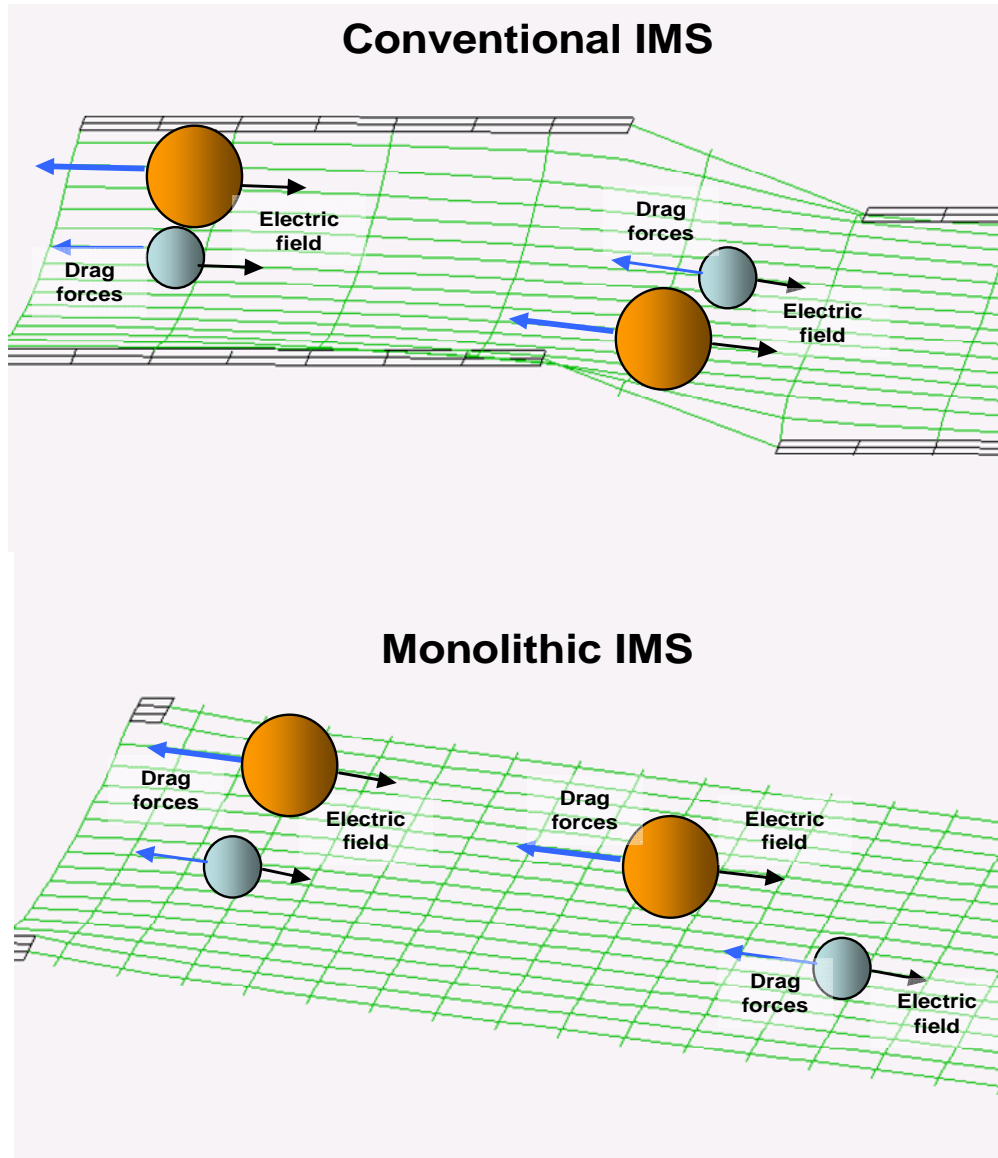


Figure 2.1 Representation of electric field potential lines generated using both a stacked ring type conventional IMS and a monolithic IMS, and their effects on drag forces exerted on individual ions within the field.

2.3. Resistive Glass Ion Mobility Spectrometer

2.3.1. Instrument Configuration

The idea and design behind the high-resolution monolithic resistive glass DTIMS was developed at Georgia Institute of Technology. The machining and assembly of the DTIMS, along with the development of the voltage divider, ion gate pulsing circuit, and detector was performed by TOFWERK AG (Thun, Switzerland). A schematic diagram of the spectrometer is shown in Figure 2.2 and a longitudinal cross section of the spectrometer is shown if Figure 2.3.

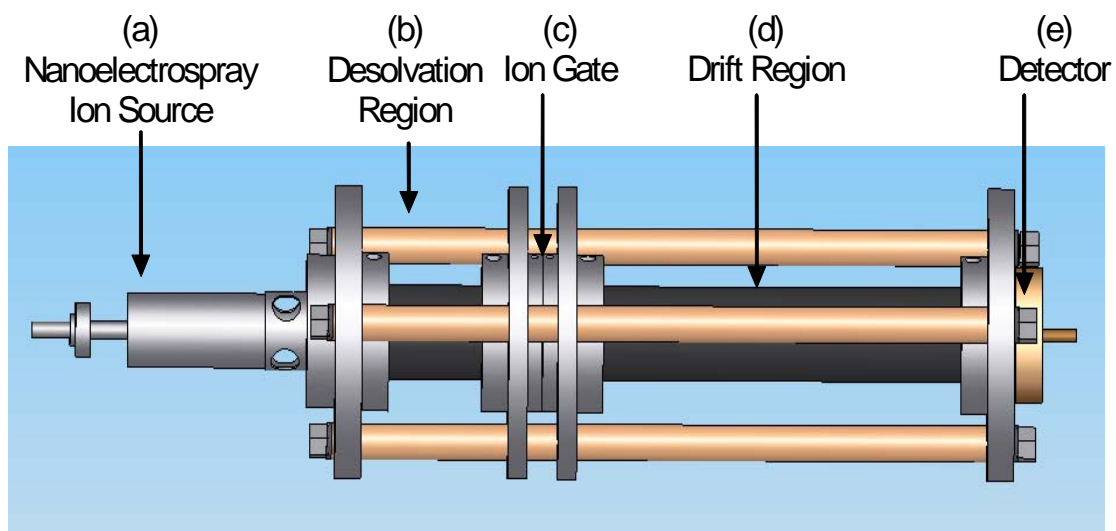


Figure 2.2 Schematic showing the resistive glass ion mobility spectrometer: (a) nanoESI ion source, (b) desolvation region, (c) ion gate, (d) drift region, and (e) Faraday plate detector.

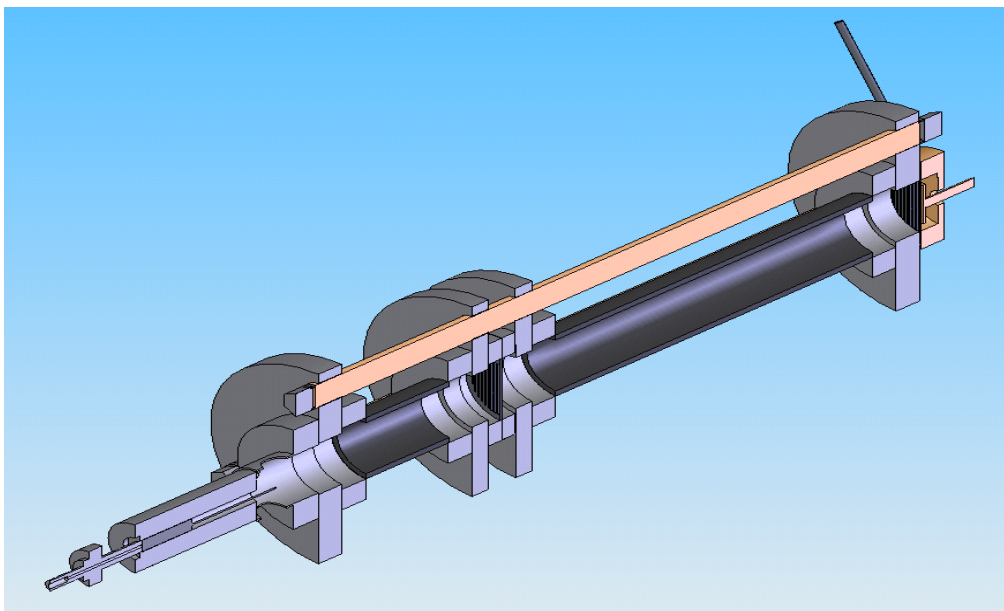


Figure 2.3 Schematic showing longitudinal cross-section of the resistive glass ion mobility spectrometer.

This instrument was furnished both with nanoESI and corona discharge ion sources. The desolvation and drift regions were constructed of monolithic sections of resistive glass tubes (Photonis, Sturbridge, MA) with a resistance of $0.45 \text{ G}\Omega\cdot\text{cm}^{-1}$. The dimensions of the tubes were 3 cm i.d. and 4 cm o.d. with lengths of 12 cm and 26 cm, respectively. The ends of these tubes were furnished with thin film metalized contact points by the manufacturer. The resistive glass tube assembly was supported by three 2.0 cm i.d. 36.5 cm long polyetheretherketones (PEEK) rods (Victrex, West Conshohocken, PA). A high-voltage power supply (FUG HCL 14-2000, Magnavolt Technologies, Plattsburgh, NY) provided, through a voltage divider (TOFWERK AG), adequate voltages for the entrance and exit of the desolvation and drift tubes and for the grid electrode placed in front of the Faraday plate detector (TOFWERK AG, Thun,

Switzerland). Table 2-1 shows typical operation voltages applied to the different regions of the instrument when utilizing nanoESI and corona discharge ion sources.

Table 2-1 Typical voltages applied to the different regions of the ion mobility spectrometer when utilizing nanoESI and corona discharge ion sources. All voltages reported in kV.

Ion Source	Needle Voltage	Desolvation Start	Desolvation End	BNG Grid 1	BNG Grid 2	Drift Start	Grid Electrode
NanoESI	15.00	12.45	10.65	10.43	10.52	10.32	0.372
Corona discharge	10.00	8.21	7.04	6.89	6.92	6.84	0.244

The default Faraday plate detector configuration consists of a 26 mm diameter iridized aluminum flat plate positioned 5.0 mm behind the grid electrode. As seen in Figure 2.4, a photograph of the resistive glass DTIMS with the Faraday cage removed, the desolvation and drift tubes were wrapped with red silicone heating tape (Minco, Minneapolis, MN) in order to enhance desolvation of electrospray droplets at higher sample flow rates. This heating tape was powered by a 60 V- 2 A DC power supply (BK Precision Co. 1715A, Yorba Linda, CA) and regulated by a temperature controller (Minco CT15, Minneapolis, MN) equipped with a PT100 sensor (S17624PDZT40A, Minco). In order to insulate the instrument from electromagnetic interferences and protect the operator from accidental exposure to high voltage, the instrument was encased in a protective cage constructed of 2 mm thick aluminum mesh. This mesh extended 5.0 cm beyond the detector plate in order to shield the anode and current amplifier.

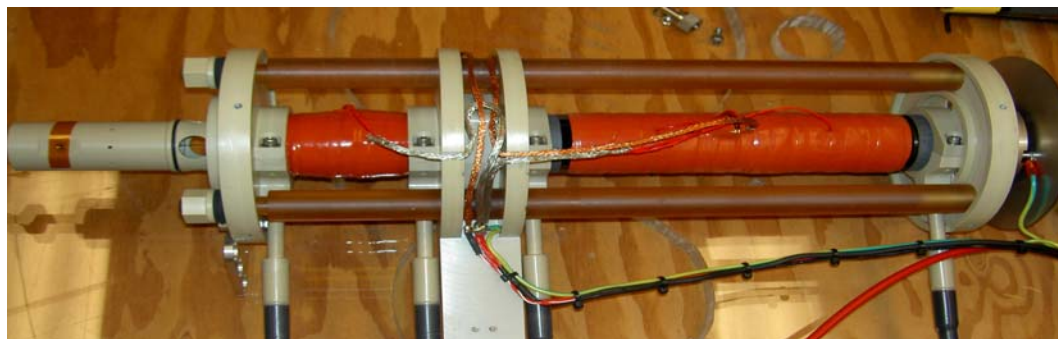


Figure 2.4 Photograph of the resistive glass monolithic ion mobility spectrometer with the protective Faraday cage removed.

Drift gas was supplied to the IMS through a gas inlet positioned behind the anode. The gas inlet was connected into a custom-built air diffuser to provide a more homogeneous drift gas flow rate through the mobility cell. The flow rate was controlled via a precision flow meter (PMR1, BEL-ART/Scienceware, Pequannock, NJ). Prior to entering the drift chamber, the drift gas was dried by a moisture trap (Restek 22015, Bellefonte, PA).

Ion gating was achieved with a Bradbury-Nielsen-type ion gate⁶⁶ located between the end of the desolvation tube and the entrance of the drift tube. An aperture mask (11 mm i.d.) was placed in front of the ion gate to a) decrease the amount of solvent from the electrospray plume entering the drift tube, b) increase the velocity of the drift gas exiting the drift chamber, thus enhancing charged droplet desolvation, and c) reduce the diffusion of laboratory air into the drift tube when the instrument is not being operated.¹²⁷ Gate pulse widths between 50 and 800 μs are commonly used. Custom-built pulsing electronics (TOFWERK AG) powered the Bradbury-Nielsen ion gate (BNG). The logic signals required by the pulsing electronics were generated through a PC (AMD Athlon

XP 2600+ 1.91 GHz, 1.0 GB RAM) equipped with an arbitrary waveform generator board (National Instruments 5411, Austin, TX). The ion gate was closed by applying ± 35 V to adjacent wire sets causing positive ions to be collected on the negative wire set and negative ions to be collected on the positive wire set. Ions were gated into the drift chamber at a frequency of 9.76 Hz. The ion gate can be theoretically operated at frequencies up to 120 kHz with ion gate pulse widths as small as 1 μ s, however these maximum operating conditions are not utilized due to deterioration in gate performance at these extreme limits. The ion gate timing was set by the user via software coded in LabVIEW 7.0 (National Instruments, Austin, TX).

The Faraday plate detector was connected to a custom-built amplifier constructed at TOFWERK AG with an input resistance of 1 k Ω , an amplifier rise time of 250 μ s (10 % to 90 %), a gain setting of 0.1 pA mV⁻¹, and a noise level of 2 pA peak to peak rms with 500 sweeps averaged. This amplifier was connected to a 200 MHz oscilloscope (Tektronix TDS 2024, Richardson, TX) in series with a fast 12-bit 5 Msamples s⁻¹ A/D data acquisition board (National Instruments 6111).

Faraday plate detection can be replaced with MS detection by coupling the DTIMS to our JEOL AccuTOF mass spectrometer (Tokyo, Japan, Figure 2.5) to achieve a detection range of up to 6,000 m/z with a resolving power of $> 6,000$ FWHM and mass measurement accuracies < 5 parts-per-million (ppm).

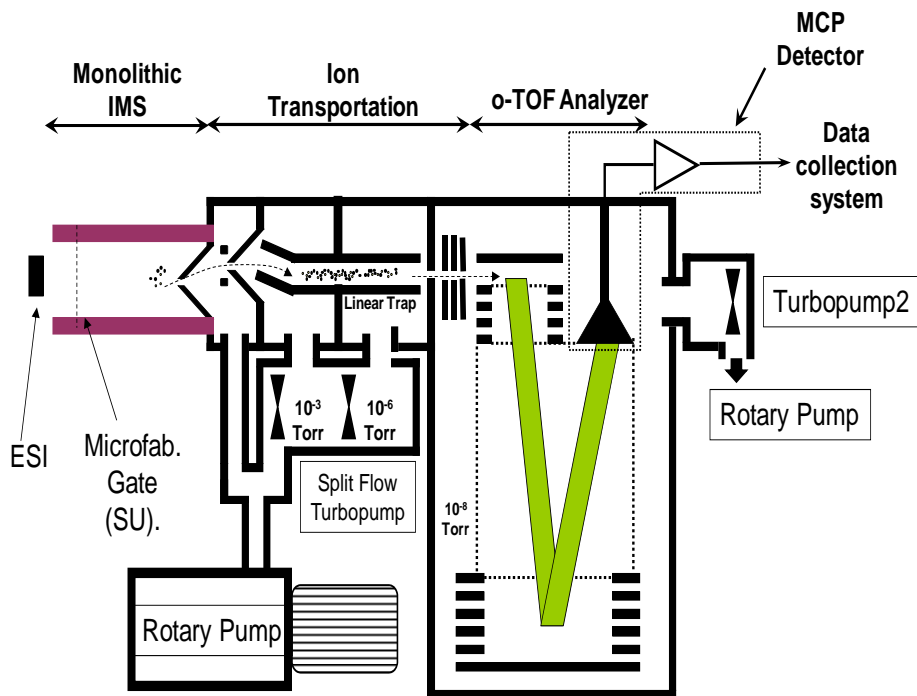


Figure 2.5 Schematic showing the coupling of the DTIMS to a JEOL AccuTOF-MS.

2.3.2. Ion Source Configurations

The electrospray ion source was designed to function in both micro and nanoESI modes depending on the choice of emitter (New Objective Inc. PicoTip, Woburn, MA) and liquid sample flow rates. A 15 μm i.d. emitter is used with flow rates ranging from 100 to 500 $\text{nL}\cdot\text{min}^{-1}$, a 30 μm i.d. emitter is used with flow rates ranging from 300 to 1,000 $\text{nL}\cdot\text{min}^{-1}$, and a 100 μm i.d. emitter is used with flow rates ranging from 400 to 3,000 $\text{nL}\cdot\text{min}^{-1}$ without the assistance of a sheath gas. A sheath gas was not utilized because preliminary experiments showed that it had the undesired effect of destabilizing the electrospray plume. The emitter was held by a cylindrical PEEK holder, which directed the charged spray into the desolvation chamber. The nanoESI needle mount has four 1.5 cm diameter drilled holes that allowed observation of the emitter tip and the

spray. These viewing holes were covered with a removable quartz ring to prevent any ambient air currents from destabilizing the spray. The position of the nanoESI emitter was adjusted so it penetrated 1.5 cm into the desolvation region. High-voltage was applied to the sprayed solution via an electrochemical junction placed 30 cm upstream from the emitter tip. Sample solution was delivered to the electrospray ion source by a liquid handling pump (Valco Instruments Co. VICI M6, Houston, TX) connected to the tip using either fused silica capillary tubing (150 μm i.d. 350 μm o.d., Polymicro Tech. Phoenix, AZ) or PEEK capillary tubing (100 μm i.d. 360 μm o.d., 1571 Upchurch Oak Harbor, WA). A second high-voltage power supply (FUG HCP 14-2000, Magnavolt Technologies, Plattsburgh, NY) provided independent voltage control for the nanoESI and corona discharge ion sources up to $\pm 20,000$ V. An electrospray voltage of 2,000 - 3,000 V versus the desolvation chamber entrance provided the most stable spray conditions.

Corona discharge experiments were performed by replacing the electrospray emitter with a sharpened 1 mm o.d. tungsten welding tip (McMaster-Carr, Atlanta, GA). A fine wire grid was mounted between the tungsten tip and the entrance of the desolvation region and was used as the discharge counter electrode. The distance between the corona discharge tungsten tip and this grid was approximately 0.5 mm. A discharge voltage of 800 - 1,200 V and 1,600 - 2,000 V versus the desolvation chamber entrance, when using helium and nitrogen drift gas respectively, provided a stable discharge.

2.3.3. Timing Scheme DTIMS Mode

The timing scheme used in DTIMS and multiplexed DTIMS mode for synchronizing ion gating and data acquisition is shown in Figure 2.6. The arbitrary waveform generator (NI-5411) is first software-triggered by the operator (software trigger 1), causing a transistor-transistor logic (TTL) 5 V pulse to be sent to the IMS ion gate voltage divider and pulsing electronics, and a second TTL pulse, generated via the NI-5411 “marker” output, to be sent to the data acquisition board (NI-6111) via the real-time system integration (RTSI) 6 line. The 6111 data acquisition board is synchronized with the 5411 arbitrary waveform generator board via its 20 MHz on-board clock, which is fed to the phase-locked loop (PLL) input of the 5411 arbitrary waveform generator. Data acquisition is enabled by the operator via a second software trigger, which enables the NI-6111 board. After the board is enabled, data acquisition is initiated synchronously with the next marker pulse sent to the ADC start input.

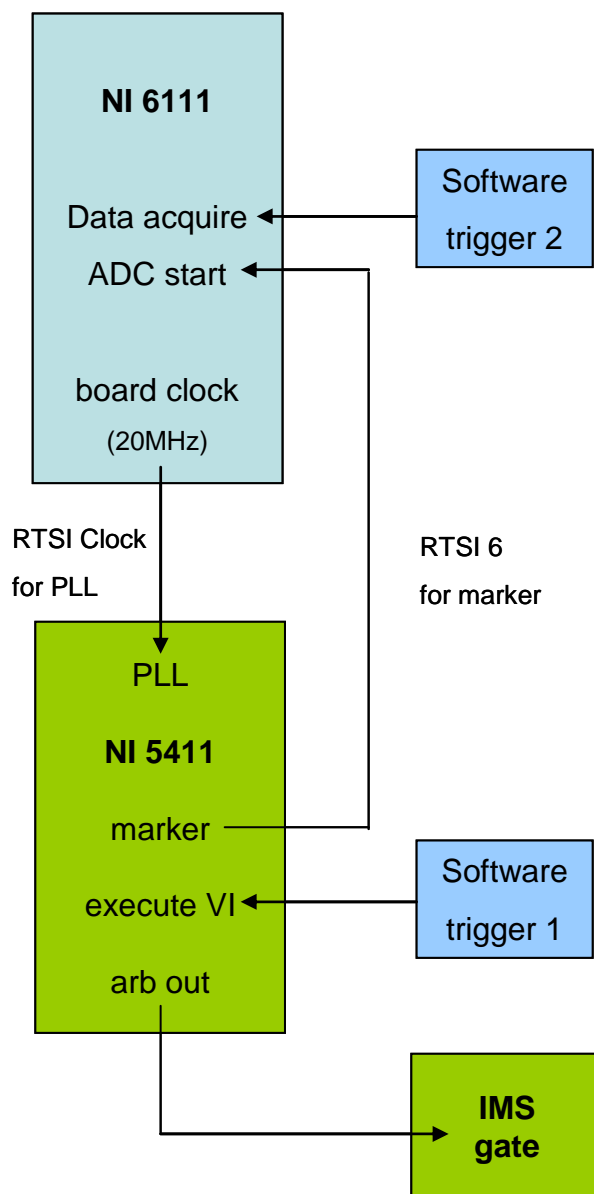


Figure 2.6 Timing scheme used in DTIMS and multiplexed DTIMS modes for synchronizing ion gating and data acquisition using a National Instruments NI-5411 arbitrary waveform generator and a NI-6111 analog-to-digital data acquisition board.

2.3.4. Timing Scheme DTIMS-MS Mode

The timing scheme used when coupling the DTIMS to our JEOL TOF-MS for synchronizing ion gating with the JEOL TOF pulser and modified data acquisition system uses a National Instruments NI-5411 arbitrary waveform generator, a NI-6602 counting

board, and a FAST ComTec GmbH P7887 (Oberhaching, Germany) 250 ps time bin, 4GHz multiple-event time digitizer is shown in Figure 2.7. The arbitrary waveform generator (NI-5411) is first software-triggered by the operator, causing a TTL 5 V pulse to be sent to the IMS ion gate voltage divider and pulsing electronics, and a second TTL pulse, generated via the NI-5411 “marker” output, to be sent to the counting board (NI-6602) via the Programmable Function Interface (PFI) 9 line with a Bayonet Neill-Concelman (BNC) cable. The NI-6602 counting board is synchronized with the NI-5411 arbitrary waveform generator board via its 20 MHz on-board clock, which is fed to the phase-locked loop (PLL) input of the NI-5411 arbitrary waveform generator via PFI 8 line with a BNC cable. The JEOL TOF pulser is triggered via counter output 1 (ctr 1) with a 64 ns wide TTL level pulse via PFI 32 with a BNC cable. Peak-to-peak widths of the TOF pulser trigger pulse were 59.2, 82.0, 115.2, and 322.0 μs to operate the mass analyzed with an m/z range of 0-1000, 0-2000, 0-4000, and 0-6000, respectively. Data acquisition is synchronized with the NI-6602 counting board with a 1 V pulse via counter output 2 (ctr 2) with a BNC cable, which enables the FAST ComTech P7887 board. After the board is enabled and synchronized, data acquisition is initiated by the user via MCDWIN v2.8 software provided by FAST ComTech.

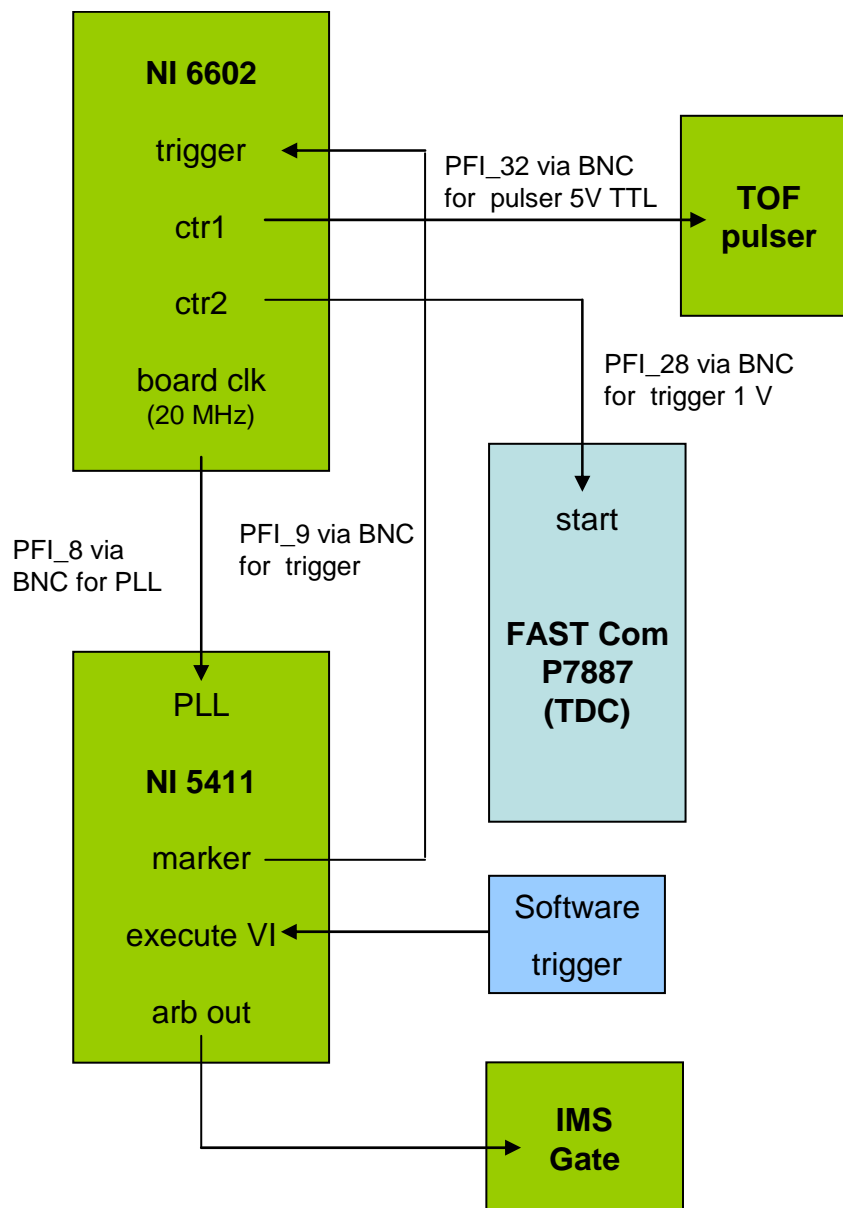


Figure 2.7 Timing scheme used in DTIMS-MS mode for synchronizing ion gating with the JEOL TOF pulser and data acquisition system using a NI-5411 arbitrary waveform generator, a NI-6602 counting board, and a FAST ComTec GmbH p7887 multiple-event time digitizer.

2.4. LabVIEW Software for DTIMS, Multiplexed DTIMS, and DTIMS-MS Operation

LabVIEW, which stands for Laboratory Virtual Instrumentation Engineering Workbench, is a software platform and development environment developed by National Instruments in 1986 for the Apple Macintosh. LabVIEW uses a visual programming dataflow language known as G. Since its inception, LabVIEW has grown to a multi-platform system that is compatible with Microsoft Windows, UNIX, Linux, and Mac OS X. The software is typically used for data acquisition, data processing, instrument control, process automation and graphing.

LabVIEW allows non-programmers to code software programs simply by dragging and dropping virtual instruments (VIs) of familiar lab equipment into the programming environment. These VIs consist of a block wire diagram, a front panel that is designed to look like an instrument interface, and a connection panel. Once the desired VIs are placed into a master block wire diagram, their order of execution is determined by their placement and order of connection. Multiple VIs are connected together by drawing wires between the inputs (controls) and outputs (indicators) of the connection panel, which allow the user to input data into, or extract data from a running virtual instrument. A virtual instrument either can be run as a standalone program, with the front panel serving as a user interface, or can be embedded into the block wire diagram of a more complex virtual instrument. Many libraries with a large number of pre-designed VIs are provided with LabVIEW for ease of use, in addition to specific function libraries included with the purchase of hardware such as data acquisition boards and signal generators.

Figure 2.8 shows the front control panel and Figure 2.9 shows the wire diagram of the virtual instrument (VI) designed in LabVIEW 7.0 to control the NI-5411 arbitrary waveform generator. This VI allows for a user selected conventional or multiplexed sequence to be outputted to the DTIMS ion gate pulsing electronics. Once the user selects an appropriate length sequence, each element in the sequence must be assigned an appropriate modulation bin width, also referred to as the ion gate width. The user then initiates the VI with a software trigger and the arbitrary waveform generator continues to generate the selected sequence until the VI is terminated via the software stop.

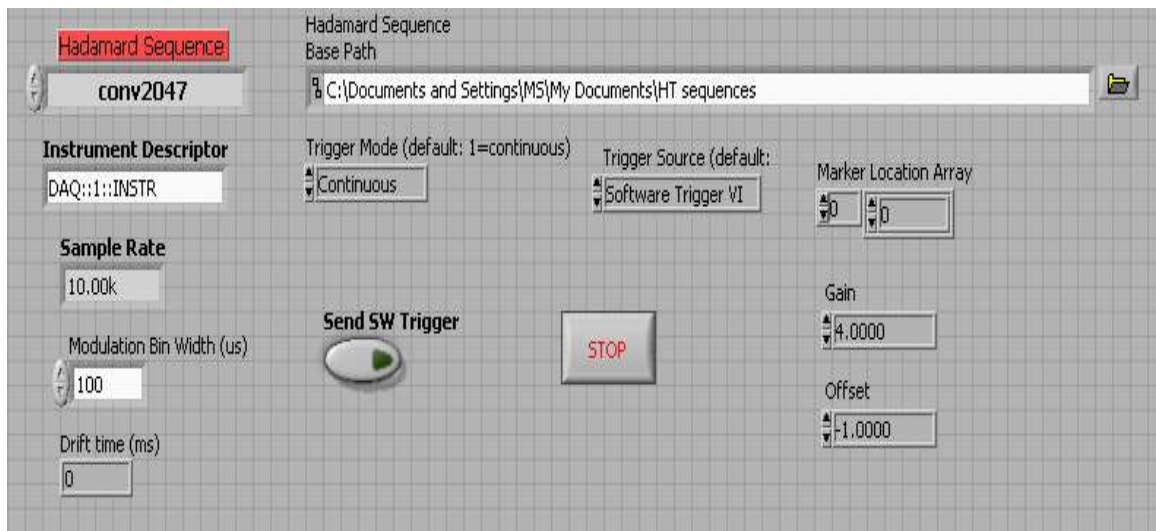


Figure 2.8 Front panel of the VI used to control the arbitrary waveform generator.

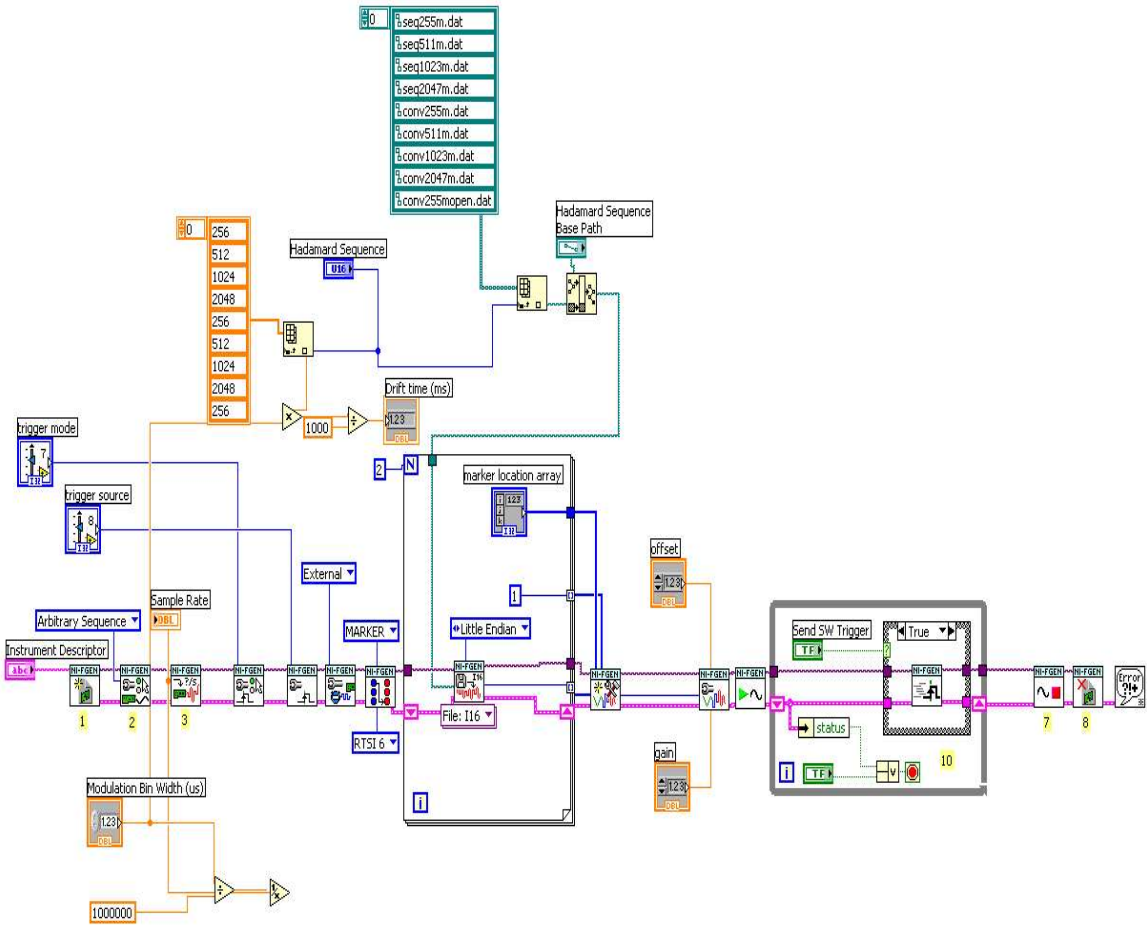


Figure 2.9 Wire diagram of the VI used to control the arbitrary waveform generator.

Figure 2.10 shows the front control panel and Figure 2.11 shows the wire diagram of the virtual instrument (VI) designed in LabVIEW 7.0 to control the NI-6111 analog-to-digital data acquisition board. This VI allows for a user selected acquisition bin width for oversampling the data. The modulation bin width and sequence length must match the values input into the arbitrary waveform generator VI. This VI will then collect a predefined number of sweeps and average them before displaying the final mobility spectrum. The spectrum can then be saved in tab delimited text format and exported to a graphing program.

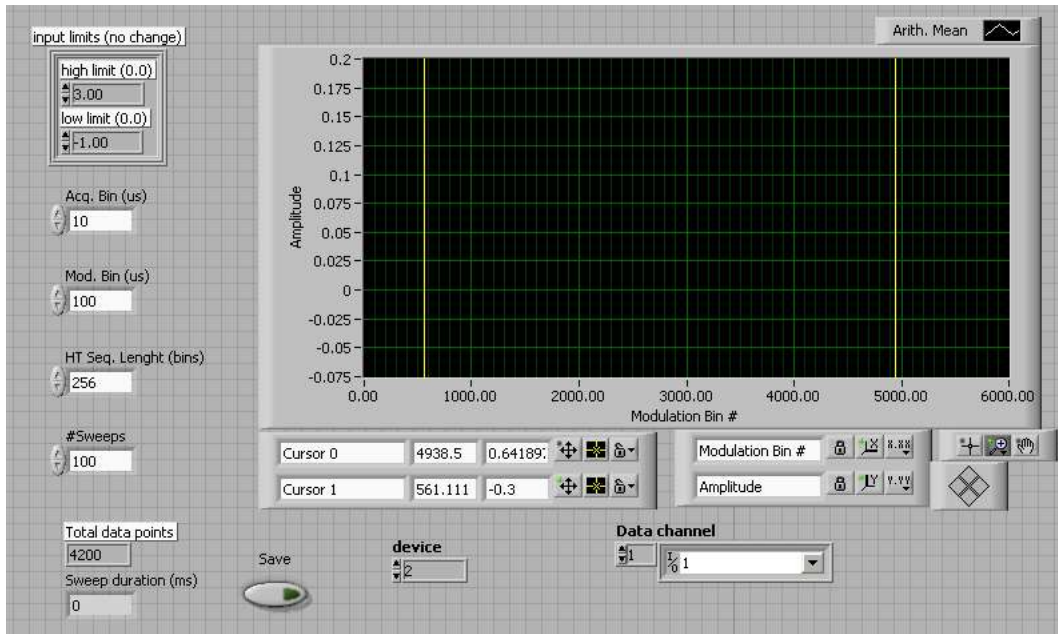


Figure 2.10 Front panel of the VI used to control the data acquisition system.

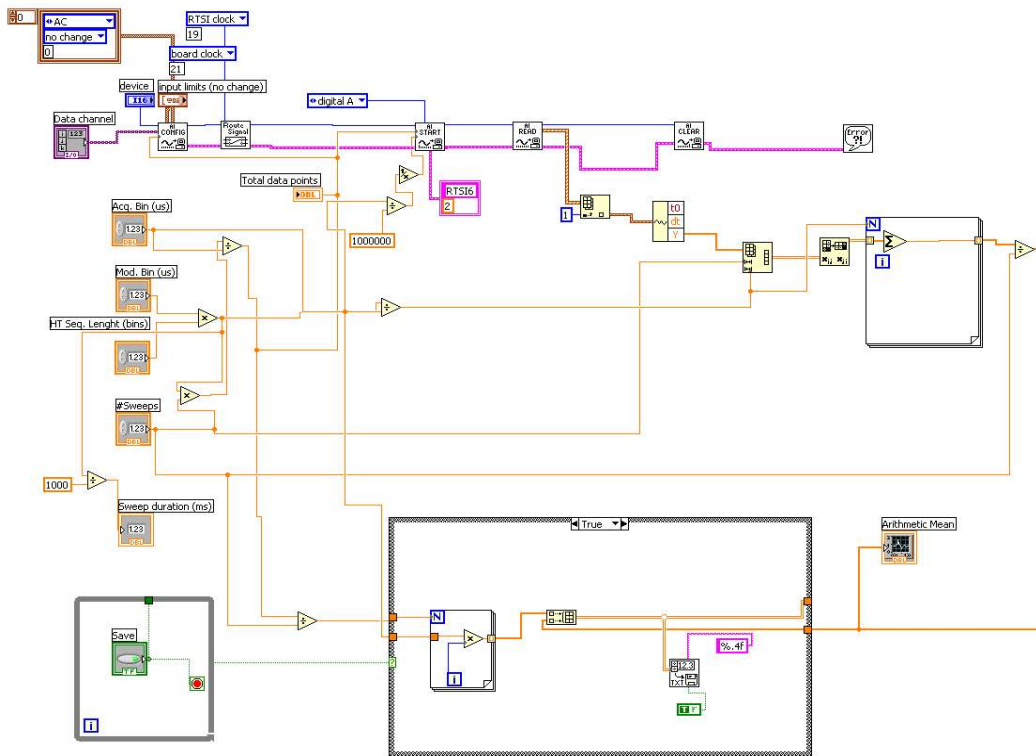


Figure 2.11 Wire diagram of the VI used to control the data acquisition system.

Figure 2.12 shows the front control panel and Figure 2.13 shows the wire diagram of the virtual instrument (VI) designed in LabVIEW 7.0 to control the NI-6602 counting board. This VI generates the nested triggering schemes required to operate the DTIMS, the TOF pulser and the modified FAST ComTec P7887 multiple-event time digitizer data acquisition system. The VI allows not only for a user selected TOF pulser width, referred to as the TOF gate duration, but also controls the frequency of the TOF pulser, referred to simply as 1/TOF. This frequency controls the m/z range and sensitivity of the instrument. A shorter, or smaller, “1/TOF” allows for more frequent injection of ions into the mass analyzer by the TOF pulser, increasing the duty cycle and sensitivity of the instrument. However, decreasing the time between TOF injection pulses limits the m/z range of the mass analyzer by excluding ions with a longer flight time from being measured by the microchannel plate (MCP) detector.

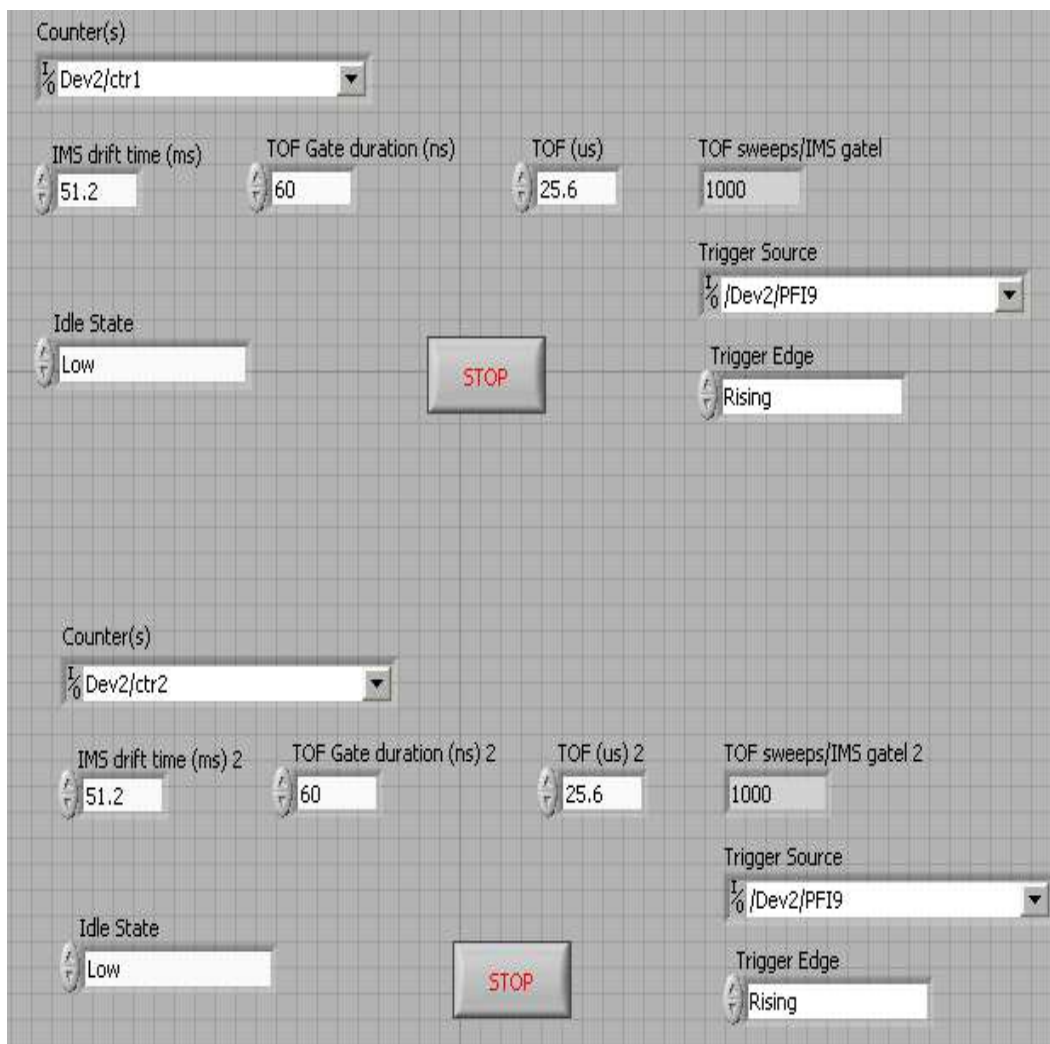


Figure 2.12 Front panel of the VI used to control the counting board for generation of the nested triggering schemes required to synchronize the DTIMS ion gate, TOF pulser, and FAST ComTec P7887 TDC for DTIMS-MS.

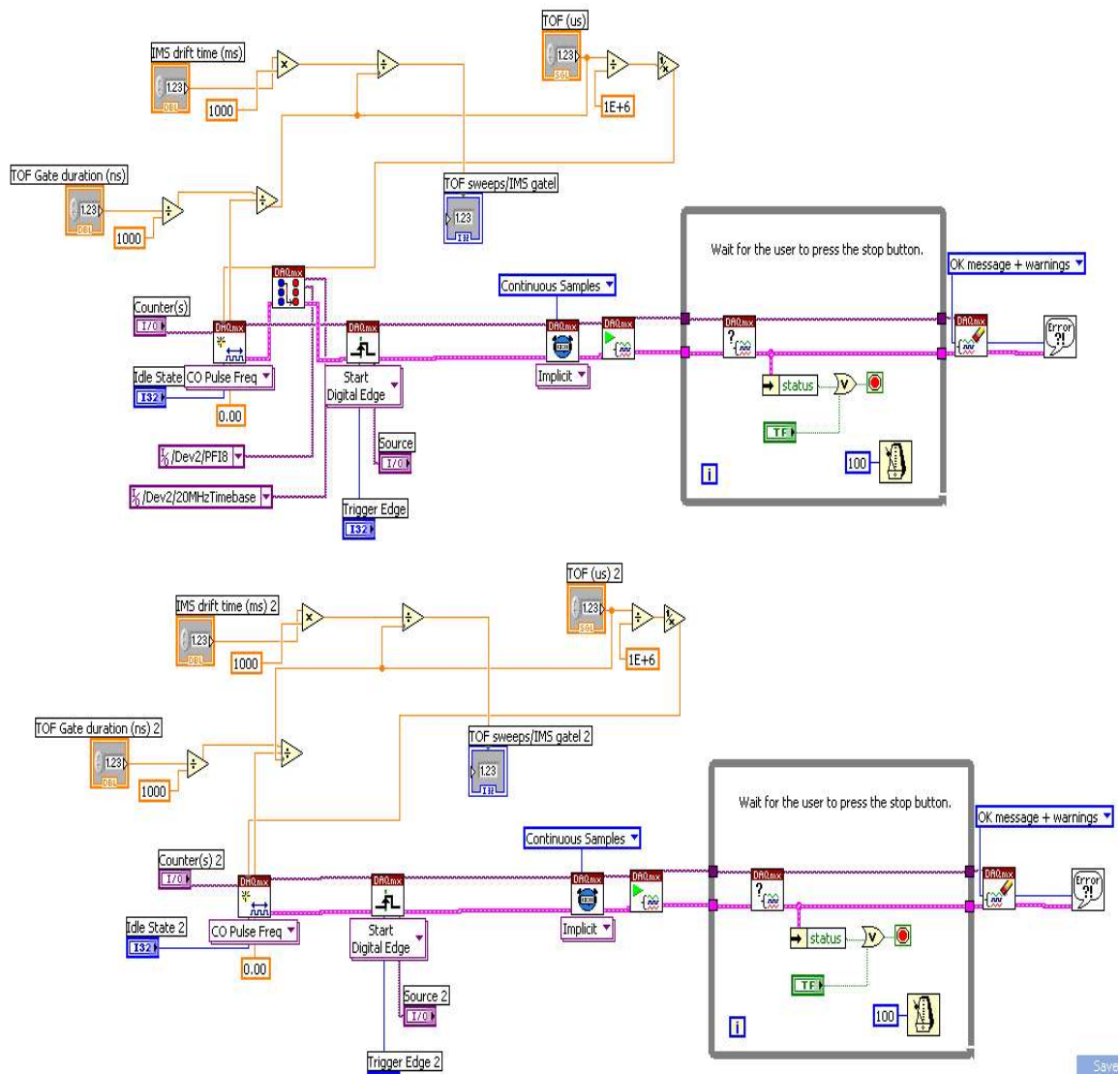


Figure 2.13 Wire diagram of the VI used to control the counting board for generation of the nested triggering schemes required to synchronize the DTIMS ion gate, TOF pulser, and FAST ComTec P7887 TDC for DTIMS-MS.

2.4.5. Preliminary DTIMS-MS Data

Figure 2.14 shows the 1-D time-of-flight spectrum of a 1 μM reserpine solution collected with the DTIMS-MS and the FAST ComTec P7887 TDC showing detailed isotopic structure. Flight time in ns is displayed on the x-axis and total ion counts are displayed on the y-axis. The m/z of the individual ions is obtained by first running a

calibration mixture of an analyte with known masses at periodic location, such as CsI, which forms $[\text{Cs}(\text{CsI})_n]^+$ clusters, or polyethylene glycol (PEG). This data is then used to create a time-of-flight to m/z correlation function that is then applied to all subsequent data to produce an accurate m/z value for all detected ions.

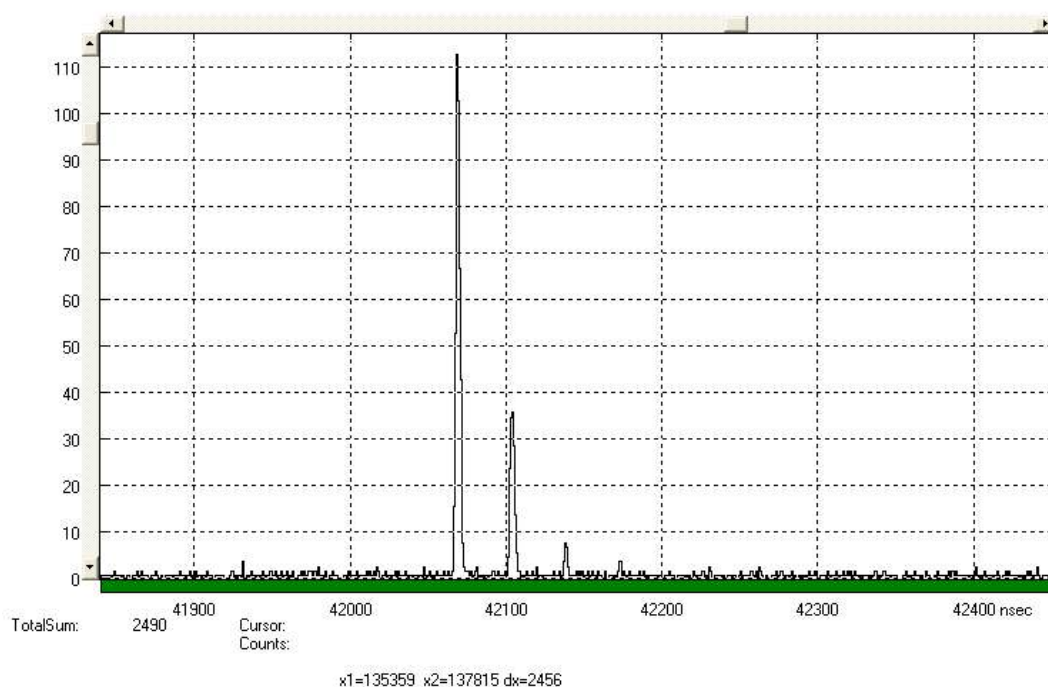


Figure 2.14 1-D TOF spectrum collected with the FAST ComTec P7887 of a 1 μM reserpine solution showing detailed isotopic structure with flight time in ns displayed on the x-axis and total ion counts displayed on the y-axis.

Figure 2.15 shows the 2-D time-of-flight as a function of the drift time mobility spectrum of a 1 μM reserpine solution collected with the DTIMS-MS and the FAST ComTec P7887 TDC. Flight time in ns is displayed on the x-axis, total ion counts are displayed on the y-axis, and drift time in ms is displayed on the z-axis. Although reserpine is clearly visible at a flight time of 42,065 ns, which corresponds to an $[\text{M}+\text{H}]^+$ peak with a 609.281 m/z , the separation in the ion mobility direction (z-axis) is lost and

reserpine can be seen with a relatively constant intensity over the 0-40 ms drift time range. After careful analysis of the data, we hypothesized that excessive collisional cooling in the 36 cm long, multi-pressure regime (10^{-2} , 10^{-3} , and 10^{-6} Torr) ion guide of the JEOL AccuTOF-MS, was causing packet spreading and a loss of all information obtained within the DTIMS. In order to reduce the amount of collisional cooling within the ion guide of the AccuTOF, the residence time of the ion packets within the ion guide needed to be decreased. This was achieved by a combination of 2 methods: (1) a series of orifices with smaller apertures was machined and tested to determine an appropriate balance between sensitivity and pressure, and (2) a dual stage direct drive rotary vane vacuum pump (E2M80, Edwards, Tewksbury, MA) with a pumping speed of 53 cubic feet per minute, and a maximum pressure of 7.7×10^{-4} Torr, was connected to the 1st vacuum region of the AccuTOF ion guide.

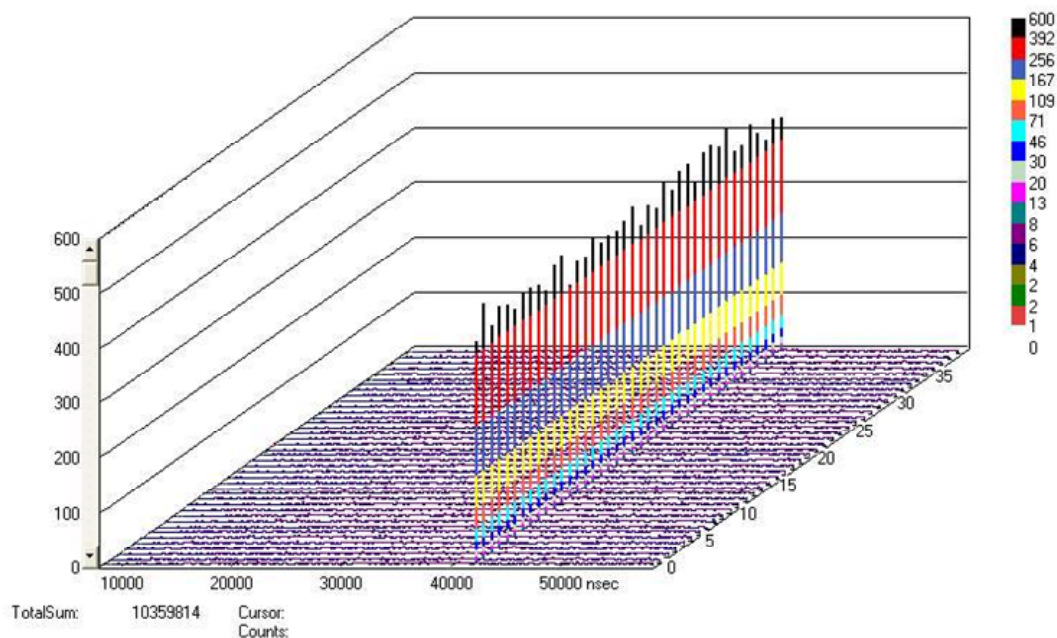


Figure 2.15 2-D TOF as a function of the drift time spectrum of a 1 μ M reserpine solution collected with the DTIMS-MS. Flight time in ns is displayed on the x-axis, ion counts are displayed on the y-axis, and drift time in ms is displayed on the z-axis.

Figure 2.16 shows the 2-D time-of-flight as a function of the drift time mobility spectrum of the same 1 μM reserpine solution, analyzed with the smaller orifices and the additional pumping capacity. The solvent clusters can now be seen between 10,000 and 20,000 ns and reserpine is observed at a flight time of 42,065 ns. Although the orifice and vacuum modifications did not completely eliminate the packet spreading within the ion guide, some defined structure is now clearly visible in the mobility dimension (z-axis).

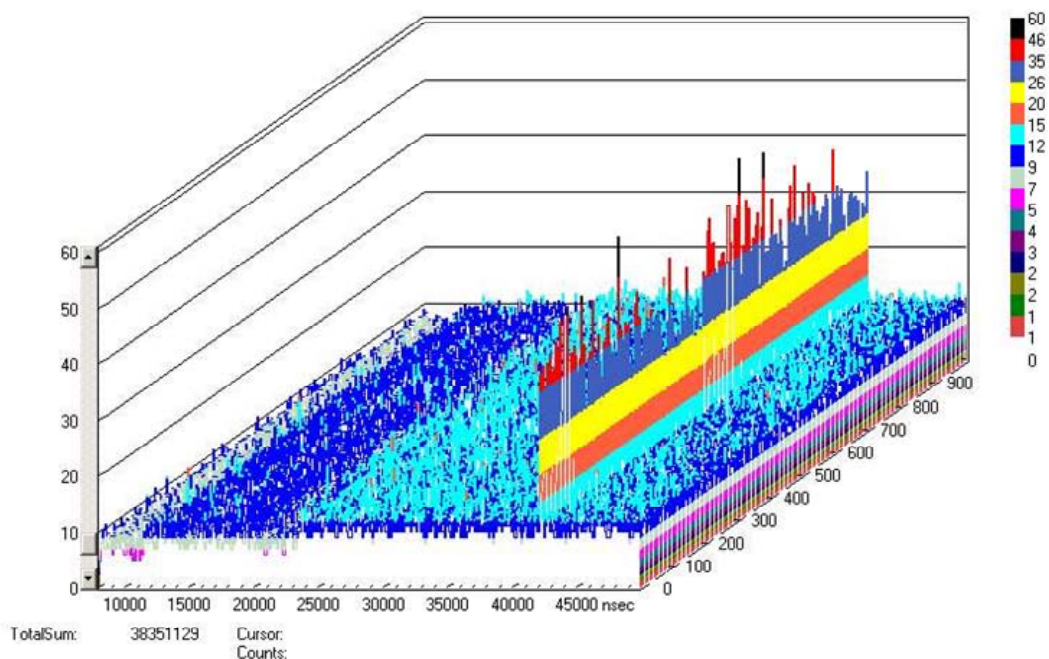


Figure 2.16 2-D TOF as a function of the drift time spectrum of a 1 μM reserpine solution collected with the DTIMS-MS after vacuum modifications. Flight time in ns is displayed on the x-axis, ion counts are displayed on the y-axis, and drift time in ms ($\times 10^1$) is displayed on the z-axis.

2.4.6. Minimizing DTIMS-MS Packet Spreading

Many approaches have been employed to balance the amount of collisional cooling ions required to have a narrow kinetic energy distribution prior to entering the TOF analyzer and maximize axial acceleration to minimize packet spreading during their transit from atmospheric pressure to the high-vacuum region of the mass analyzer. The simplest approach involves the use of a shorter ion guide to reduce the amount of time an ion packet spends in the ion guide, and therefore reduce the degree of collisional cooling. However, shorter ion guides typically do not provide sufficient time to focus ions to the center of the guide for efficient transfer to subsequent ion optics.¹²⁸ Russell and co-workers installed a 5 cm vacuum interface with a high field region (up to 1,000 V/cm) directly behind the drift cell to not only reduce collisional cooling of their ions but also to serve as an ion activation device for collision induced dissociation for mobility selected ions.¹²⁹ Smith and co-workers installed a short (10 cm) ion funnel at the exit of their drift cell that not only accumulated ions and reduced packet spreading, but could also be operated as an extension of their mobility cell resulting in improved resolving power.¹³⁰ An alternative approach to reducing collisional cooling and packet spreading involves the use of higher order multipoles to function as ion guides, such as hexapoles and octopoles. Compared to quadrupoles, these multipoles generate stronger containment fields for the same voltage and frequency applied to the rods and are advantageous for better confining ions in the radial direction.¹³⁰ A similar method involves using a linear quadrupole with an added superimposed multipole field. These additional superimposed fields are generated with mismatched electrode pair geometries.¹³⁰ Siu and co-workers applied a different approach involving a 20-segment quadrupole to generate not only conventional

rf fields for radial collisional focusing, but also axial acceleration fields. Their quadrupole could be used for reducing the residence time of ions within the ion guide, or function as a reduced pressure mobility cell.¹³¹

Future modification of the AccuTOF will involve installing a segmented ion guide to allow for application of stronger axial electric fields via variable-voltage potentials on the different segments of the ion guide to reduce the residence time of the ions further and “shotgun” them through the ion guide. These modifications will be undertaken by a postdoctoral researcher continuing this project.

CHAPTER 3. PERFORMANCE, RESOLVING POWER AND RADIAL ION DISTRIBUTIONS OF A PROTOTYPE NANOELECTROSPRAY IONIZATION MONOLITHIC RESISTIVE GLASS ATMOSPHERIC PRESSURE DRIFT TIME ION MOBILITY SPECTROMETER

3.1. Abstract

This chapter describes the initial characterization of the performance of a prototype resistive glass DTIMS. A detailed examination of the effects of drift gas flow rate, temperature and anode grid to anode distance on the observed resolving power and sensitivity of the instrument are presented. Once optimum experimental parameters are identified, different ion gate pulse widths and their effect on the temporal spread of the ion packet are investigated. A characterization of the radial ion distribution of the ions in the drift region of the spectrometer is performed to determine the ion density distribution within the prototype DTIMS. Preliminary DTIMS data demonstrating the applicability of this instrument to the study of small molecules of environmental relevance by analyzing a commercially-available siderophore, deferoxamine mesylate, in both the free ligand and iron-bound form is also presented.

3.2. Introduction

Although drift time ion mobility spectrometry (DTIMS) was first introduced as an analytical technique in the 1970s,³ a fundamental understanding of processes within the

ionization and drift regions were slow to develop because of limited instrument availability. Initial work revealed that ions are prone to form clusters where the charged molecule is associated with a neutral.^{10, 132, 133} The type of clusters formed depends on the identity of this neutral. Therefore, not only is the selection of the drift gas (X) important, but there is also a heavy dependence on any ambient vapors and contaminants present in the ionization and desolvation regions of the spectrometer. An example of typical clusters formed in atmospheric pressure DTIMS would be $MH^+ \cdot X_m \cdot (H_2O)_n$, where m and n typically fall between 1 to 4.¹³³⁻¹³⁵ The size of these clusters is dependent on moisture content and temperature in both the desolvation and drift regions of the spectrometer.^{134, 136} Further investigation into the fundamental processes within the mobility cell was pursued in 1985 by Kim and Spangler.¹³⁷ Their work revealed the presence of clusters other than water-ion, and identified dimer ion formation and dimer-water clusters that were later also found to be dependent on temperature and drift gas composition.¹³⁸ The role of temperature and water content in DTIMS were addressed systematically for a wide range of product ions in the early 1990s. It was shown that removing the moisture from the drift gas using gas purification traps produced stable, reproducible spectra with sharp peak shapes. Alternatively, operating the DTIMS at elevated temperatures, even without the use of gas purification, yielded sharp peaks by limiting cluster formation.¹³⁹ However, although increasing the temperature limited cluster formation, it also increased the Brownian motion of the ions and drift gas within the mobility cell, thereby increasing the diffusion of individual ion packets, resulting in wider peaks in the final mobility spectrum.

The drift gas density has also been shown to play a major effect on the types of ions generated within the desolvation and drift regions of the DTIMS because of its effect on cluster formation, and the mobility of those ions. The behavior of ions within the electric field of the mobility cell is regarded as a “spasmodic motion,” where the ion is rapidly accelerated by the electric field until it collides with a drift gas molecule and loses part, or all of its acquired momentum. The ion is then re-accelerated rapidly until it collides with the next drift gas molecule. This process is repeated multiple times until the ion exits the mobility cell and is detected.⁴ Increasing the drift gas flow rate will increase desolvation and limit cluster and dimer formation, however it will also increase the number of ion-gas molecule collisions, resulting in wider peaks in the final mobility spectrum.

In this chapter, an extensive instrumental characterization study is performed to investigate the effects of temperature and drift gas flow rate not only on cluster and ion formation, but also on their effects on desolvation of our ESI generated ions, to determine optimal operational parameters. The effects of instrumental parameters such as anode grid to anode distance and different ion gate pulse widths on the resolving power and sensitivity of our prototype resistive glass DTIMS is explored. A characterization of the radial ion distribution of the spectrometer will be performed to determine the ion density distribution of the ions in the drift region within our prototype DTIMS. This study will help identify if any design changes need to be implemented to minimize loss of ions due to collisions with the walls of the drift tube and to identify the area of highest ion density for maximizing transfer of ions when coupling our prototype DTIMS to a mass spectrometer.

Following these instrumental characterization studies, we demonstrate the use of this resistive glass ion mobility spectrometer to study an environmentally-relevant marine siderophore with a size similar to common tuning compounds. Siderophores are known to undergo significant conformational changes upon binding to metal centers, and thus, the ionic mobilities for the uncomplexed and complexed forms should be very different, making them amenable to IMS separation.

3.3. Experimental Details

3.3.1. Samples and Reagents

The solvent used for ESI experiments was a mixture of acetonitrile (High Performance Liquid Chromatography (HPLC) grade, Fisher, Suwanee, GA), water (Barnstead Nanopure Diamond, Van Nuys, CA), and acetic acid (99.99+ %, Sigma, St. Louis, MO) in an 80/19.9/0.1 volume ratio. Reserpine (Sigma, St. Louis, MO), Iron (III) chloride hexahydrate (99 %, Acros, Geel, Belgium) and deferoxamine mesylate (Calbiochem, San Diego, CA) were used without further purification. Nitrogen (99.9997 %, Airgas, Atlanta, GA) and helium (UHP-300, 99.999 %, Airgas) were used as drift gases for nanoESI and corona discharge experiments, respectively.

3.3.2. High Performance Liquid Chromatography

Experiments were performed on a Waters (Milford, MA) HPLC system equipped with 1525 Binary HPLC Pump and 2487 Dual λ Absorbance Detector. A Waters Symmetry C-18 column (15 cm x 4.6 mm i.d.) was used for analysis. The flow rate for the mobile phase was 1.0 mL \cdot min⁻¹. The mobile phase consisted of distilled water and

acetonitrile. The gradient program was 100 % water held for 2 min, the gradient was then increased to 100 % acetonitrile from 2 to 14 min and held at 100 % acetonitrile for 2 min.

3.4. Results and Discussion

Sufficient statistical confidence in the identification of unknowns purely from ion mobility spectra is based on the accuracy of drift time measurements and sufficient resolving power to distinguish between ionic species injected into the drift tube. DTIMS resolving power (R) is defined as the ratio between the drift time (t_d) and the full peak width at half maximum (w) as shown by Equation 1.2. Theoretical treatments of peak broadening, and thus resolving power, have focused on studying processes occurring along the drift tube longitudinal axis. Ideally, broadening in this dimension depends only on the ionic species' diffusion coefficient, temperature, width of the ion gate pulse, and absolute drift time. However, Hill et al. have observed that radial electric field inhomogeneities and ion/ion repulsions are also an important source of deviations from the theoretically-achievable resolving power.² In addition, capacitive effects in the nearby regions of the Faraday plate detector, determined by its distance to the aperture grid, have also been shown to play a significant role in the observed peak width.¹⁴⁰

According to theoretical treatment, ion mobility is related to various experimental parameters and analyte characteristics by the Equation 1.1.¹³ As a first step in characterizing our prototype IMS, the effect of various experimental parameters on the observed resolving power, ion mobility, and sensitivity were investigated.

3.4.3. Temperature Effects in our Prototype DTIMS

The effect of drift tube and drift gas temperature was the first parameter to be studied. Heating the drift tube and drift gas provides the means to desolvate analyte ions however, temperature and resolving power have an inverse relationship. Therefore, it is important to investigate if with the reduced solvent load introduced by the nanospray ion source, operation at temperatures higher than ambient grants an improvement in desolvation efficiency which offsets the unavoidable loss of resolving power associated with increased diffusional effects within the mobility cell as a direct result of increased Brownian motion. Figure 3.1 compares ion mobility spectra of reserpine ($M_w=608.28$ Da) at temperatures of 155, 125, 95, 65 and 25 °C obtained with a 400 μ s ion gate pulse width, 10,320 V drift voltage, 15,000 V nanoESI voltage, and 0.6 L·min⁻¹ N₂ drift gas. At 25 °C an intense peak corresponding to solvent clusters is observed at 36.2 ms, while peaks associated with reserpine are observed at 55.2 and 60.5 ms. As the temperature is increased to 155 °C, a loss of resolving power occurs and peaks shift to shorter drift times; 21.8 ms for the solvent and 37.6 and 42.2 ms for the reserpine peaks. Also, the intensity of the solvent peak decreases, while the intensity of the peaks associated with reserpine increases. Similar results were observed by Hill et al., who proposed that the shift to shorter drift times was caused by a decrease in clustered solvent ions associated with more efficient desolvation.⁴¹ During the course of these and following experiments, it was observed that the intensity ratio of the solvent and reserpine peaks was heavily dependent on the concentration of acetic acid in the electrosprayed solution. This dependence causes variations in signal intensity over a period of several hours as the acid in the sample container evaporates. It was concluded

that an insufficient concentration of acetic acid accounted for the small reserpine signal observed in the experiments presented in Figure 3.1. In following experiments, the concentration of acetic acid in the sample solution was kept as close to the optimum value of 0.1 % as possible. As a conclusion from these temperature-resolved experiments, we decided that in order to maximize resolving power, all subsequent experiments would be performed at 25 °C.

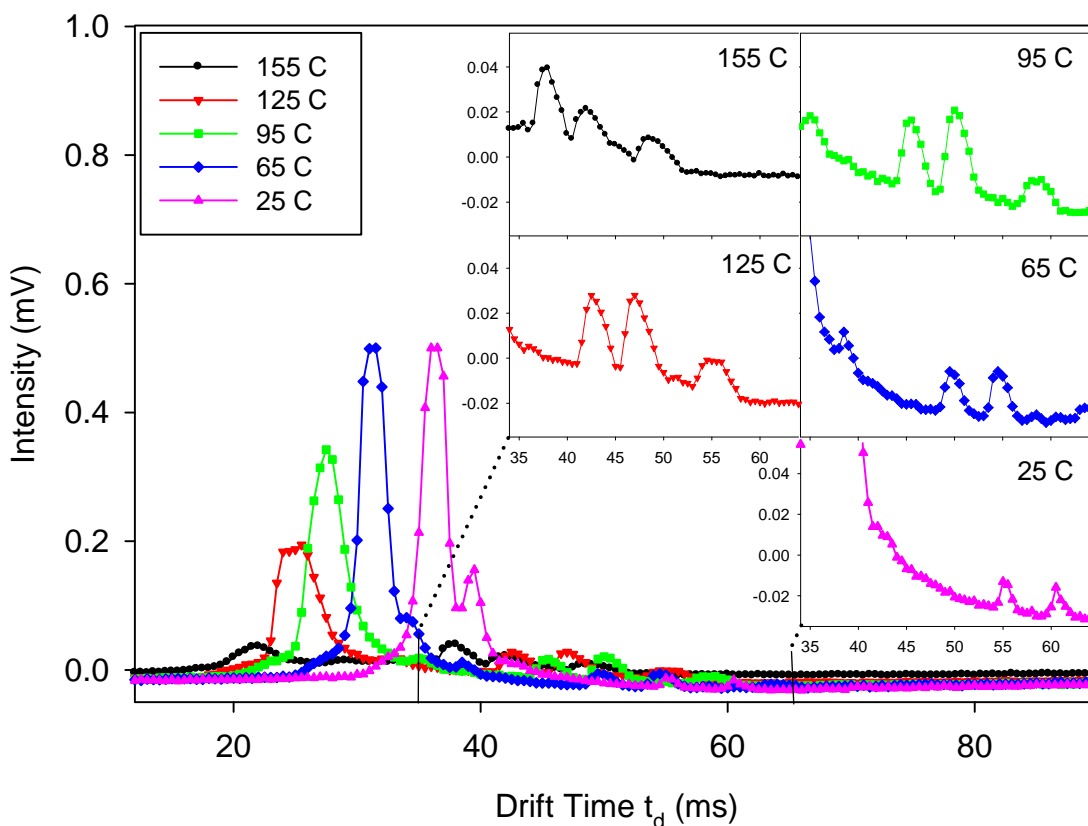


Figure 3.1 NanoESI ion mobility spectra produced by analysis of 80.0 fmol of reserpine showing the effect of temperature (155, 125, 95, 65, and 25 °C) on drift time and signal intensity of the solvent and reserpine species.

3.4.4. Drift Gas Effects in our Prototype DTIMS

Next, the effect of drift gas flow rate on the separation of the reserpine monomer and dimer was investigated. Drift gas serves not only to desolvate ions, but also acts as the separation medium in DTIMS therefore, increasing the drift gas flow rate increases the frequency of ion-drift gas collisions and should improve the separation. Figure 3.2 shows ion mobility spectra of reserpine at N₂ drift gas flow rates of 0.40, 0.77, 1.10, and 1.40 L·min⁻¹ obtained with a 200 μs ion gate pulse width, 10,320 V drift voltage, 15,000 V nanoESI voltage, and at 25 °C. Select data points are plotted in Figure 3.2 for clarity. As the drift gas is increased from 0.4 to 1.40 L·min⁻¹, the solvent peak shifted to a slightly shorter drift time from 40.8 to 40.2 ms, with a corresponding decrease in intensity. This decrease is associated with increased desolvation and declustering similar to that observed in Figure 3.1. However, the exact opposite effect was observed for the reserpine monomer and dimer peaks in this case. As the drift gas is increased from 0.4 to 1.40 L·min⁻¹, the reserpine peaks shifted to longer drift times from 56.6 and 62.8 ms to 57.4 and 63.1 ms, with a corresponding increase in intensity. We propose that the shift to longer drift times is caused by the increased drag force and increased frequency of collisions experienced by the ions as the drift gas flow rate is increased, which influences how the ions travel down the drift tube, while the increase in intensity is associated with more efficient desolvation. A drawback associated with the higher drift gas flow rates is that the peaks have a less Gaussian like shape and have a more distorted tailing edge. We believe this is caused by an inhomogeneous drift gas flow from behind the detector that is distorting the periphery of the ion packets. Based on these observations, the drift gas

induction port was later modified with the addition of a custom-build gas diffuser to help minimize flow inhomogeneities.

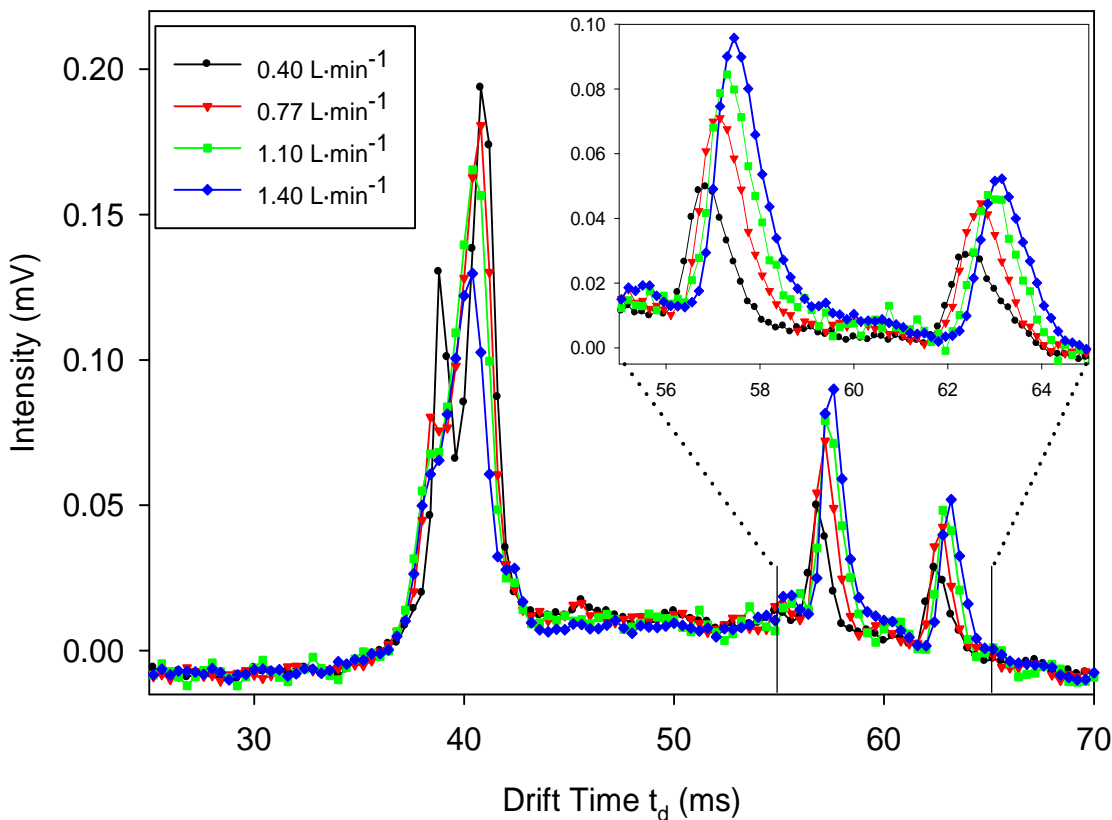


Figure 3.2 NanoESI ion mobility spectra produced by analysis of 40.0 fmol of reserpine showing the effect of N₂ drift gas flow rates (0.4, 0.77, 1.10 and 1.40 L·min⁻¹) on drift time and signal intensity of the solvent and reserpine species.

3.4.5. Anode-to-Anode Grid Distance Effects in our Prototype DTIMS

Once the effects of parameters such as temperature and drift gas were better understood and optimized, the effect of modifying the anode grid to anode detector distance was studied. The purpose of the anode grid is to prevent the electric field of the arriving ion cloud from inducing a capacitive current flow on the Faraday plate detector

prior to the ions striking the plate, thus effectively preventing the formation of an image current. Variable grid-detector distances were tested by placing an increasing number of metal spacers behind the anode detector. Table 3-1 shows the resolving power values obtained for reserpine, using the default anode grid-detector configuration (5 mm distance) and also 0.7 and 1.5 mm distances at a fixed ion gate pulse length of 200 μ s collected with a 10,300 V drift voltage, 15,000 V nanoESI voltage, 25 °C, and a 0.6 L·min⁻¹ N₂ drift gas. Spectra corresponding to these experiments are shown in Figure 3.3. The peak at 49.4 ms was again attributed to clusters originating from the acetonitrile:water solvent mixture, while the peaks at 62.2 and 93.5 ms are attributed to the reserpine monomer and dimer, respectively.

Table 3-1 Resolving powers obtained from nanoESI DTIMS analysis of 15.5 fmol of reserpine showing the effects of varying the anode to aperture grid distance.

Anode to Grid Distance	Solvent Peak (ms/ms)	Reserpine Peak (ms/ms)	Reserpine Dimer Peak (ms/ms)
5.0 mm	36	33	41
1.5 mm	45	40	50
0.7 mm	56	50	67

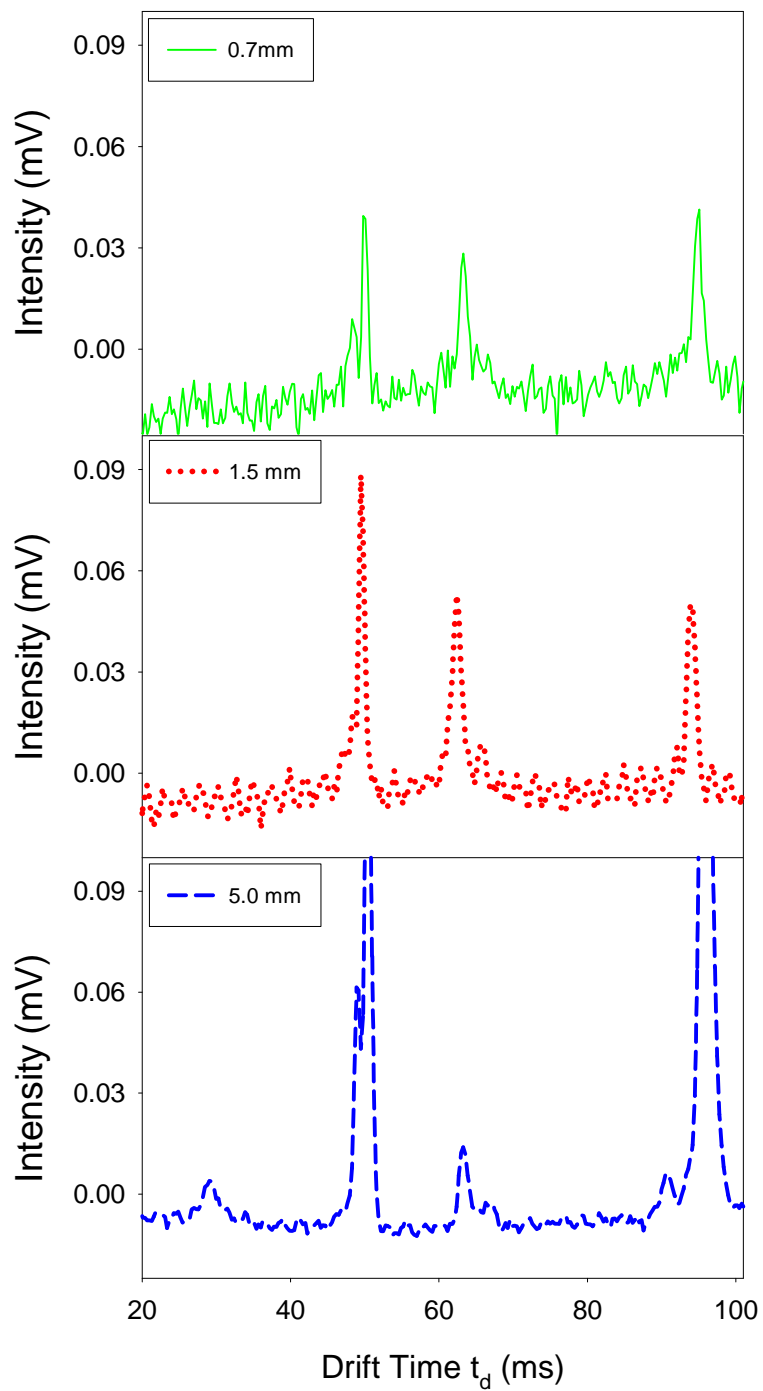


Figure 3.3 Typical DTIMS spectra obtained from the injection of a total of 16 fmol of reserpine into the drift tube, observed at anode grid-to-anode distances of 5.0, 1.5, and 0.7 mm. Resolving power values are reported in Table 3-1.

As stated previously, variations in the concentration of acetic acid due to evaporation caused changes in the intensity ratio of the solvent and reserpine peaks. In the experiments depicted in Figure 3.3, the concentration of acetic acid was increased to 0.15 % in an attempt to minimize such changes. The higher concentration of acid caused the formation of what we believe to be a proton-bound dimer, with an appearance and intensity dependent on the concentration of acetic acid in the electrosprayed solution. This dependence accounts for the smaller reserpine monomer signal and larger dimer signal observed at the 5.0 mm anode to anode grid distance when compared to the 1.5 and 0.7 mm distances, as the spectra shown in Figure 3.3 were sequentially collected from the same reserpine solution. Although the dependence of signal intensity on acetic acid concentration may slightly skew the resolutions calculated in Table 3-1, the overall trend indicates that resolving power systematically increased with a decrease in anode to aperture grid distance. Reducing the spacing from the 5 mm default configuration to 0.7 mm resulted in a significant increase in resolving power due to the decoupling of the image current from ion detection. Measured resolving powers ranged from a minimum of 33 ms/ms (6,100 theoretical plates) for a 5 mm distance, to a maximum of 67 ms/ms (approximately 25,000 theoretical plates) for a 0.7 mm distance.

3.4.6. Ion Gate Pulse Width Effects in our Prototype DTIMS

Figure 3.4 shows typical spectra obtained at varying ion gate pulse lengths. The data was collected with an anode to aperture grid distance of 0.7 mm and a 10,320 V drift voltage, 15,000 V nanoESI voltage, 25 °C, and 0.6 L·min⁻¹ N₂ drift gas. The spectra were produced by nanoESI analysis of reserpine using 400, 200 and 100 μs ion gate pulses,

respectively. The total amounts of reserpine injected into the drift tube in each case were 31, 16, and 8 fmol. Resolving power ranged from an average value of 50 ms/ms for a 400 μ s ion gate pulse, up to an average value of 68 ms/ms for a 100 μ s ion gate pulse. A maximum resolving power of 76 ms/ms was observed for the reserpine dimer with a 100 μ s gate pulse. In all cases, an increase in resolving power was observed for shorter ion gate pulses, as expected. Experiments with 50 μ s ion gate pulses showed insufficient signal-to-noise ratio, making the calculation of the experimental resolving power challenging, and thus, they are not presented here. For comparison purposes, Table 3-2 shows resolving power values reported in the recent literature for stacked-ring standalone atmospheric pressure DTIMS instruments.^{38, 44, 102, 127} Only references describing standalone instruments with Faraday plate detectors and where resolving power values were reported are included in Table 3-2. Ion mobility instruments with MS detection tend to offer higher resolving powers due to enhanced analyte desolvation and sampling of only the most homogeneous portion of the ion cloud, and thus they were not included here. Although a direct head-to-head comparison between the resolving power obtained with the prototype IMS characterized here and ion mobility spectrometers described in the literature would not be completely accurate due to differences in tube lengths, drift voltages and ion gate pulse lengths. By comparing the results in Figure 3.4 with Table 3-2, it can be seen that the resolving power range obtained with the prototype resistive glass instrument is comparable, or in some cases higher, than previously reported values in the literature. This suggests that resistive glass holds significant potential for developing new ion mobility instrumentation and should be tested further.

We expect that additional optimization of this prototype spectrometer and its coupling to a mass spectrometer will yield even higher resolving power values.

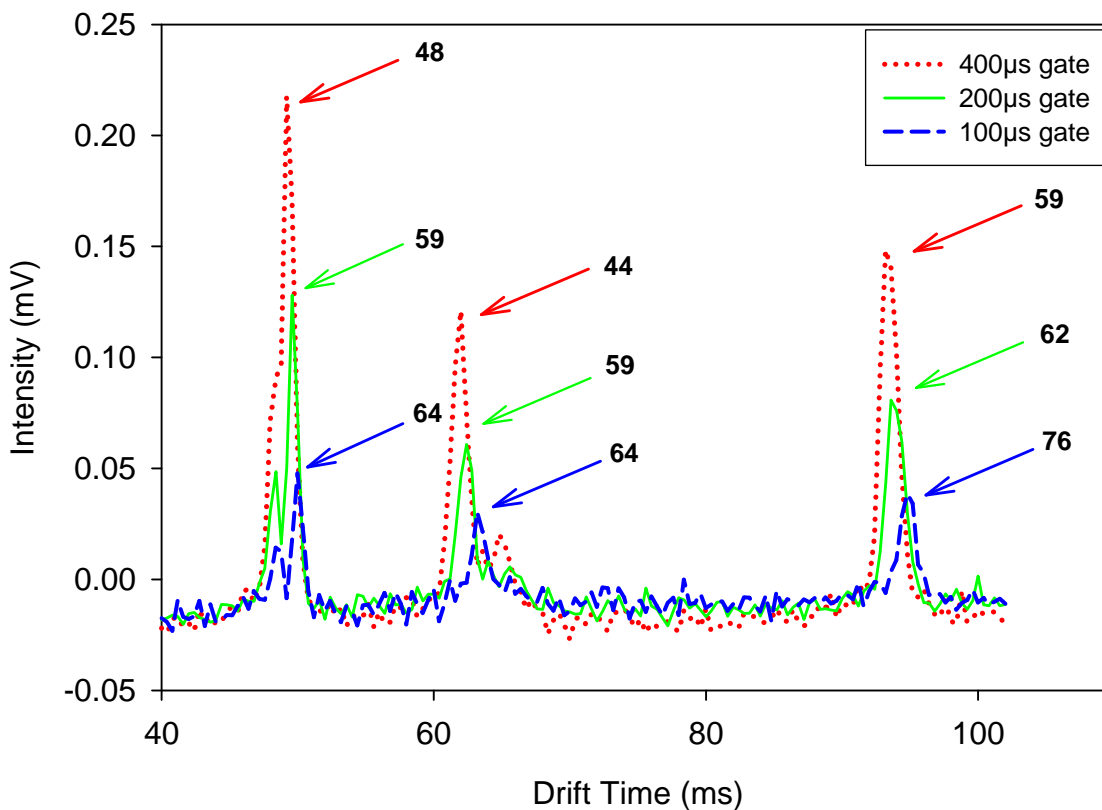


Figure 3.4 NanoESI ion mobility spectra produced by analysis of 31.0, 15.5 and 7.8 fmol of reserpine showing the effect of ion gate pulse length (400, 200 and 100 μ s) on the resolving power (indicated by arrows for each peak), for the solvent species (49.4 ms), reserpine (62.2 ms) and reserpine dimer (93.5 ms).

Table 3-2 Resolving power values recently reported for atmospheric pressure electrospray ion mobility spectrometers built with stacks of ring electrodes.

Drift Tube Length (cm)	Voltage Across Drift Tube (kV)	Operation Temperature ($^{\circ}$ C)	Typical Ion Gate Length (μ s)	Resolving Power Observed (ms/ms)	Reference
27	15.0	ambient	200	65-95	Collins and Lee ¹²⁷
11	6.6	130	300	27-59	Khayamian and Jafari ³⁸
17.4	7.7	175	50-150	44-50	Hill et al. ¹⁰²

3.4.7. Radial Ion Distributions in our Prototype DTIMS

In addition to characterizing the observed resolving power, the investigation of the shape of the ion cloud within the drift tube, as manifested by the radial ion densities observed at the detector plane, is also important for further optimization of this instrument. Radial ion densities not only have an effect on the instrument's sensitivity when operated in standalone mode, but also determine the optimum ion collection geometry for sampling the ion packet for subsequent coupling to time-of-flight or other mass spectrometric detectors. In this case, maximum sensitivity is achieved when transmission at the DTIMS-MS interface is maximized. In order to better understand the ion distribution within the drift region, and with the objective of deciding on the best configuration to later joining our prototype DTIMS to an orthogonal time-of-flight mass spectrometer, a series of experiments with detection anodes of varying diameters were conducted.

Figure 3.5 shows the ion density profiles obtained by collecting corona discharge spectra under a 6,800 V drift voltage, 10,000 V tungsten filament voltage, 25 °C and 1.7 L·min⁻¹ He drift gas with 26, 22, 17 and 10 mm diameter anodes, respectively. These profiles give a qualitative picture of the ion cloud density as a function of the distance from the longitudinal symmetry axis of the drift chamber, and were computed according to the following steps: 1) the ion current observed with each one of these anodes was integrated over the complete arrival time distribution; 2) the total charge (Q) obtained by integration ($Q=It$, where Q is the charge in coulomb, I is the current in ampere, and t is the time in seconds) was normalized by the area of the corresponding anode; 3) the ion densities obtained for a pair of two sequential anodes were subtracted from each other to

calculate the net contribution produced by an increase in anode area; and 4) these differential ion densities were plotted as a function of the distance from the drift tube center. This procedure was then repeated for various ion gate pulse lengths.

The results presented in Figure 3.5 indicate that ion density increased with increasing duration of the ion gate pulse, in an approximately linear fashion and decreased with increasing distance from the longitudinal symmetry axis of the drift chamber (see Figure 3.5 inset). Ion density rapidly decayed beyond the area not blocked by the ion gate mask (between -5 and 5 mm), suggesting that the ion beam radius followed the ion gate aperture and that no ions were lost by collision with the drift tube walls. The ion density calculated for a 13 mm distance from the spectrometer's symmetry axis was slightly negative, which is an artifact caused by the small difference in ion currents measured between the 22 and 26 mm anodes when compared to the between-run variability of our DTIMS. A qualitatively-similar radial ion distribution has been recently observed by Hill et al. for a stacked-ring IMS equipped with an ESI ion source and a target-like segmented Faraday plate detector.¹⁴¹

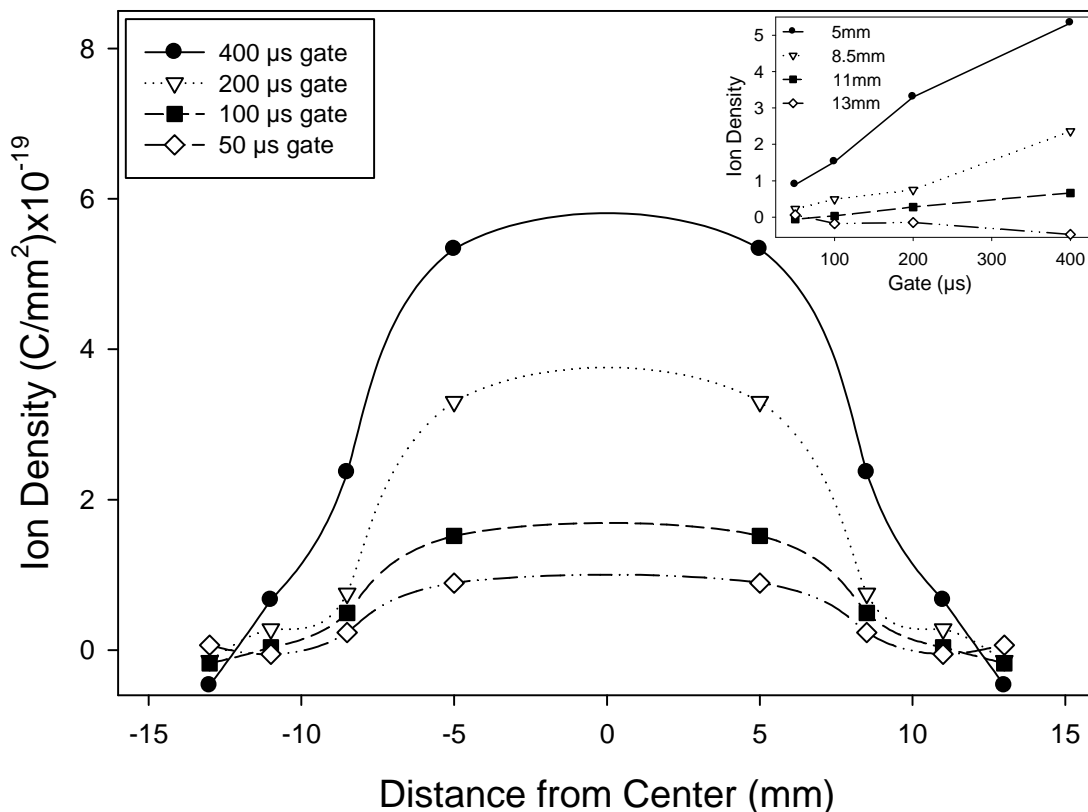


Figure 3.5 Radial ion density profiles within the resistive glass drift tube measured using detector plates with various radii and a corona discharge ion source. The inset shows ion density as a function of ion gate widths for different distances from the longitudinal symmetry axis of the spectrometer.

In terms of coupling this instrument to a mass spectrometer, the results shown in Figure 3.5 clearly indicate that for a homogeneous ion beam, such as the one produced by the prototype presented here, sampling the ion cloud with a small aperture placed at the center of the drift cell would result in the loss of a large majority of the ions. If a single micron-sized aperture is used for sampling the ion cloud after separation in the ion drift chamber, its inner diameter and length are generally chosen so as to result in a gas conductance compatible with maintaining an adequate pressure in the first differentially pumped chamber immediately after the drift cell. Russell et al. have demonstrated, both

theoretically and experimentally, that a single micron-sized aperture results in a large loss in ion transmission.¹⁴² Clearly, new approaches will be needed for more efficiently coupling atmospheric pressure ion mobility instruments to mass spectrometric detectors that operate under vacuum. If this drift cell were to be operated at reduced pressures, an ion funnel with a large acceptance aperture could be used to match the most homogeneous part of the ion density profile (-5 to 5 mm), but this approach would not be viable for atmospheric pressure IMS, as optimum focusing with ion funnels can only be achieved at pressures of a few Torr.¹⁴³

3.4.8. Application to Commercially-Available Siderophores

As a first step in applying this instrument to the high-throughput separation of small molecules in environmental samples, we analyzed a solution of a commercially-available marine siderophore, deferoxamine mesylate (DFOB), in both the free ligand and Fe bound (Fe(III)-DFOB) forms by nanoESI-DTIMS. This compound was chosen because it is a small molecule, close in size to the tuning compound reserpine, but known to undergo significant conformation changes upon binding to Fe, allowing us to explore the consequence of such a conformational change for the separation. The results obtained by nanoESI-DTIMS using a 400 μ s ion gate width are shown in Figure 3.6. The solid trace represents the solvent blank, while the dotted and dashed traces represent spectra for DFOB and Fe(III)-DFOB solutions, respectively. We hypothesize that the peak at 31.2 ms is a contaminant that is present in the Fe(III) solution, the peak at 57.3 ms corresponds to the Fe(III)-DFOB complex, while the peak at 77.6 ms corresponds to DFOB. The Fe(III)-DFOB complex has a higher mass than DFOB due to the addition of

the Fe^{+3} , therefore in a first analysis it would be expected that this increase in mass would cause the Fe(III)-DFOB complex to appear at a later drift time than DFOB. However, the change in ligand conformation upon metal binding must have a more dramatic effect than the 55.8 Da increase in mass.

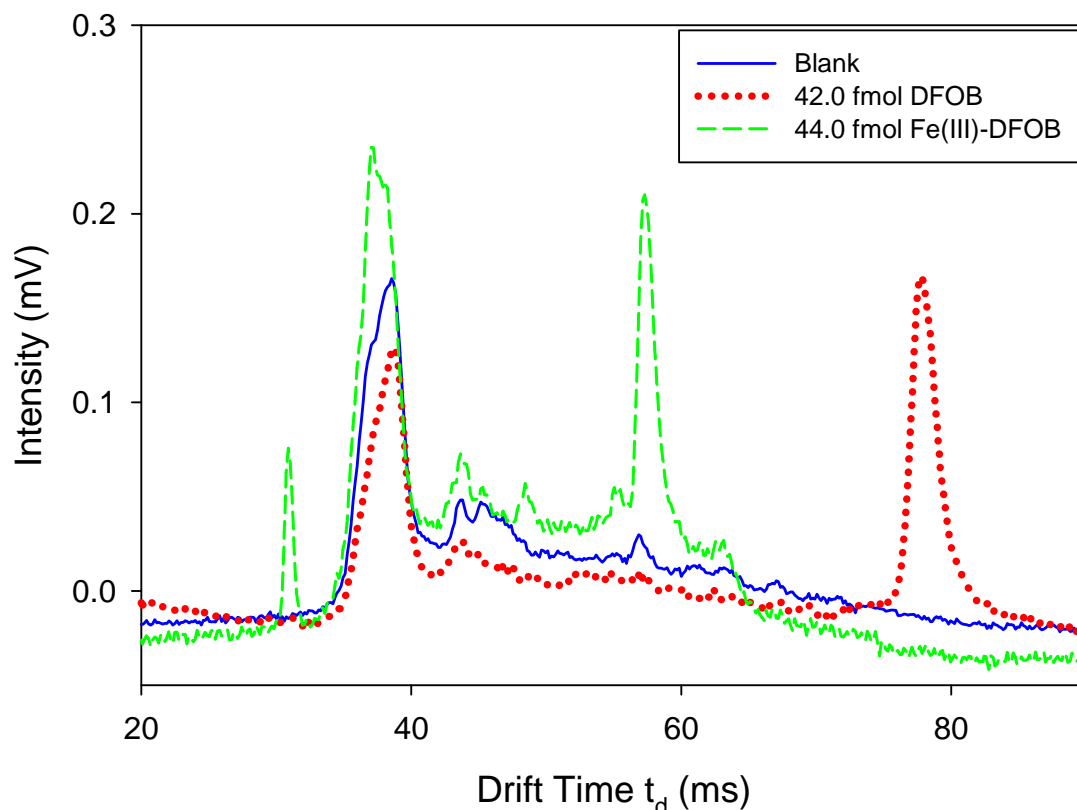


Figure 3.6 NanoESI-DTIMS analysis of solutions containing DFOB and Fe(III)-DFOB. The spectra show the analysis of a blank, 42.0 fmol of DFOB, and 44.0 fmol of the Fe(III)-DFOB complex. The peak at 31.2 ms is a contaminant that is present in the Fe(III) solution, the peak at 57.3 ms corresponds to the Fe(III)-DFOB complex with a resolving power of 45 ms/ms while the peak at 77.6 ms corresponds to DFOB with a resolving power of 41 ms/ms.

Interestingly, this behavior is analogous to what we have observed by reverse-phase HPLC when separating mixtures of DFOB and Fe(III)-DFOB; the Fe complex has a shorter retention time than the free ligand, as can be seen in Figure 3.7, so

conformation again appears to be important for explaining the chemical behavior of this system.

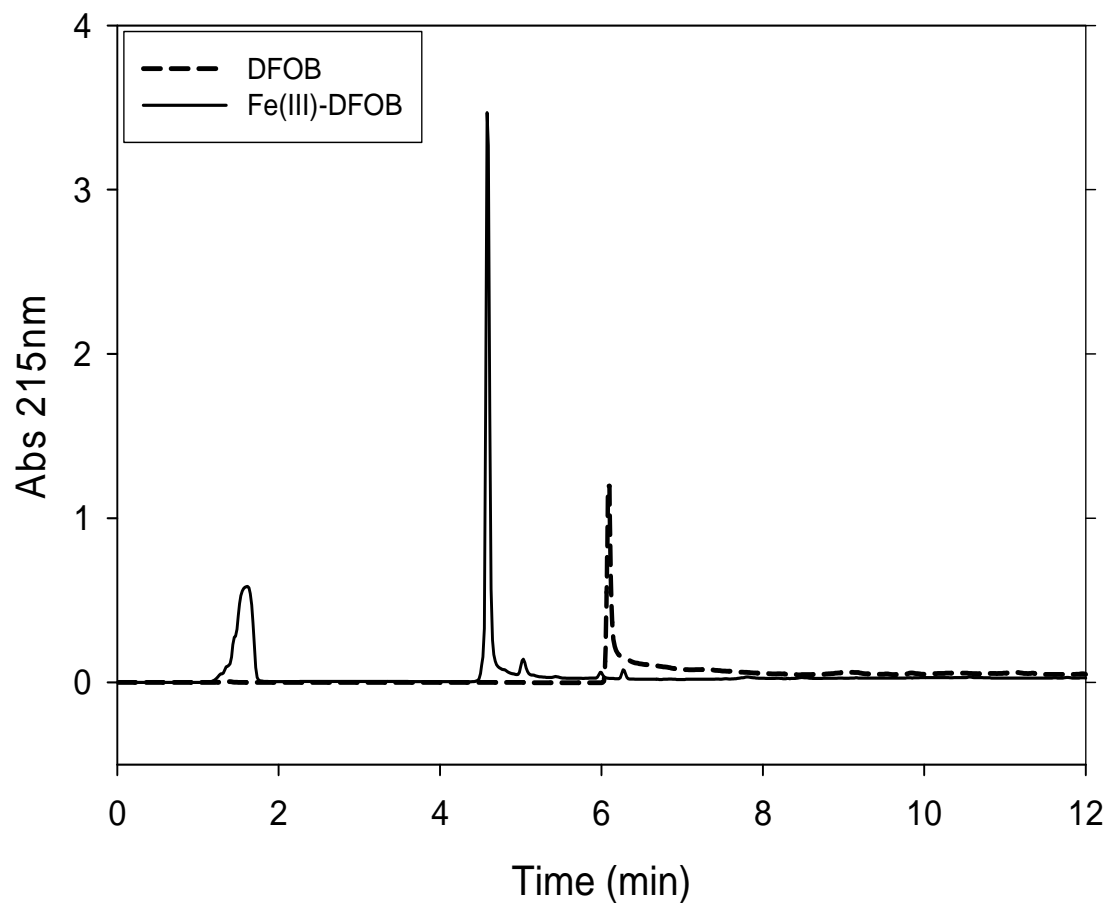


Figure 3.7 HPLC chromatograms obtained for Fe(III)-DFOB (4.7 min) and DFOB (6.1 min) on a Waters Symmetry C-18 column. The peak at 1.8 min is an unknown compound that we hypothesize is a contaminant from the Fe (III) solution.

3.5. Conclusions

The instrument presented here demonstrates the potential of resistive glass as an alternative building material to the typical stack ring electrode construction with a performance comparable to other standalone IMS reported in the literature. The monolithic resistive glass not only provides a homogenous electric field in the drift region to help maximize resolving power, but also simplifies the construction and periodic cleaning of the spectrometer.

We have investigated the effects that temperature and drift gas flow rate have on our prototype monolithic resistive glass IMS in order to understand and optimize instrumental parameters. Although higher temperature and drift gas flow rate lead to better desolvation and separation, they also lead to a loss of resolving power. It is thus preferable that they are operated at the lowest possible values required for analysis. The anode grid to anode distance has a major effect on resolving power, as decreasing this distance from 5.0 to 0.7 mm produced an average increase in resolving power of 20 ms/ms due to the decoupling of the image current from ion detection.

The radial distribution of ions within the drift tube of the spectrometer was a reflection of the ion source and ion gate mask configuration, showing that the highest density of ions was located along the longitudinal symmetry axis of the drift tube. The ion cloud was highly homogeneous in the area not blocked by the ion gate aperture mask but rapidly decayed between the mask and the drift tube walls, indicating little to no loss of ions due to collisions with the walls. The high homogeneity and ion density at the

center of the ion cloud is crucial for subsequent sampling with a mass spectrometer, helping to maximize transmission and resolution.

We have also demonstrated the ability of this instrument to provide conformational information for small molecules of environmental relevance such as DFOB, in both the free ligand and Fe-bound forms by nanoESI. Analysis showed a dramatic shift to shorter drift times caused by conformational changes upon metal binding, analogous with results observed by reverse-phase HPLC when separating DFOB and Fe(III)-DFOB mixtures.

CHAPTER 4. DIGITALLY-MULTIPLEXED NANO-ELECTROSPRAY IONIZATION MONOLITHIC RESISTIVE GLASS ATMOSPHERIC PRESSURE DRIFT TIME ION MOBILITY SPECTROMETER

4.1. Abstract

One of the shortcomings of atmospheric pressure drift tube ion mobility spectrometry (DTIMS) is its intrinsically low duty cycle ($\sim 0.04 - 1\%$) caused by the rapid pulsing of the ion gate (25 - 400 μs) followed by a comparatively long drift time (25 - 100 ms), which translates into a loss of sensitivity. Ion trapping methods, as well as multiplexing approaches via Hadamard and Fourier-type gating techniques, have been reported for increasing the sensitivity of DTIMS. This chapter explores these trapping and multiplexing methods, introduces the principles of multiplexing and describes an extended multiplexing approach that encompasses arbitrary binary ion injection waveforms with variable duty cycles ranging from 0.5 to 50 %. In this approach, ion mobility spectra can be collected using conventional signal averaging, arbitrary, standard Hadamard and/or “extended” Hadamard operation modes. Initial results indicate signal-to-noise gains ranging from 2 - 7-fold for both arbitrary and “extended” Hadamard sequences. Standard Hadamard transform IMS provided increased sensitivity, with gains ranging from 9 - 12-fold, however mobility spectra suffered from defects that appeared as false peaks, which were reduced or eliminated when using arbitrary or “extended” Hadamard waveforms for multiplexing.

4.2. Introduction

Most ion mobility instruments utilize a pseudo-continuous or continuous ionization source such as corona discharge, electrospray ionization (ESI), photoionization or ^{63}Ni chemical ionization. Utilization of this continuous stream of ions is maximized in high-duty cycle ion mobility approaches, such as differential mobility spectrometry (DMS, also known as field-asymmetric ion mobility spectrometry (FAIMS)) and aspiration ion mobility spectrometry (AIMS).

Pulsed IMS approaches such as drift time IMS (DTIMS) and traveling-wave ion mobility spectrometry (TWIMS) use time-domain separations to resolve chemical species and therefore require the creation of a discrete ion packet from the continuous stream of ions generated at the source. The most common approach for creation of these packets is utilization of an optical element such as a Bradbury-Nielson ion gate (BNG)⁶⁶ or a Tyndall ion gate⁹⁸ to inject a discrete packet of ions into the drift region of the spectrometer where separation occurs. Unfortunately, DTIMS operated in this conventional signal averaging (SA) mode suffers from the drawback that only when the closing electric potential supplied to the ion gate is shut off (i.e. the ion gate is open) will ions be separated and detected. All other times when closing potential is applied to the gate (i.e. ion gate is closed), the continuous stream of ions is neutralized against the ion gate wires.

The interval with which the ion gate is operated is called the ion injection time, or ion gate width, with typical values of 25 - 400 μs . The time it takes the species in the discrete ion packet to travel down the drift tube and be detected, either by a Faraday plate detector or a mass spectrometer, is typically in the range of 25 - 100 ms. Ion gating

events are created in a periodic fashion, following a master clocking period larger than the maximum drift time of the slowest traveling species in the ion packet to avoid overlap of ions in successive ion packets. The time scale of these events is disproportionate resulting in an experimental duty cycle, the ratio of the injection time to the total analysis time, of $\sim 0.04 - 1\%$. In other words, 99 % or more of ions generated in the source are never analyzed. The low duty cycle of DTIMS experiments severely limits the overall sensitivity of the analysis, forcing the user to increase the number of sequential runs averaged per spectrum. Effectively, this issue can translate to improper matching between the time scales of the pre- and post-separation processes, forcing the acquisition to slow down the former for improving detectability of trace analytes. Failure to do so would result in under-sampling of the stream eluting from the ion source and aliasing of its inherent chemical information. Increases in the ion injection time, although beneficial in terms of sensitivity, simultaneously decrease resolving power, and are thus not considered a satisfactory alternative in practical terms.¹⁰²

Most methods employed to increase sensitivity and improve resolving power of DTIMS experiments focus on instrumental improvements such as lengthening the drift distance, lowering drift gas temperature, increasing pressure in the mobility cell and increasing ionization efficiency prior to ion injection. An alternative approach to improve on traditional DTIMS and DTIMS-MS analysis that is described in this chapter focuses on ion trapping at reduced pressure for duty cycle improvement. Duty cycle improvements require major instrumental modifications only when ion trapping is employed, otherwise they involve smaller changes to the instrument and to the ion pulsing and detection scheme, by using a multiplexed ion gating procedure.

4.2.1. Multiplexing in Analytical Applications

In the context of analytical instrumentation, multiplexing is the process of overlaying multiple sources of information coherently along a single channel to increase the overall signal quality without a change in total sampling time. Specifically, multiplexing methods in spectroscopy and spectrometry allow multiple experimental trials to be run *simultaneously*, thereby increasing throughput. In multiplexed DTIMS, multiple packets of ions are successively injected into the drift tube instead of just one packet per master clocking period. By knowing the ion injection time, the sequence of gating events during which the gate was opened or closed, and the frequency at which the ions' arrival times, or mass-to-charge ratios were monitored, one can deconvolute the signals measured at the detector to generate mobility or mass spectra. As a result, a greater total percentage of the generated ions are available to contribute to the measured signal, resulting in an enhanced duty cycle.

4.2.2. Weighing Designs

A problem of all measurement-based fields is obtaining reliable, consistent and accurate results of whatever variable is of interest. The goal is to perform reproducible measurements with as little interfering factors as possible. A common metaphor would be the weighing of apples at a grocery store using a single pan scale. Imagine wanting to know the weight of three apples. The most straightforward way to do this is to weigh the group of apples at once to obtain the weight of the group. Although this method is time-efficient, there is only one measurement, thus it will not provide the most reliable of results since it is based on only one trial.

An improvement to this method would be to weigh each apple separately and sum the weights of all three. Although direct and simple, each step in this type of experiment could easily fall victim to any uncertainty like a fly landing on an apple during the measurement or left over water found on the bottom of the measuring pan from a previous weighing of freshly cleaned produce. Because each apple is measured only once, this design has no failsafe way of ensuring the data generated is not biased. Random noise, imprecision, instrument or environmental background, etc. all contribute to inaccurate measurement results.

How then can we improve the confidence in the obtained mass of the apples without spending any extra time at the grocery store? By utilizing a multiplexed method of placing two apples at a time into the scale in the three possible configurations (apple 1 and 2, apple 2 and 3, and apple 1 and 3), and subtracting the mass of one pair from the sum of the other two, will result in the weight of the individual apple common to the second and third pairs. All three masses of apples can then be obtained in a similar way, and summed to yield the total mass of the three apples. With this experiment, no additional time is spent weighing the apples versus weighing each apple independently, since the total number of experiments is still three. Why is this experimental design more accurate? In comparison to our “one-apple-at-a-time” experiment, the calculated SNR gain obtained with this multiplexed approach increases with $(n + 1)/2n^{1/2}$, where n is the number of apples investigated.¹⁴⁴ By multiplexing the measurements, each apple is weighed twice, allowing for a realized gain in the SNR of 15 % over weighing the apples separately.

The use of two weighing pans (equivalent to detectors in a spectrometer) could increase our SNR gains even further. Instead of weighing the apples in a single pan scale, they could be weighed in a two-pan scale with two apples placed on one pan while one is placed on the other. A similar method is followed to solve for the masses of each apple, however, by using two pans each apple is weighed in every trial since there are three possible combinations of weighing experiments. Therefore, the realized SNR gain in a dual-pan scale is 40 %.^{144, 145}

Making the leap from grocery shopping to precise, analytical measurements may seem far-fetched yet the principle of multiplexing remains the same. Multiplexing in spectroscopy involves encoding multiple independent signals so that combinations of them can be transmitted simultaneously in a controlled way, without increasing the total analysis time. Since the way the signals were initially combined (encoded) is known, the readout produced by the detector can be deconvoluted at the end of the experiment into the individual original signal components, each enhanced by SNR gains.

4.2.3. Types of Multiplexing and their Applications

Both single detector (one pan scale) and multiple detector (two pan scale) multiplexed spectroscopic experiments are possible, all resulting in improved performance,¹⁴⁶ however only single detector arrangements will be discussed here as they are more closely related to multiplexed IMS. One single detector approach for encoding spectroscopic information, known as frequency division multiplexing, allows for multiple wavelengths of light to strike the spectrometer's detector simultaneously. By modulating each wavelength of interest with a different "carrier" frequency, individual components

of the signal can be interpreted by electronic means using tuned amplifiers. Interference from crosstalk of the modulating frequencies can be a problem if they are not sufficiently different from one another. Another approach, time-division multiplexing, successively arranges incoming wavelengths to be detected for a fraction of the total scan time.¹⁴⁶ In other words, a particular wavelength is always being detected at a given time during the scan. It is susceptible to instability in the spectral sweep caused by instrumental or sample based noise that is compounded by the short scan time at any particular wavelength. Frequency-division multiplexing has been used with flame atomic fluorescence spectrometry,¹⁴⁷ fluorometry,¹⁴⁸ diode laser spectroscopy,^{149, 150} reflectometry,¹⁵¹ radiography,¹⁵² tomography,^{153, 154} Fourier transform profilometry,¹⁵⁵ and fiber optic sensors.¹⁵⁶ Time-division multiplexing has been implemented in three-dimensional integral imaging,^{157, 158} x-ray microcalorimetry,¹⁵⁹ gas¹⁶⁰ and fiber optic sensors,¹⁶¹ various rapid scanning spectrometers,¹⁶² and monochromators¹⁶³ for atomic spectrometry.

Transform based multiplexing, also a single detector approach, allows multiple spectral elements to be recorded simultaneously without loss in selectivity. Monitoring multiplexed wavelength combinations, instead of single channels can, in principle, yield improvements in SNR and spectral line shapes, aiding in increasing the spectral acquisition rate at constant SNR.^{146, 164} Based on Fourier transform (FT) and Hadamard transform (HT) mathematics, these methods rely less on physical instrument modifications than frequency-and time-division multiplexing approaches.

In FT methods, the detection of multiple frequencies is performed in the time domain, e.g., the free induction decay in a nuclear magnetic resonance (NMR)

experiment. By simultaneously measuring several spectral elements, a multiplex advantage, also called Fellgett's advantage, is obtained.¹⁶⁵ The data digitized in time can be connected mathematically via the fast FT (FFT) to the frequency domain. This leads to the additional possibility of enhancing the analytical information by removing unwanted components in the frequency spectrum. Apodization, digital filtering, baseline smoothing and resolution enhancement are all possible.^{146, 164} Examples of techniques that make use of FT multiplexing include ion cyclotron resonance MS,¹⁶⁶ IMS,¹⁶⁷ quadrupole resonance,¹⁶⁸ dielectric,¹⁶⁹ microwave,¹⁷⁰ NMR,¹⁷¹ UV/Vis¹⁷² and IR spectroscopy.¹⁷³ As with FT methods, transform methods based on Hadamard mathematics have also proven to be powerful, but because of their particular importance to the field of IMS and work with our prototype monolithic resistive glass DTIMS, we describe them in detail in the next section.

4.2.4. Hadamard Multiplexing and the Fellgett Advantage

Traditionally, DTIMS is performed in the SA mode. The BNG is quickly pulsed open delivering a small packet of ions to migrate within the drift region until they are detected (Figure 4-1). The total time for the experiment between gating pulses (i.e. the master period) is often referred to as the sweep or acquisition time. After a given sweep is completed, the BNG is pulsed again followed by detection during the drift time. This process is repeated many times until a spectrum with sufficient signal-to-noise is acquired. The drawback of this operational mode is that each sweep suffers from low duty cycle. In the best-case scenario, the total ion utilization approaches 1 %.

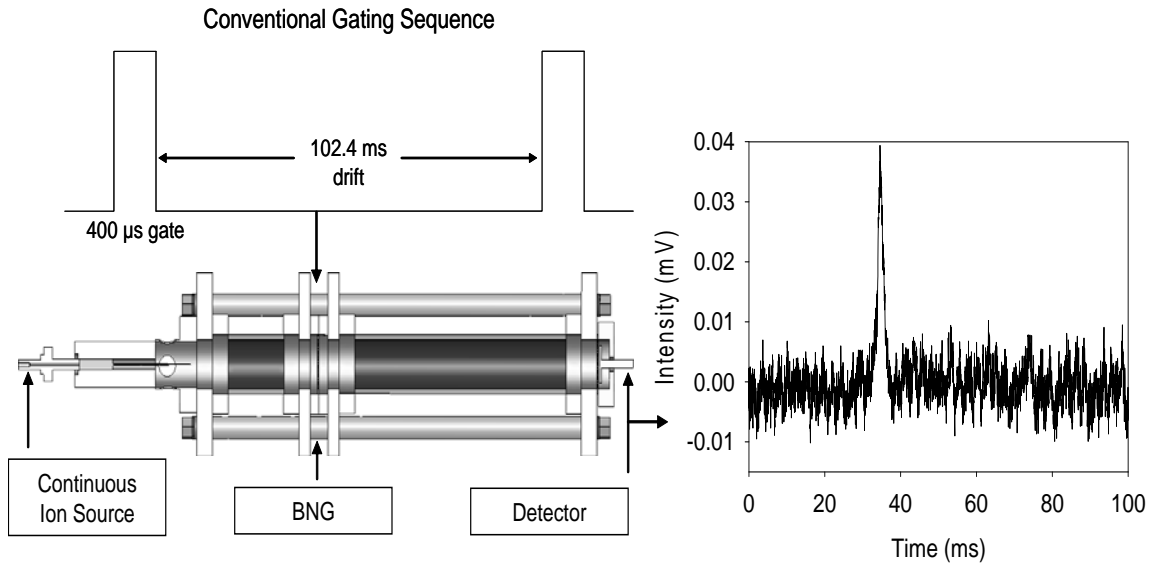


Figure 4-1 Conventional SA DTIMS gating sequence and acquired spectrum. The gating sequence is shown with typical values, but these are generally user selectable.

As a way to improve the throughput of the experiment and SNR of DTIMS, a HT-based multiplexing experiment can be utilized. HT multiplexing uses a binary code arranged in a matrix to determine which combination of ions with different mobilities is present at any given time within the drift tube. In other words, the code used for gating represents successive opening and closing events of the BNG. A mobility spectrum (ion current versus drift time in a standalone DTIMS) is produced by the deconvolution of the acquired multiplexed data points by the application of the fast HT, often resulting in gains approaching the theoretical multiplex, or Fellgett's advantage.¹⁶⁵ The binary code is derived from a Hadamard matrix (H_n) composed of ones (1) and minus ones (-1) of size n such that the dimensions of the matrix are $n \times n$. Hadamard matrices must have their scalar product of any two different rows equal to zero as shown in Equation 4.1

$$H_n H_n^T = nI_n \quad (\text{Eq. 4.1})$$

The superscript “T” denotes the transpose, and I_n is the $n \times n$ identity matrix.¹⁷⁴ In HT-DTIMS, the spectral elements are either present or omitted reflecting when the BNG is open or closed. Therefore, the experimental design is better represented by a Simplex matrix (S_{n-1}) created by replacing the ones of the Hadamard matrix with zeros (0) and minus ones with ones (1), correlating to the opening (1) and closing (0) events of the BNG. Further modification of the Hadamard matrix involves deleting the first row and column of the matrix (by definition all ones) for the creation of the S_{n-1} matrix of order $n-1$. Simplex matrices must satisfy all conditions in Equation 4.2 where J_n is the $n \times n$ matrix of ones.¹⁷⁴

$$\begin{aligned}
 S_n S_n^T &= \frac{1}{4}(n+1)(I_n + J_n) \\
 S_n J_n &= J_n S_n = \frac{1}{2}(n+1)J_n \\
 S_n^{-1} &= \frac{2}{n+1}(2S_n^T - J_n)
 \end{aligned}
 \tag{Eq. 4.2}$$

Making a Simplex matrix practical for use involves making it cyclic. In replacement of several different n sequences to apply to the BNG, one long coding sequence can be generated with the reading frame of the experiment shifting down along the series following the length of $2n - 1$. For example, if we chose a reading frame for the conventional SA sweep to be five bits (units)-long it would then resemble:

1 0 0 0 0

If there were five total runs in the entire SA experiment, this experiment would be represented as:

```
1 0 0 0
1 0 0 0
1 0 0 0
1 0 0 0
1 0 0 0
```

When applied to the BNG, the sequence would look like:

```
1 0 0 0 0 1 0 0 0 0 1 0 0 0 0 1 0 0 0 0 1 0 0 0 0
```

A corresponding 5 x 5 Simplex matrix used for a HT multiplexed experiment could resemble:

```
1 0 1 0 1
0 1 0 1 1
1 0 1 1 0
0 1 1 0 1
1 1 0 1 0
```

The applied sequence to the BNG has length $2n - 1 = 9$ so that the final zero in the gating sequence is omitted. The actual experiment is based on the following sequence of gating events:

```
1 0 1 0 1 0 1 0 1 1 1 0 1 1 0 0 1 1 0 1 1 1 0 1
```

One can now start to see the advantage of the HT multiplexing technique. The increase in number of open gate events (the 1's in the sequence) results in more ions gated into the drift tube (Figure 4-2). In SA mode, the only avenue to increase the number of ions is to increase the duration of the experiment (i.e. the averaging time). In the HT multiplexed experiment, ions overlap with one another within the drift tube while traveling towards the detector. At any given time, the detector does not “see” ions of a single ionic mobility, but predetermined combinations of ions of various mobilities. This is in general counterintuitive, but is equivalent to a multiplexed optical spectrometer where photons of several wavelengths strike the photomultiplier at the same time. The key point is that there is *a priori* knowledge of the encoded sequence for the ion injections that is used to deconvolute the acquired signal. Implementing a coding sequence with an equal number of ones and zeros, we realize a 50 % duty cycle without added instrument complexity, such as an additional ion gate as in FT-DTIMS.^{167, 175}

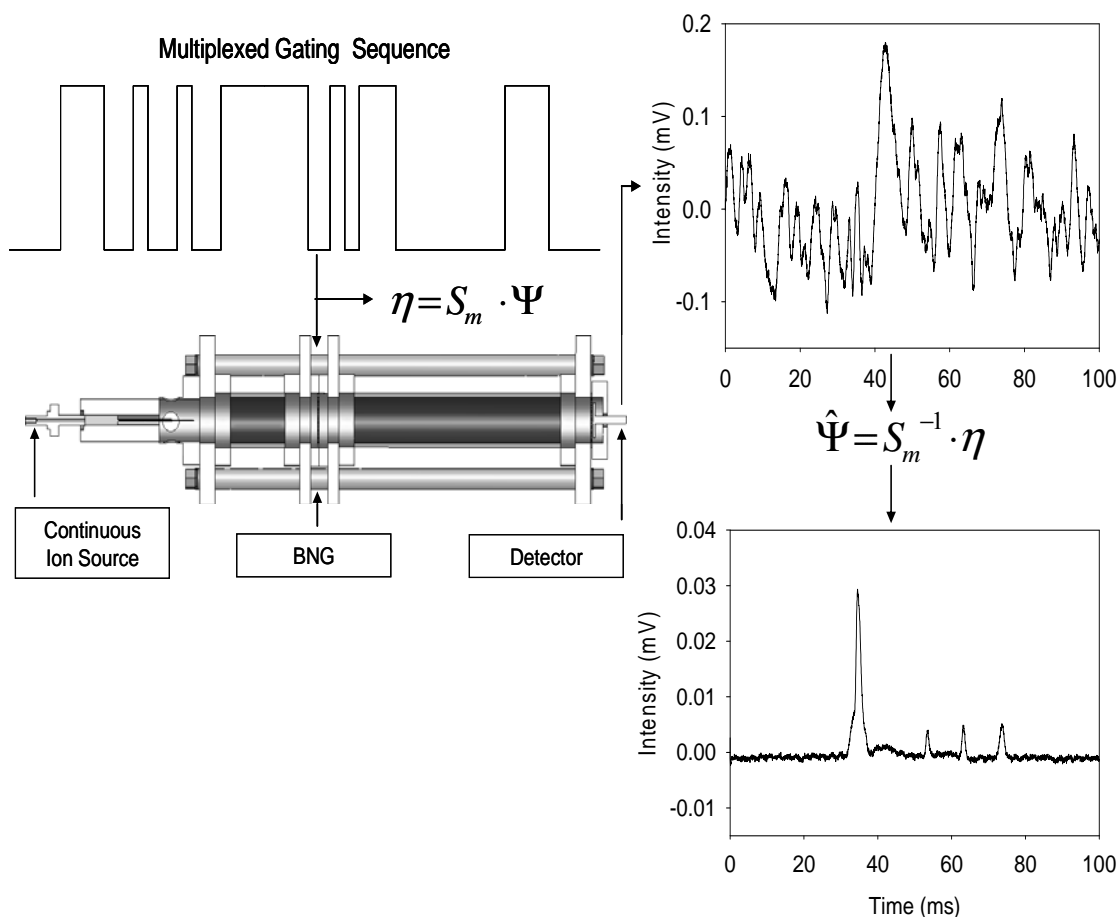


Figure 4-2 A representative multiplexed DTIMS gating sequence. The ion beam is modulated using a pseudorandom sequence (PRS) derived from a Simplex matrix which is applied to the BNG. This is mathematically expressed as a multiplication of the original ion mobility spectra (Ψ) by the Simplex matrix (S_m). The multiplexed spectrum (η) is collected at the detector. The deconvoluted data ($\hat{\Psi}$) is recovered by multiplication of the multiplexed spectrum (η) with the inverse of the Simplex matrix (S_m^{-1}).

It is important to remember that HT multiplexed instrumentation was initially conceived for optical spectroscopy where the detected photons travel orders of magnitude faster than the fastest modulation sequence. Unfortunately, ions traveling down a drift tube, especially at atmospheric pressure, do not travel anywhere near the speed of light. As a result, any processes that change the shape of the ion packet from a “perfect” square

pulse to a more diffuse ion cloud during the time frame of the experiment will result in less-than-ideal multiplexing gains. Space-charge and thermal diffusion along the radial and longitudinal axes of the drift tube are known to occur¹⁷⁶ in addition to ringing of the square waveform applied to the ion gate,¹⁷⁷ and ion depletion in the region between the BNG and the ion source.¹⁰² Deviations from ideal square ion packets decrease SNR gains and create “ghost” or “echo” peaks complicating spectral identification.¹⁷⁸

In addition to DTIMS,^{102, 103, 179} HT multiplexing has been applied to infrared spectrometry,¹⁸⁰ nuclear magnetic resonance,¹⁸¹ Raman¹⁸² and fluorescence microscopy,¹⁸³ capillary electrophoresis,¹⁸⁴ and gas and liquid chromatography MS,¹⁸⁵ perhaps most related to HT-DTIMS is HT-TOFMS. The increased attention towards broad range molecular mass analysis has caused greater use of TOFMS due to its excellent resolving power, practically unlimited mass range, high ion transmission and high spectral acquisition rate.¹⁸⁶ To further improve both sensitivity and speed of TOFMS, the Zare group developed a linear injection HT-TOFMS.^{177, 178, 186-190} In its original implementation, duty cycle improvements of up to 50 % and possible SNR gains of 45 - 64 for single detector configurations could be realized.^{186, 190} Further development of a dual anode detector setup saw improvements of increased signal-to-noise ratio (SNR) of 41 % over a single detector HT-TOF system while reaching the theoretical 100 % maximum duty cycle.¹⁸⁹

4.2.5. Examples of Multiplexing DTIMS and DTIMS-MS

In 1985, Hill and coworkers¹⁶⁷ were the first to address the issue of low SNR in DTIMS caused by the intrinsically-low duty cycle associated with SA data acquisition

methods. By adding a second BNG mounted at the exit of the drift tube and before the detector, and applying a square wave pulse swept from low to high frequencies between the entrance and exit gates, a duty cycle of 25 % was obtained. As the gates were swept, ion populations of a fixed mobility would appear in and out of phase with the gating events, resulting in a mobility “interferogram” that could be deconvoluted via application of a FFT. The SNR gain observed by FT multiplexing of DTIMS was approximately three-fold.¹⁷⁵ In 2004, Tarver et al.¹⁹¹ performed FT-IMS without modification of the spectrometer through the use of an external “electronic” software based gate to simulate the behavior of a physical gate. Utilizing this software based approach to “filter” select ions allowed for an improvement in SNR gain of seven. Although FT-IMS did provide significant improvements in SNR, the drawbacks associated with this approach were three-fold: (1) it was sensitive to changes in the efficiency of the ion gate especially at high pulse frequencies and the use of an apodization function was needed to remove both baseline noise and the presence of spectral echoes, (2) the 25 % duty cycle was only achieved for ion populations that were in phase with the gate pulses, and not all ions within the drift tube, and (3) in the original approach, an existing instrument had to be modified through the addition of an extra ion gate at the end of the drift tube.

A different multiplexing method was proposed by Russell et al.¹⁹² utilizing rapid injection of ions into the drift tube at a frequency much faster than could be processed by a standalone IMS using one-dimensional time correlation creating a pseudo-continuous ion beam within the drift tube. In this instrumental arrangement, a TOFMS was utilized as a rapid and sensitive detector since both IMS and TOFMS achieve separation based on time dispersion of ions. Correlated multiplexed data acquisition allowed the use of ion

injection rates much faster than that predicted to achieve 100 % duty cycle in a sequential pulse-and-wait experiment, and improved usage of the bidimensional separation space.

An alternative yet complimentary approach to multiplexing the ion injection sequence is to trap and accumulate the ions prior to injection. When working in the low pressure regime (10^{-3} - 10^{-1} Torr), ion manipulation methods utilizing both quadrupole and octopole ion traps have been successfully employed not only to accumulate ions prior to reduced pressure IMS analysis, but also to inject or gate the ions into the drift tube.^{83, 100, 193} These types of low pressure ion trapping methods provide for increased sensitivity associated with higher ion utilization resulting in gains between 60 - 100 % depending on the experimental setup. In 2001, Wyttenbach et al.¹⁰¹ made advances in the manipulation of ions in a medium pressure regime by employing an electrodynamic ion funnel that could be operated in the 0.2 Torr range to efficiently accumulate and transfer ions into the drift tube of an IMS. Over the next several years, improvements in the design and construction of these ion funnel “traps” made possible ion manipulation in the 2 - 5 Torr pressure range while enhancing ion utilization efficiency by a factor of seven.^{143, 194} With this type of setup, the drift tube is positioned between two electrodynamic ion funnels. The first funnel accumulates ions for 50 - 100 ms and injects them in 50 μ s pulses while the second funnel collects and focuses the now spatially disperse ion packets as they exit the drift tube. The second funnel then directs ions to an RF ion guide prior to mass analysis by an orthogonal TOF. Although ion efficiency was dramatically improved with this new dual ion funnel setup, the millisecond ion trapping and accumulation time was still disproportionally large when compared to the microsecond time scale of the ion injection events, and thus limited the overall ion utilization efficiency or duty cycle.

In 2007, Belov et al.¹⁹⁵ used the above mentioned dual ion funnel trap setup and applied Hadamard based pseudorandom pulsing sequences (PRS) to the ion trap for multiplexing of the ion injection events. PRS-based approaches utilize a binary, 50 % duty cycle sequence generated from the first row elements of a Simplex matrix. Through the simultaneous use of ion funnel trapping and PRS-based multiplexing, they were able to increase the duty cycle of their instrument beyond the typical 50 % associated with Hadamard based multiplexing, and realized improvements in SNR of up to 10-fold. The drawback of this method was that the ion funnel trap would accumulate ions with different efficiencies dependent on the intensity of the incoming ion beam. To correct for this phenomenon, a sample-specific weighing matrix was needed to accurately deconvolute or reconstruct the data and eliminate spectral echoes and, as such, this multiplexing method could not be universally applied. In 2008, it was proposed that by dynamically modifying the previously used PRS and trapping events to normalize the quantity of injected ions, the need for sample specific weighing matrices could be eliminated. By employing fixed accumulation times in the ion traps prior to the individual gating events, they were able to improve the robustness of the multiplexing approach. These improvements made this method amenable to a wider range of samples while concurrently achieving a 2-fold enhancement in the amount of ion injection events compared to the traditional HT-IMS experiment.¹⁹⁶ The latest advancements in the field of dynamic multiplexing now allow for the analysis of highly complex samples, such as proteolytic digests of blood plasma by IM-MS. Dynamically multiplexed IMS-TOFMS correlates analyzer performance with "brightness" of the ion source and ion funnel trapping function to minimize space charge-induced ion discrimination.¹⁹⁷ Through the

use of automated feedback algorithms to select an optimum multiplexing sequence, peptides were detected at a concentrations of 1 nM in complex mixtures with an accuracy better than 5 ppm, while providing a 3-orders of magnitude dynamic range.¹⁹⁴

Hadamard transform-based multiplexing methods applied to standalone DTIMS were implemented in 2006 by Clowers et al.,¹⁰² and Szumlas et al.,¹⁰³ with SNR gains of ~ 2 - 10. In this case, Hadamard multiplexing was performed by applying a PRS to the two wire sets of a BNG, thus injecting multiple ion packets in rapid succession into the drift tube. The pseudorandomly distributed ion packets undergo separation and are detected as an overlay of multiple arrival time distributions. This encoded signal is deconvoluted with the Hadamard transform, and thus this DTIMS approach has been named Hadamard Transform (HT) IMS.

One of the challenges associated with Hadamard multiplexing is the presence of spectral errors resulting from modulation defects. The comprehensive article by Hanley¹⁹⁸ describes the sources and manifestations of these errors in optical instruments. Kimmel et al.¹⁹⁹ presented an analysis of modulation defects in HT TOF-MS caused by imperfections in the encoding of the ion beam due to defects in rise time, ringing, and overshoot during gating events, when employing a BNG. Clowers et al.¹⁰² minimized the effect of modulation defects due to imperfect gating in HT-DTIMS by discarding the part of the multiplexed ion signal that was most affected by imperfect performance of the BNG. These authors also identified an additional source of imperfections in encoding associated with Hadamard multiplexing at atmospheric pressure, namely depletion of the ions in the region prior to the BNG.¹⁰² Hadamard multiplexing was originally developed for optical spectroscopies where the involved photons travel at speeds orders of

magnitude larger than the modulation rates. However, when the injection of ions traveling under atmospheric pressure conditions is multiplexed, the involved species have much lower mobilities and may experience depletion between closely-spaced gating events, along with thermal or space-charge induced diffusion along the longitudinal and radial axes of the drift region. The identification of modulation defects and the reduction of their effects is further complicated by the dependency of their position and intensity on the different possible PRS constructions, as demonstrated by Hudgens et al.²⁰⁰

Keeping these challenges in mind, we have implemented and investigated a flexible “digital multiplexing” method which allows for the application of user-generated arbitrary binary sequences of variable duty cycles ranging from 0.5 - 50 % to the BNG of an atmospheric pressure DTIMS instrument. These user-selected digital sequences are assembled in a new kind of matrices named “A” matrices instead of the previously described “S” matrices. By reducing the frequency of gating events employed in our variable duty cycle arbitrary sequences, the contribution of ion depletion prior to gating and the cumulative effect of imperfect gating events is mitigated in comparison to standard Hadamard multiplexing. The behavior of “extended” PRS sequences with additional “0”s appended to each original sequence element is also investigated in an effort to minimize the effects of imperfect modulation on spectral defects and maximize SNR gains. In line with our research interests, these various multiplexing approaches are applied to the nanoelectrospray DTIMS analysis of a model marine siderophore with the aim of decreasing the detection limits observed for these biologically relevant species in conventional DTIMS.

4.3. Experimental Details

4.3.6. Samples and Reagents

The solvent used for all nanoelectrospray experiments was a mixture of acetonitrile (HPLC grade, Burdick & Jackson, Muskegon, MI) and high-purity water ($18.2 \text{ M}\Omega\cdot\text{cm}^{-1}$, Barnstead Nanopure Diamond, Van Nuys, CA) in a 70:30 volume ratio. Sample solutions of tetrabutylammonium (TBA) nitrate (98 %, Acros, Geel, Belgium) were prepared and analyzed at concentrations of 50 μM . Deferoxamine mesylate (Calbiochem, San Diego, CA) samples were analyzed at concentrations ranging from 5 to 400 μM . Nitrogen (99.9997 %, Airgas, Atlanta, GA) was used as the drift gas.

4.3.7. Digital Sequence Generation

The arbitrary ion gating sequences were generated by selecting a duty cycle and calculating the number of open bins (1's) and closed bins (0's) the sequence should contain. A random number generator (www.randomizer.com) was utilized to generate a number corresponding to the position within the sequence of each open bin, covering the full range of the sequence and not allowing for repeats. The list of random numbers was used to substitute a one into the corresponding position of a zero-filled sequence of appropriate length. Sequences of length $n = 256, 512, 2048,$ and 4096 were generated for use with modulation bins of 400, 200, 50 and 25 μs , respectively, to maintain a constant acquisition time. Six arbitrary sequences were generated for each of the following duty cycles: 0.5, 1, 2, 5, 10, 30 and 50 %.

Standard pseudorandom sequences (PRS) commonly used in HT-IMS were generated using a maximum length shift register sequence (MLSRS) of $n = 2^m - 1$ with a

binary primitive polynomial of degree m , as outlined by Harwit and Sloane.¹⁴⁴ Extended Hadamard sequences were constructed starting with a PRS of length $n = 255, 511, 1023,$ and 2047 to which a user-selected number of zeroes ranging from $1 - 7$ was added after each element in the original sequence. The duty cycle of these “extended” Hadamard sequences was thus decreased from 50% to a value between $6.2 - 25\%$, depending on the number of zeroes added. All extended Hadamard sequences were zero filled to 2048 elements for more accurate comparison with a standard Hadamard S_{2047} sequences. Throughout this work, we refer to the multiplexing approach encompassing arbitrary, standard Hadamard and extended Hadamard sequences as “digital” multiplexing.

4.3.8. Signal Acquisition and Processing

A Faraday plate detector mounted at the end of the drift tube was connected to a custom-built amplifier (TOFWERK AG). Data from this amplifier was acquired and saved in tab delimited text format using a fast $12\text{-bit } 5 \text{ Msamples}\cdot\text{s}^{-1}$ A/D data acquisition board (National Instruments 6111) synchronized with the 5411 arbitrary waveform generator via its 20-MHz clock. All data was oversampled by a factor of two with respect to the modulation bin width, and 20 sweeps were averaged for all collected spectra. Duplicate runs were collected for each of the six arbitrary sequences tested per each duty cycle. These experiments were bracketed with signal averaging runs using conventional pulsing. Sensitivity changes between runs were thus mitigated by calculating a signal-to-noise gain for each arbitrary sequence tested by dividing the signal-to-noise ratio (SNR) of the deconvoluted spectrum by the SNR ratio calculated for a conventional spectrum collected immediately after the arbitrary run.

The left circulant $n \times n$ A matrices, constructed with the same methodology as the simplex matrix S_m in Hadamard multiplexing, were generated from the modulation sequences and used for subsequent data deconvolution. The original spectrum was recovered by a multiplication of the multiplexed spectrum with the pseudoinverse of the A -matrix (A^{+1}). Oversampled data was deinterleaved into individual vectors matching the dimension of the A -matrix prior to matrix multiplication, and subsequently reconstructed to produce the final deconvoluted spectrum. Pseudoinverse calculations and matrix multiplications of multiplexed data were carried out using MATLAB 7.5 (The MathWorks, Natick, MA).

4.4. Results and Discussion

In the application of digital multiplexing to DTIMS, an arbitrary binary sequence with a user-specified duty cycle is used for modulation of the ion beam. The sequence length n , also referred to as the number of individual bins, is selected such that the length of the entire modulation sequence is long enough to accommodate the drift time of the ion having the lowest mobility. Modulation sequence length is determined by multiplying the temporal duration of the modulation bin by the number of total bins constructing the sequence. Arbitrary sequences were generated with lengths of $n = 2^m - 1$, where m is a positive integer, and would thus be readily comparable to standard Hadamard PRSs. These arbitrary sequences were then used to construct a left circulant matrix called the A -matrix, with the original arbitrary sequence being used as the first row. Each subsequent row was created by removing the first element of the row, placing it at the end of the row, and shifting the remaining elements to the left by one element. This

process was repeated n -times to create an $n \times n$ A -matrix, in a similar fashion to the creation of the S -matrix used in HT-IMS. The original spectrum was recovered by a multiplication of the multiplexed spectrum with the pseudoinverse of the A -matrix, A^{+1} . Calculation of the pseudoinverse is more computationally-intensive than for the inverse, however not all of the generated A -matrices necessarily have an inverse, and therefore the pseudoinverse was employed for deconvolution of all data for consistency. Selected calculations performed using the inverse for deconvolution (data not shown) yielded the same results as those performed using the pseudoinverse, thus validating the use of this method.

4.4.1. Effects of Sequence Construction

As a first test of the proposed digital multiplexing system, experiments using sequences of the same length and duty cycle but with different constructions were conducted. Changing the position of the gating events within a sequence not only changes the mathematical properties of the encoding but, more importantly, changes the interaction between individual ion packets within the drift tube and the time allowed for the region preceding the BNG to be replenished. To investigate the effect of different constructions of the arbitrary sequences on the appearance of the IMS spectra, six arbitrary digital sequences and one evenly spaced sequence were analyzed for each duty cycle. Figure 4-3 shows spectra from the analysis of a 50 μM TBA solution collected using conventional signal averaging and arbitrary multiplexing modes. All spectra were acquired at 12.5 μs intervals with 25 μs modulation bins, and are an average of 20 sweeps. Figure 4-3A is an IMS spectrum collected in conventional “pulse and wait”

signal averaging mode employing a 0.02 % duty cycle, with the TBA signal appearing at 54.6 ms. Figure 4-3B presents the deconvoluted spectrum obtained from multiplexing with an arbitrary $A_{40\%}$ 1 % duty cycle sequence, showing the largest SNR gain of the six tested sequences compared to the signal averaging mode spectrum. As a general trend it was observed that sequences constructed with less densely packed gating events, and without any predefined order or structure imposed upon their distribution of “1”s, produced higher SNR gains. We hypothesize that varying the position of the gate closing events, “0”s, changes the density of ions in front of the BNG gate and thus the fidelity of the modulation events where ions are injected. The gate is closed by applying ± 35 V to adjacent ion gate wire sets floating at the drift tube entrance voltage. This event causes a depletion of the incoming ion cloud, changing its ion path and decreasing the ion density in front of the ion gate. This decrease becomes relatively more significant with shorter modulation widths because the proportion of depleted ions becomes a greater percent of the total amount of ions to be injected.

The spectrum in Figure 4-3C is an example of a unique baseline pattern that was observed for some tested sequences. This baseline structure, which initially appears to be noise, is actually caused by the specific distribution of gating events and is a reproducible phenomenon. Instead of the discrete spectral echoes observed in HT-IMS because of modulation defects, modulation errors in arbitrarily multiplexed IMS appear to be distributed throughout the baseline, with the magnitude of these errors varying between individual sequences. An extreme case is observed for sequences with an evenly spaced distribution of gating events (Figure 4-3D), which resulted in a marked decrease in SNR

when compared to conventional signal averaging mode, and produced similar detrimental results for all investigated duty cycles.

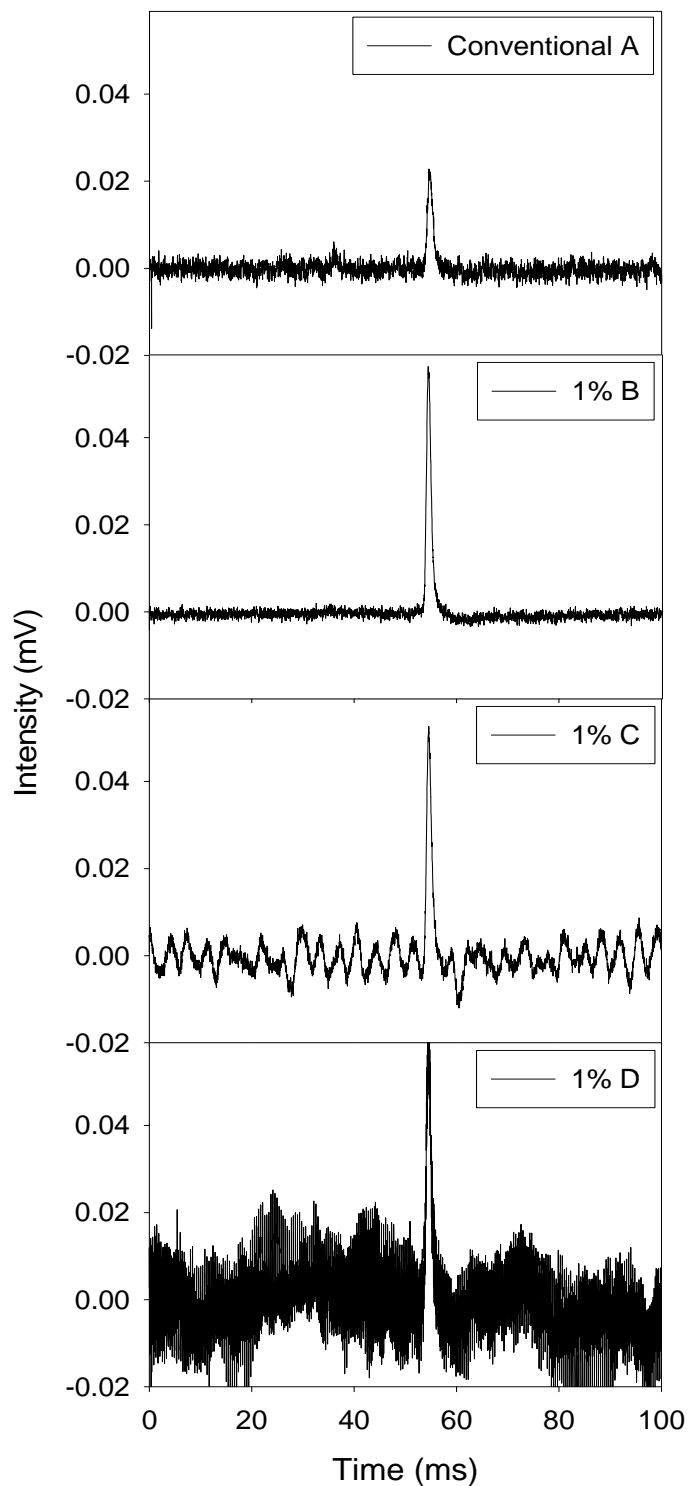


Figure 4-3 (A) Conventional SA IMS spectrum of a 50 μ M TBA solution with a 0.02 % duty cycle and (B-D) deconvoluted arbitrary IMS spectra from an identical solution representing 3 different 1 % duty cycle A_{4096} sequences. Spectra B and C represent sequences generated by randomly distributed gating events while spectrum D represents a sequence generated by an evenly spaced distribution of the same number of events.

4.4.2. Effects of Sequence Length and Modulation Width

The effects of different sequence lengths and modulation widths on sequence performance were the next parameters investigated. Due to the varying gains observed for the different arbitrary constructions, the sequence with the best SNR gain was selected and used in all subsequent investigations. SNR gains in HT multiplexing compared to conventional signal averaging mode increase with $(n + 1)/2n^{1/2}$, where n is the length of the first row of the Hadamard matrix used.¹⁴⁴ Thus, SNR gains can be improved by extending the length of the pulsing sequence. The extent to which this holds true for arbitrary sequences, however was not known *a priori*.

To investigate the inherent effect of sequence length on the performance of arbitrarily multiplexed DTIMS experiments, sequences of length $n = 256, 512, 2048,$ and 4096 were utilized with modulation widths of $400, 200, 50$ and $25 \mu\text{s}$, respectively. The combination of sequence length and ion gate duration were chosen to maintain the nominal number of total ions injected constant. For example, a 256 element, $400 \mu\text{s}$ 10% duty cycle sequence and a 4096 element, $25 \mu\text{s}$ 10% duty cycle sequence both result in a net ion injection time, assuming ideal gate performance, of 10.24 ms. However, the 4096 element sequence contains 16 -times more gating events. Therefore, it is important to investigate the spectral differences observed between these two scenarios, and whether it is preferable to operate with longer arbitrary sequences, or if negative contributions arising from the higher number of modulation defects caused by imperfect operation of the BNG at higher frequencies prevail.

Figure 4-4 summarizes the SNR gains observed for nanoelectrospray ionization of a $50 \mu\text{M}$ TBA solution at $400, 200, 50$ and $25 \mu\text{s}$ modulation widths as a function of the

percent duty cycle chosen for the ion injection sequence. Longer ion injection events (400 μs) combined with shorter sequences (256 elements) produced the lowest overall gains, with a maximum SNR gain of 2.4 occurring at a 10 % duty cycle. As the sequences are shifted to shorter injection times and larger n values, the overall gain in SNR was observed to increase, with the best performing sequence (50 μs , 2048 element) producing a SNR gain of 6.3. However, the range of optimum duty cycles for which multiplexing is highly advantageous was observed to be smaller in this case than for shorter arbitrary sequences. Significant improvement in SNR gains for longer sequences can be attributed to the distribution of experimental noise across a greater number of individual modulation bins despite the larger number of ion injection events. The trend of longer sequences producing an enhancement in SNR holds true up to a gate width of 50 μs . However, for a 25 μs 4096 element sequence this trend was not followed. A 4096 sequence produces a SNR gain of 4.8 at an optimum duty cycle range of 0.5 - 5 %. This SNR gain is 1.5-fold lower than that associated with a 2048 element sequence. We propose that the cause of this deterioration in performance is threefold: 1) the cumulative contribution of multiplexing defects caused by modulation of the BNG at the highest frequencies, 2) limits in the ability of the push-pull electronics to rapidly and accurately output a 25 μs square pulse, and 3) depletion of ions in the region prior to the BNG caused by periods of densely packed opening and closing events.

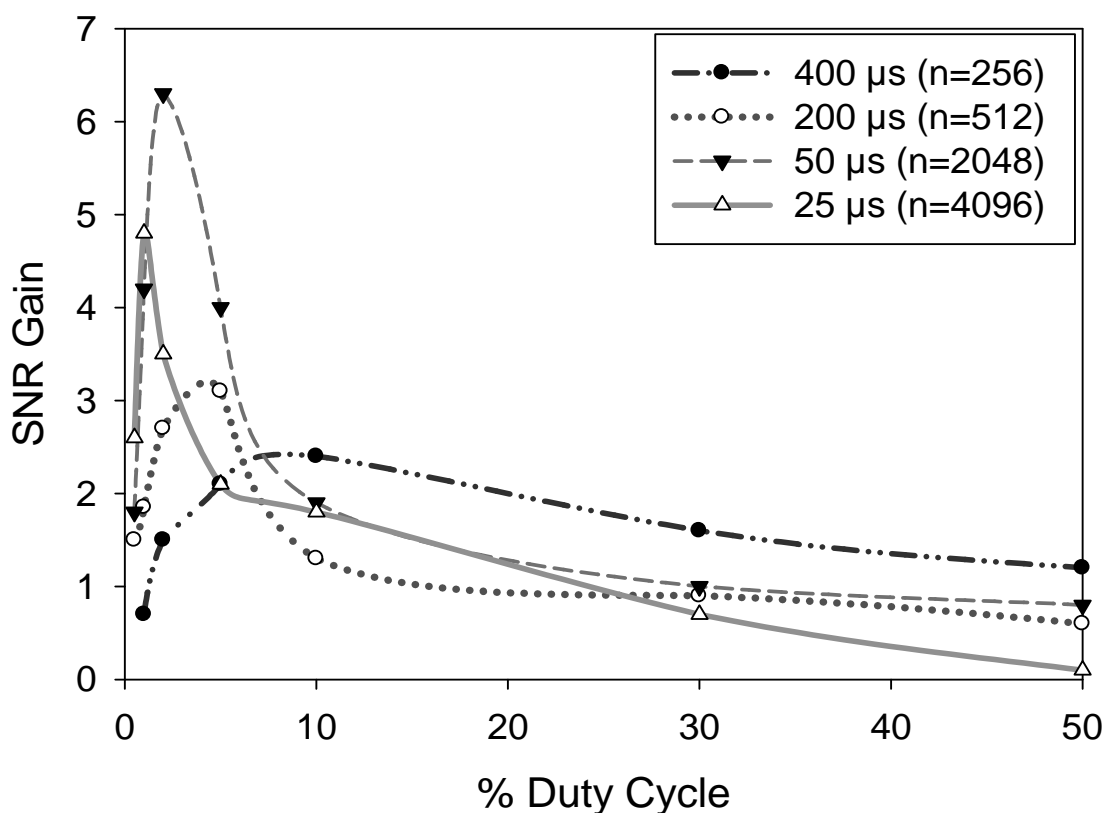


Figure 4-4 SNR gains observed for nanoESI of a 50 μM TBA solution at 400, 200, 50, and 25 μs ion gates as a function of the percent duty cycle of the ion gating sequence.

Longer ion gating events (400 μs) produced lower overall gains (2.4x) but can be operated in a wider range of duty cycles while maintaining a multiplex advantage while shorter gates (50 μs) produced higher gains (6.3x) but result in a much narrower range of optimum duty cycles for which multiplexing is advantageous.

The implementation of longer sequences with shorter injection events not only maximizes the SNR gain achieved by multiplexing, but also increases the DTIMS resolving power. IMS resolving power (R) is defined as the ratio between the drift time (t_d) and the full peak width at half-maximum (w) as shown in Equation 1.2. Revercomb and Mason¹³ identified parameters affecting ion pulse width as measured at the exit of the drift tube. In a first approximation, and assuming negligible contributions from ion-

molecule reactions, the pulse width at the detector (Δt) depends on the initial gate pulse width and the contribution of diffusional broadening as the pulse travels down the drift tube according as shown in Equation 4.1 where (Δt_0) is the initial ion pulse width, (k) is Boltzmann's constant, (T) is the drift gas temperature, (V) is the potential difference across the drift tube, (e) is the elementary charge, and (z) is the number of charges on the ion.

$$(\Delta t)^2 = (\Delta t_0)^2 + \left(\frac{16kT \ln 2}{Ve} \right) \frac{t_d^2}{z} \quad (\text{Eq. 4.1})$$

Assuming constant instrumental operating parameters, the most obvious way to increase the resolving power is to decrease the initial ion injection pulse width. From another perspective, an analyte peak width will never be narrower than the initial width of the packet of ions injected into the drift tube, however as smaller ion packets are injected, there is a dramatic decrease in sensitivity. Multiplexing IMS offers an avenue for circumventing this problem by allowing the injection of narrow ion packets of a higher ionic density, as with ion trapping methods, or at a higher frequency as in PRS and arbitrary gating approaches. In both scenarios, sensitivity is maximized without sacrificing resolving power.

The previous examples have shown that increasing the duty cycle of a sequence is beneficial in terms of SNR gain, when compared to a SA sequence with the same modulation bin width. However, the effects of increasing the duty cycle on the final measured peak width were not known *a priori* because of possible contributions from space charging within the drift tube or Coulombic repulsions between successively

injected ion packets. Equation 4.1 shows that other than diffusion, the most important factor affecting the final measured pulse width of the ion packet is the initial injected ion pulse width. Since the same ion gate width is used to inject the ion packets in both SA and multiplexed modes the performance of the instrument, in terms of resolving power, should not be affected at higher duty cycles. Experiments with 2 % duty cycle arbitrary sequences with modulation widths of 400, 200, 50 and 25 μs produced resolving power values for the TBA signal of 48, 62, 69, and 76 ms/ms, respectively. Resolving powers obtained in conventional signal averaging mode with identical modulation bin widths were within $\pm 3\%$ of the resolving power obtained in arbitrary multiplexed mode, indicating no significant change in peak widths when spectra were collected at the same modulation width.

4.4.3. Effects of Concentration on Sequence Performance

Once the effect of parameters such as sequence duty cycle and length were investigated and optimized, the effect of varying analyte concentration on the performance of the arbitrary sequences was studied. As a first step in applying this instrument to the high-throughput separation of small molecules in environmental samples, a solution of a model siderophore, deferoxamine mesylate (DFOB), was analyzed. To illustrate the concentration dependency of the arbitrary multiplexing experiment, the observed SNR gains for DFOB solutions at concentrations of 5, 25, 50, 100 and 400 μM are shown in Figure 4-5 as a function of the percent duty cycle. Sequences of length $n = 2048$ acquired at 25 μs intervals with 50 μs ion gate modulation were selected based on their optimum performance, as seen in Figure 4-4. The most

prominent gains were observed for solutions at the lowest concentration, with a maximum SNR gain of 5.3 observed for a 5 μM solution of DFOB collected at a 5 % duty cycle. As the concentration of DFOB was increased, SNR gains gradually decreased and the dependence on optimum duty cycle became less pronounced, with a SNR gain of only 2.4 observed for 400 μM DFOB at a 5 % duty cycle. We hypothesize that this effect may be caused by the smaller amount of ions entering the drift tube in conventional signal averaging mode when solutions of a lower concentration are analyzed. For example, only 0.025 fmol of DFOB are gated into the drift tube in conventional mode when working with a 5 μM solution, whereas, 2.0 fmol are gated when working with a 400 μM solution. Similar results were observed by Belov et al., who proposed that gains in SNR are most pronounced for smaller concentrations because signal averaging measurements are more limited by ion statistical considerations in the low concentration regime.¹⁹⁶ Therefore, injecting lower concentrations into a higher sensitivity DTIMS, such as what can be achieved via digital multiplexing, will provide a greater advantage over using high concentrations in an IMS with lower sensitivity. Concentration detection limits were improved from 100 μM DFOB in conventional signal averaging mode (0.5 fmol sampled), to 2 μM DFOB for a 2048 element digital sequence with a duty cycle of 5.0 % (1.02 fmol sampled).

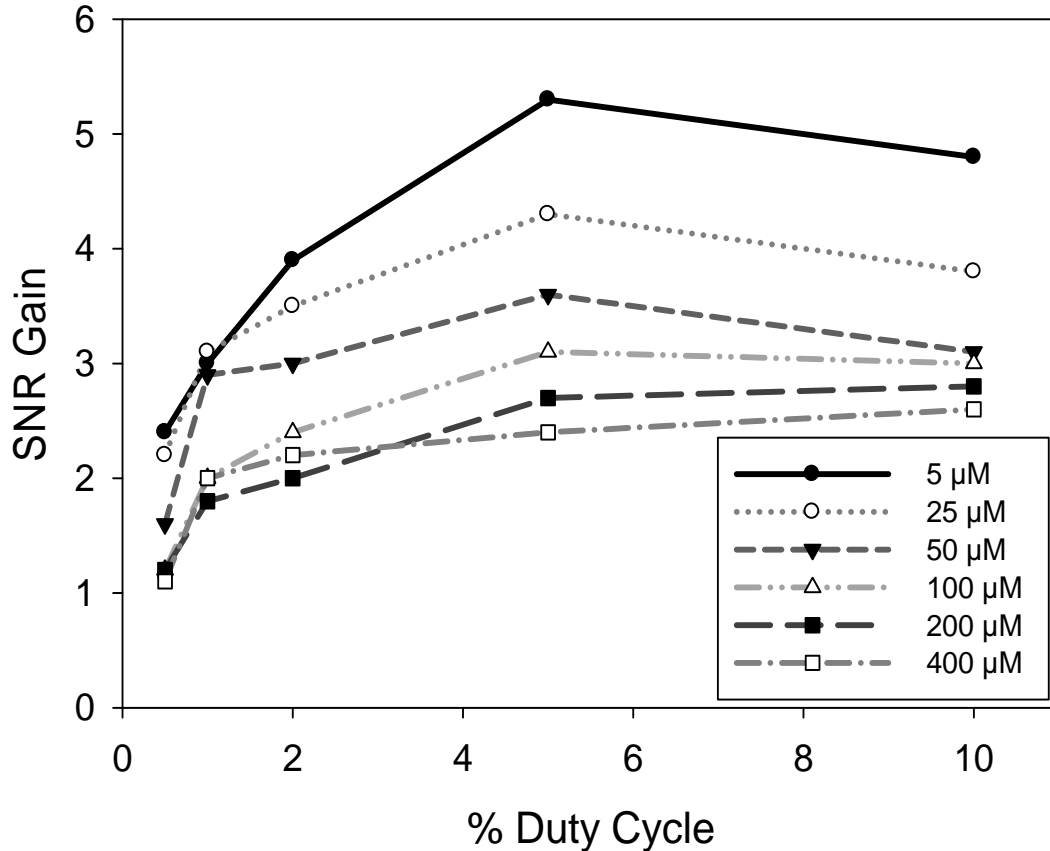


Figure 4-5 Concentration dependency of the observed multiplexing SNR gains observed for DFOB solutions at concentrations of 5, 25, 50, 100, 200, and 400 μM as a function of percent duty cycle. Gains were highest for the lowest concentrations of DFOB with 5 μM solution producing a maximum gain of 5.3x at a 5 % duty cycle. As the molar DFOB concentration was increased the overall SNR gains decreased and the dependence on optimum duty cycle became less pronounced.

4.4.4. “Extended” Hadamard Sequences

In addition to investigating the behavior of arbitrary ion gating sequences based on randomly generated numbers, extended Hadamard sequences were constructed based on a PRS generated via a MLPRS algorithm, to which a user-selected number of zeroes was added after each element in the original sequence to reduce their duty cycle. These “extended” Hadamard sequences are named by the number of elements in the original PRS followed by the number of zeroes added after each element in that sequence. For

example, a 255-7 sequence is generated with a 255 element conventional PRS and has seven zeroes inserted after each element in the sequence, resulting in a 2040 element-long sequence. By reducing the frequency of gating events in the extended Hadamard sequences, but still maintaining the general structure of the PRS, a reduction in the cumulative contribution of imperfect gating, ion depletion in the region before the BNG, and thermal or space-charge induced diffusion on spectral echoes could be achieved. PRSs were chosen as a starting point for building extended sequences because they are well-characterized and are known to be mathematically superior in terms of SNR improvements.¹⁴⁴ Figure 4-6 shows a comparison of spectra of a 5 μM DFOB solution collected in (a) conventional signal averaging, (b-c) extended Hadamard, and (d) standard Hadamard modes. Under conventional signal averaging conditions the DFOB signal appearing at 74.5 ms is barely distinguishable from the background noise (SNR=1.4) and is below the limit of detection at a concentration of 5 μM . A peak corresponding to solvent species is observed at 34.4 ms. Application of a 255-7 extended Hadamard sequence with a 6.2 % duty cycle (Figure 4-6b) resulted in a SNR gain of 3.3, while use of a 1023-1 sequence with a 25 % duty cycle (Figure 4-6c) produced a SNR gain of 5.8. The peak at 63.3 ms is believed to be a DFOB-metal complex, not clearly distinguishable in signal averaging mode, and the now visible peak at 53.4 ms arises from residual TBA contamination. The spectrum collected with standard Hadamard multiplexing utilizing a S_{2047} sequence (Figure 4-6d) showed a gain in SNR of 9.1, but suffered from spectral echoes appearing as a negative peak at 22 ms and a false positive peak at 85 ms. Although experiments with extended Hadamard sequences resulted in lower overall SNR gains, spectral echoes were not detected to the same extent as for the standard Hadamard

experiment. When comparing the performance of arbitrary sequences (Figure 4-5) with extended Hadamard sequences (Figure 4-6), the former performed better at duty cycles $< 5\%$ (60% higher gain at a 5% duty cycle). However, with increasing duty cycle, the gains produced by the arbitrary sequences began to deteriorate while that of the extended Hadamard sequences continued to increase, with a 5.8 SNR gain obtained from a 25% duty cycle 1023-1 sequence.

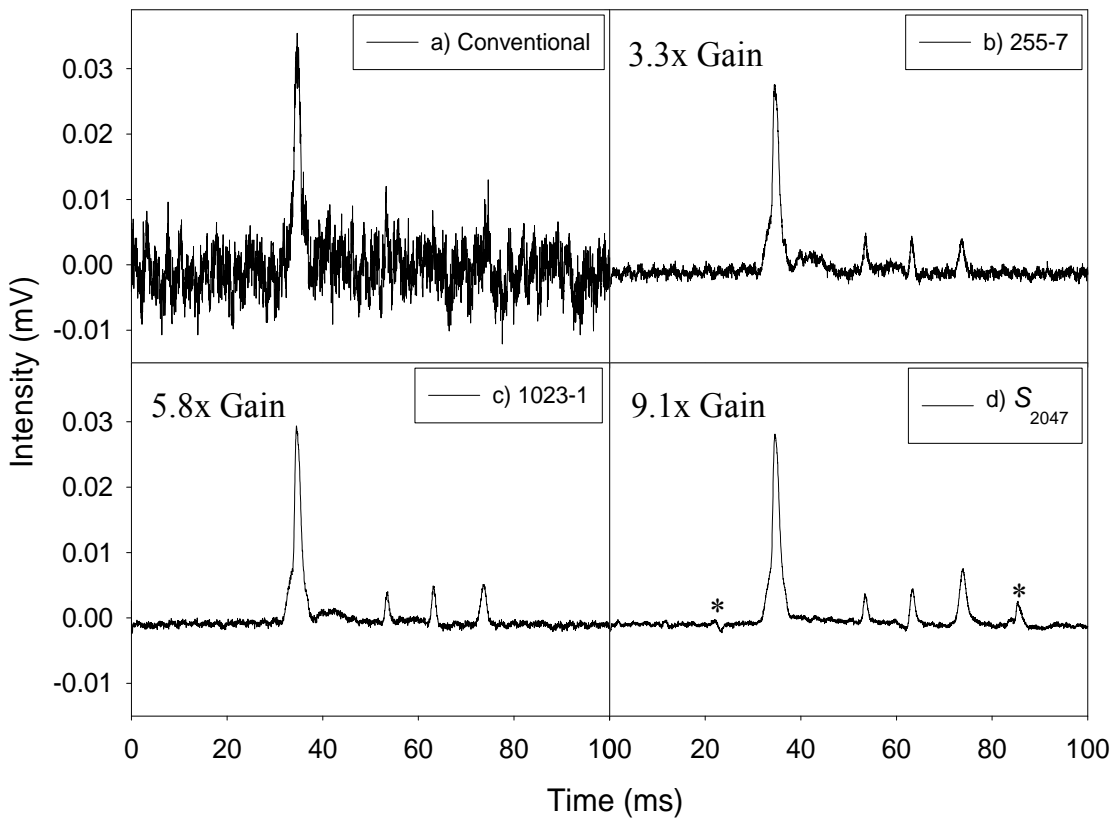


Figure 4-6 Comparison of spectra obtained for a 5 μM DFOB solution in (a) conventional signal averaging mode (0.05% duty cycle), (b) 255-7 and (c) 1023-1 extended Hadamard sequences with 6.2 and 25% duty cycles, and (d) standard Hadamard S_{2047} (50% duty cycle). Standard Hadamard multiplexing resulted in a 9.1x SNR gain but suffered from spectral defects (echoes) appearing as a negative peak at 22 ms and a false positive peak at 85 ms. Extended Hadamard multiplexing sequences 255-7 and 1023-1 resulted in lower gains of 3.3x and 5.8x, respectively, but did not generate spectral defects to the same extent as with the standard Hadamard.

4.4.5. Comparison of Hadamard and Arbitrary Multiplexing

To further evaluate the performance of the arbitrary multiplexing method with respect to HT-IMS, comparative experiments using various sequences were performed. Figure 4-7 (left panel) compares the analysis of a 50 μM TBA solution using (a) conventional signal averaging, (b) arbitrary, and (c) Hadamard multiplexing. A SNR gain of 6.3 was obtained for an arbitrary A_{4096} , 2 % duty cycle sequence, while a SNR gain of 11.4 was obtained for the corresponding Hadamard sequence. Although a higher gain is achieved in the latter case, again it was observed that the spectrum suffers from spectral echoes that appear at 42.6 and 56.2 ms. Figure 4-7 (right panel) compares the analysis of a 5 μM DFOB solution using (d) conventional, (e) arbitrary, and (f) Hadamard multiplexing with the DFOB peak appearing at 75 ms. A gain of 4.4 was obtained for an arbitrary A_{2048} , 5 % duty cycle sequence, while a SNR gain of 9.7 was obtained for the Hadamard sequence. As with the TBA example, a higher gain is achieved with the Hadamard sequence; however, the spectrum suffers from modulation defects that appear as spectral echoes at 2.8, 13.1, 23, and 86 ms. These echoes could be easily confused for a real chemical species when unknown samples are investigated.

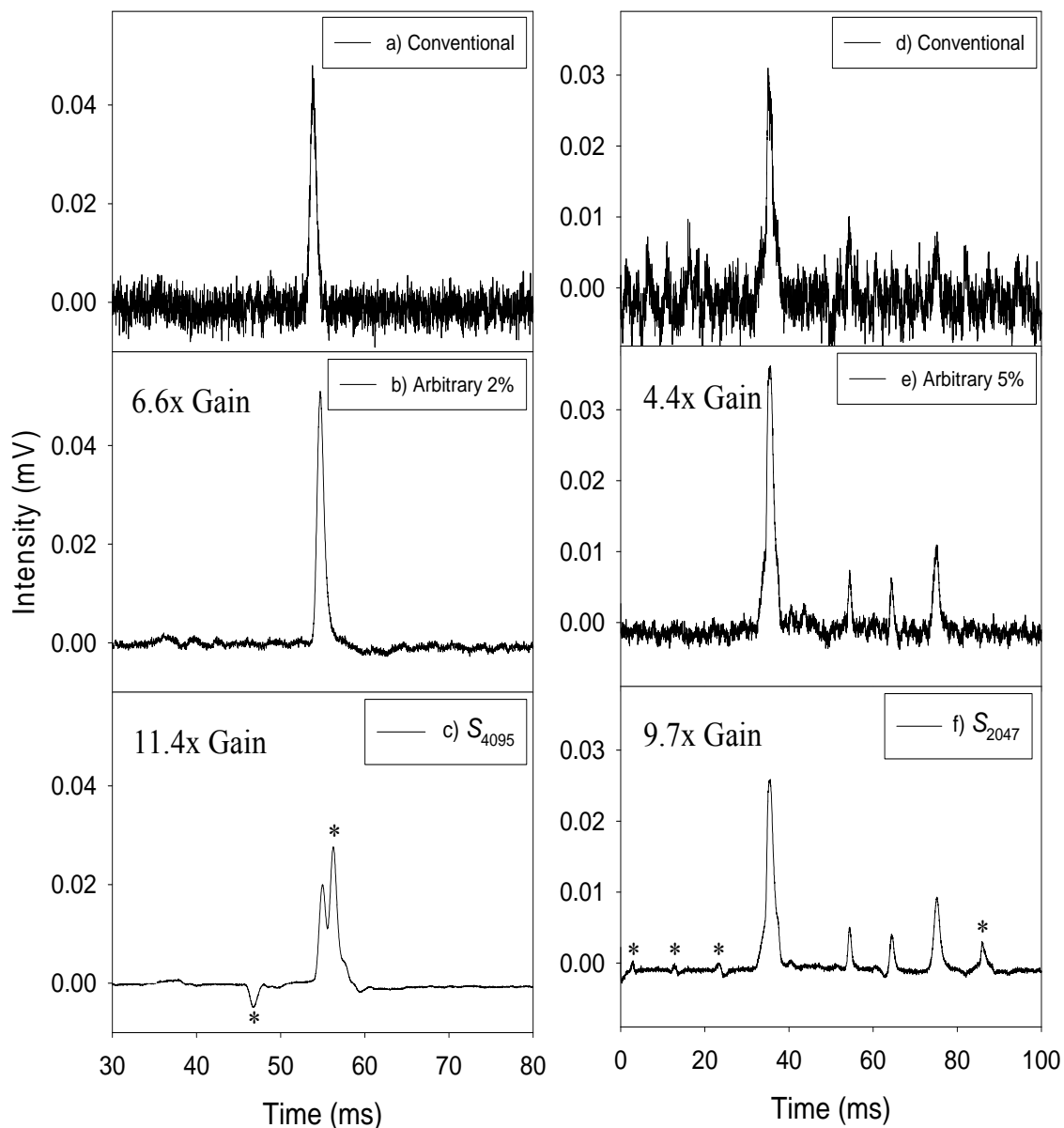


Figure 4-7 Comparison of the analysis of a 50 μM TBA (left panel) using (a) conventional, (b) arbitrary, and (c) standard Hadamard sequences and 5 μM DFOB (right panel) using (d) conventional, (e) arbitrary, and (f) standard Hadamard sequences. The DFOB $[\text{M}+\text{H}]^+$ peak appears at 75 ms. For both compounds, the SNR gains increase in the order conventional < arbitrary < standard Hadamard. However, the Hadamard mobility spectrum suffers from spectral defects labeled with an (*).

4.5. Conclusions

A new digital multiplexing method for DTIMS encompassing a variety of ion modulation schemes has been developed and evaluated as an alternative approach that enables the utilization of sequences with variable duty cycles falling outside the typical duty cycle ranges associated with conventional signal averaging mode ($< 1\%$), and standard Hadamard multiplexing (50%). The utilization of arbitrary binary ion injection sequences and “extended” Hadamard sequences produced a 2 - 7-fold gain in SNR. Experiments demonstrated that changing the distribution of gating events in a sequence not only affected SNR gains, but also the effect of modulation errors on the deconvoluted spectra. The optimum duty cycle percent for arbitrary sequences was observed to be dependent on sequence length and modulation bin size. As sequences are shifted to shorter injection times and longer sequences their multiplexing gains increase, but at the cost of a decreased optimum duty cycle range due to the cumulative effect of modulation defects. Standard Hadamard transform IMS provided greater increases in sensitivity compared to the arbitrarily multiplexed IMS, with SNR gains ranging from 9 - 12-fold. However, the HT-IMS spectra suffered from the appearance of false peaks typically present in Hadamard multiplexing techniques. Digital multiplexing via arbitrary or extended Hadamard approaches minimizes or eliminates these spectral defects without the implementation of complex spectral correction methods such as deconvolution with a sample specific defective S^* -matrix. In summary, digital multiplexing provides an alternative, tunable multiplexing scheme that can be used to increase the sensitivity of DTIMS while providing a reduction in the effect of modulation defects on the final deconvoluted spectra.

CHAPTER 5. THEORETICAL AND EXPERIMENTAL STUDY OF THE ACHIEVABLE SEPARATION POWER IN A NANOELECTROSPRAY IONIZATION MONOLITHIC RESISTIVE GLASS ATMOSPHERIC PRESSURE DRIFT TIME ION MOBILITY SPECTROMETER.

5.1. Abstract

This chapter presents a detailed investigation of the performance of our nanoelectrospray high resolution resistive-glass atmospheric pressure drift tube ion mobility spectrometer constructed with monolithic resistive-glass desolvation and drift regions. Using experimental spectral data in comparison with theoretical pulse width and diffusion variables, we compare theoretical and experimental resolving powers achievable with our instrument under a variety of field strengths and ion gate pulse widths. The effects of instrumental and operational parameters on the resolution achievable with our instrument in chromatographic terms are also discussed. Following characterization of the separation power of the instrument, experimental spectral peak width data is fitted by a least-squares procedure to a pre-existing semiempirical model developed to study contributions to peak width other than initial pulse width and diffusional broadening. The model suggests possible contributions to the final measured peak width from electric field inhomogeneity and minor contributions from instrumental parameters such as anode size, anode-to-anode grid distance and drift gas flow rate. The model also reveals an unexpected ion gate width dependence on the final measured peak

width that we attribute to non-ideal performance of the Bradbury-Nielsen ion gate and limitations in the design of our pulsing-electronics.

5.2. Introduction

Chapter 3 described the initial characterization of the performance of the nanoelectrospray high resolution resistive-glass atmospheric pressure drift tube ion mobility spectrometer by evaluating the effects of drift gas flow rate, temperature, and the radial ion density distribution within the drift space. Although these preliminary studies demonstrated the potential of resistive glass as an alternative building material for DTIMS, there were still many unanswered questions including; the homogeneity of the electric fields generated by the resistive glass, the performance of the Bradbury-Nielsen ion gate and respective pulsing electronics, and the affects of instrumental parameters such as anode size, anode to anode grid distance, and field strength within the drift tube on the performance and separation power of our prototype resistive-glass DTIMS.

As with any other separation technique, the ability of DTIMS to resolve closely spaced peaks is of paramount importance. To this end, Hill and co-workers have studied the effects of several experimental variables on the resolving power of atmospheric pressure IMS. Their results consistently showed that peaks in IMS spectra had a larger temporal width than predicted, even after accounting for differences in instrument design, initial pulse width and thermal ion diffusion. In order to rationalize these differences, they proposed that Coulombic repulsions and electric field inhomogeneities within the drift tube were responsible for the lower than ideal resolving powers observed.⁶³

As stated previously, most ion mobility spectrometers utilize a drift region built with a stack of ring electrodes, each pair separated by insulating spacers. In contrast, our DTIMS is furnished with a resistive-glass monolithic desolvation and drift chambers.²⁰¹ Resistive-glass is a lead silicate glass that has been reduced in a hydrogen atmosphere to make its surface semiconducting.¹²² Kelvin probe measurements show that resistive-glass produces highly uniform electrical fields.¹²³ The use of resistive-glass for building ion mobility spectrometers has four advantages: (1) the radial inhomogeneities in the drift tube electric field are minimized, (2) the construction of ion mobility spectrometers is simplified, eliminating the need for machining several ring electrodes and using resistor chains to generate the potential gradient, (3) the complexity of periodic cleaning and maintenance is reduced, and (4) the resistive-glass is rugged making it amicable for field applications while maintaining mechanical integrity.

In this chapter we present a detailed investigation of the performance of our high resolution monolithic resistive-glass based DTIMS²⁰¹ using experimental spectral data in comparison with theoretical pulse width and diffusion variables. We also incorporate the theory of Siems et al.⁶³ and utilize their semi-empirical models to provide a means of studying instrumental design factors and investigating their effect on instrumental performance. Contributions to measured peak widths from factors such as radial electrical field variations within the drift tube caused by the resistive-glass building material are explored. The model employed here also provides an indirect means to study the performance of the Bradbury-Nielsen ion gate (BNG)⁶⁶ in our spectrometer. These types of ion gates are known to perform non-ideally and were shown to produce ion packets with a slowly decaying population at its leading and trailing edges.⁷² SIMION modeling

has also portrayed this phenomena by modeling the distortion effects caused by wire grids on ions under atmospheric pressure conditions.^{70, 71}

IMS resolving power (R_p) is defined as the ratio between the drift time (t_d) and the full peak width at half maximum (w) as shown by equation 1.2. The shape of an IMS peak is determined by the initial shape of the ion packet injected (t_g) into the drift tube by the BNG and the diffusional broadening contribution (t_{diff}) for the ion packet as it travels through the drift space to the detector as shown by Equation 5.1. The t_{diff}^2 parameter has been expanded by Revercomb and Mason¹³ as shown in Equation 5.2.

$$w^2 = t_g^2 + t_{diff}^2 \quad (\text{Eq. 5.1})$$

$$t_{diff}^2 = \frac{16 \ln 2 k T t_d^2}{qV} \quad (\text{Eq. 5.2})$$

This expanded equation was later modified by Siems et al. to include three adjustable parameters; α , β , and γ that could be applied to experimental line width data to evaluate various contributions to experimentally measured peak widths resulting in Equation 5.3.

$$w^2 = \gamma + \beta t_g^2 + \alpha \frac{T t_d^2}{V} \quad (\text{Eq. 5.3})$$

Alpha represents the diffusion contribution to the final observed pulse width. Assuming ideal behavior, α would have a value of 0.957×10^{-3} . A larger value would

indicate effects such as field inhomogeneity, energy imparted by the electric field or other such effects. Beta describes the contribution from ion gating to the final observed pulse width. Assuming ideal gating and no diffusion, the width of the injected ion packet would be the width of the final measured ion packet yielding an ideal value of $\beta = 1$. Changes in beta would indicate non-ideal performance of the BNG or non-diffusional contributions to packet broadening such as Coulombic repulsion that would be dependent on the quantity of ions injected with each packet. Gamma is an instrument-specific constant that accounts for any parameters not affected by gating or voltage and would have an ideal value of zero.

In the work presented here, this semi-empirical model is applied to evaluate not only contributions to pulse width from factors such as field inhomogeneity and gate performance in our resistive-glass IM spectrometer, but also contributions from other instrumental parameters such as anode size, anode-to-anode grid distance, drift gas flow rate, and their effects on resolving power. Also presented is an investigation of the effect of drift voltage, anode size, anode to anode grid distance, and drift gas flow rate on the analytical separation power of our instrument, measured as the chromatographic resolution as shown in Equation 1.3.^{64,65}

5.3. Experimental

5.3.1. Samples and Reagents

The solvent used for all nanoelectrospray experiments was a mixture of acetonitrile (HPLC grade, Burdick & Jackson, Muskegon, MI) and high-purity water (18.2 M Ω ·cm⁻¹, Barnstead Nanopure Diamond, Van Nuys, CA) in a 70:30 volume ratio.

Sample solutions of tetrabutylammonium (TBA) nitrate (98%, Acros, Geel, Belgium) and tetraethylammonium (TEA) acetate tetrahydrate (99 %, Sigma-Aldrich, St. Louis, MO) were prepared and analyzed at concentrations of 150 μM . Nitrogen (99.9997 %, Airgas, Atlanta, GA) was used as the drift gas.

5.3.2. Instrumental Conditions

An electrospray voltage of + 2.5 kV versus the desolvation chamber entrance was used for all experiments. Drift gas at a flow rate of 0.2 $\text{L}\cdot\text{min}^{-1}$, unless otherwise noted, was supplied to the IMS through a custom built gas diffuser positioned behind the detector. Data collected with a modulation bin width of 100 and 200 μs was oversampled by a factor of four, while data collected with modulation bin widths of 400 and 800 μs was oversampled by a factor of eight with respect to the modulation bin width, and 100 sweeps were averaged for all collected spectra.

5.3.3. Variable Voltage Studies

Voltage dependent experiments were performed by operating both high-voltage power supplies in a synchronous manner. The instrument power supply was set to provide a 15 kV voltage to the entrance of the desolvation chamber while the electrospray power supply was operated with a voltage of + 2.5 kV with respect to the instrument power supply. Both power supplies were then adjusted synchronously to produce a 1 kV stepwise change in voltage at the entrance of the desolvation chamber. Voltage was reduced in 1 kV increments until a signal could no longer be observed. The number of voltage reduction steps was dependent on the size of the ion gate, with larger ion gates

allowing for collection of spectra at lower voltages. The voltage at the start of the drift chamber was calculated based on the starting voltage applied to the voltage divider. Measurements of drift time, peak width, and peak width at half-height were made over a range of drift voltages, ion gate pulse widths, and instrumental parameters for both TBA and TEA. Instrumental parameters such as anode size (10 and 30 mm), anode-to-anode grid (AG) distance (5.0 and 0.7 mm), drift gas flow rate (0.2 and 1.5 L·min⁻¹) and their effects on resolving power and separation power in terms of chromatographic resolution were investigated.

The information was used to calculate the change in resolving power for the two test compounds. Theoretical “ideal” resolving power was calculated as a function of voltage and gate pulse width for comparison to the experimentally observed resolving powers to determine conditions for optimal resolving power for the compounds. Voltage dependent data was then plotted, and a least-squares fit was used to determine the most accurate α , β , and γ parameters.

5.4. Results and Discussion

5.4.1. Comparison of Theoretical and Experimental Resolving Power

Figure 5.1 shows both theoretical and experimental R_p for TBA and TEA using 800, 400, 200, and 100 μ s ion gate widths and drift voltages in the range 5.84 - 11.58 kV for the 10 mm anode, 5.0 mm AG distance instrumental configuration. The blue and green traces represent the theoretical R_p for TBA and TEA, respectively, while the red and black trace represents experimentally obtained R_p for TBA and TEA. It was observed that each ion gate width has an optimal operational drift voltage that maximizes R_p , with

larger ion gate widths (top panels) performing better at lower drift voltages and smaller ion gate widths (bottom panels) performing better at higher drift voltages. Experimental performance for all ion gate widths was lower than the theoretically achievable maximum R_p . These results are consistent with work performed by Watts et al.²⁰² who showed that for a selection of three different instruments, experimentally obtained resolutions for all ion gate widths were “under-achieving” by approximately 50 %.

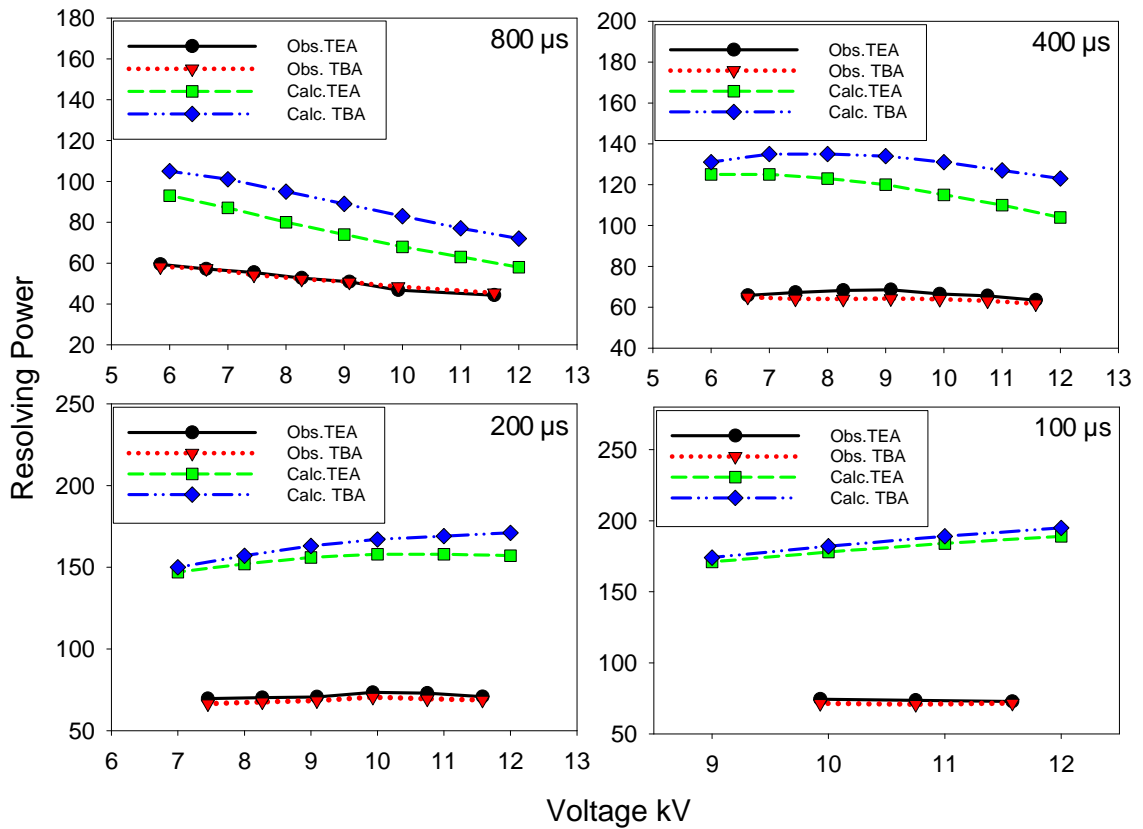


Figure 5-1 Theoretical and experimental resolving power obtained for a 150 μM TBA and TEA solution using 800, 400, 200, and 100 μs ion gate widths and drift voltages in the range 5.84 - 11.58 kV for a 10 mm anode and a 5.0 mm AG distance instrumental configuration. The blue and green traces represent the theoretical R_p for TBA and TEA, respectively, while the red and black traces represent experimentally observed values.

Detailed consideration of the data shown in Figure 5.1 reveals that the difference between theoretical and experimental R_p increased as the ion gating pulse width was made smaller. For example, the experimentally obtained R_p of TEA acquired at a 10 kV drift voltage and an 800 μ s gate was 25 % lower than the expected value. The difference between theoretical and experimental R_p increased to 45, 55, and 60 % for ion gate widths of 400, 200, and 100 μ s, respectively. This increase in under performance at smaller gates indicated a possible constant error contribution from imperfect gating and will be addressed further in the following sections. The data also revealed that although theoretical R_p for TEA and TBA varied by 10 - 20 ms/ms, depending on the drift voltage, experimental R_p obtained for both TEA and TBA remained almost constant and only varied by 2 - 4 ms/ms. Despite the observed differences in experimental and theoretical R_p , resolving powers as high as 71 ms/ms were observed.

In the next set of experiments all other experimental conditions were kept constant with the exception of the AG distance, which was reduced from 5.0 mm to 0.7 mm with the results shown in Figure 5-2. This distance was reduced in an attempt to improve the R_p of this instrument. The purpose of the anode grid is to prevent the electric field of the arriving ion cloud from inducing a capacitive current flow on the Faraday plate detector prior to ions striking the anode, thus effectively preventing the formation of an image current. These capacitive effects, determined by its distance to the anode grid, have been shown to play a significant role in the measured peak width.¹⁴⁰

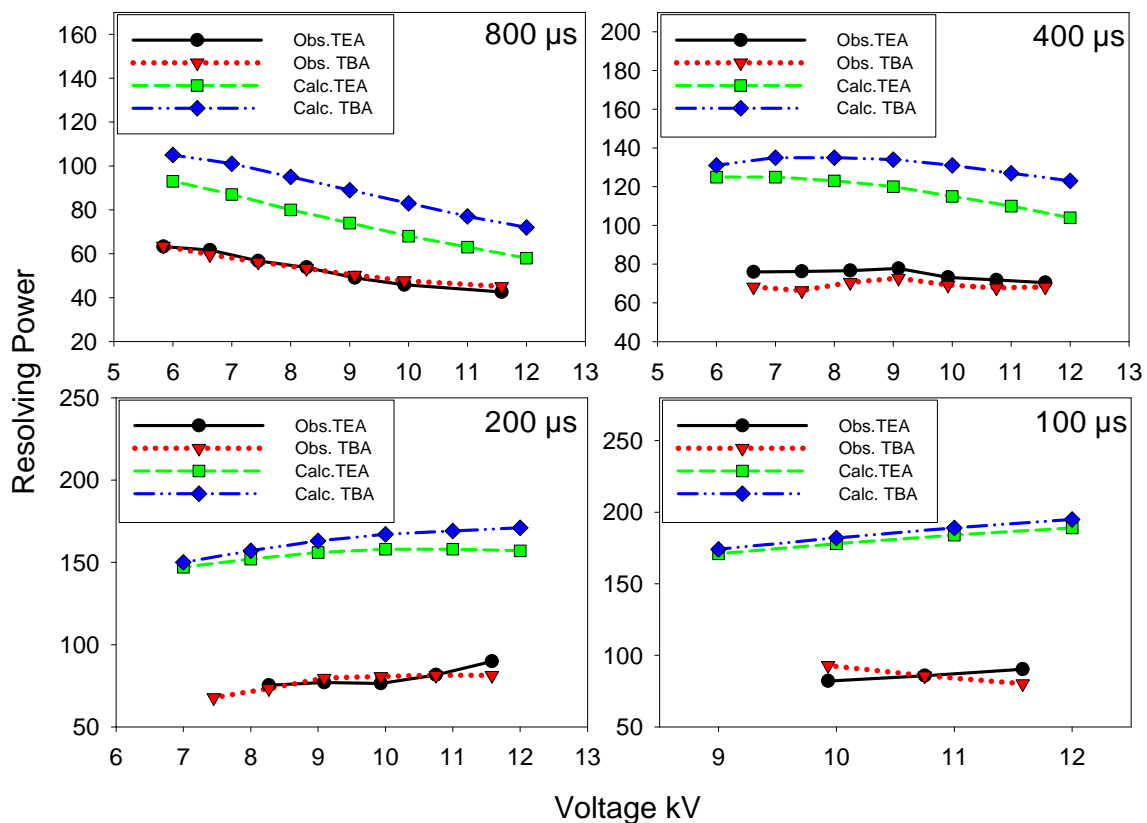


Figure 5-2 Theoretical and experimental resolving power obtained for a 150 μM TBA and TEA solution using 800, 400, 200, and 100 μs ion gate widths and drift voltages in the range 5.84 - 11.58 kV for a 10 mm anode and a 0.7 mm anode grid distance instrumental configuration. The blue and green traces represent the theoretical R_p for TBA and TEA, respectively, while the red and black traces represent experimentally-observed values.

Figure 5-2 shows the results obtained with the 0.7 mm AG distance configuration. Similar trends to those observed with the 5.0 mm AG distance were observed. Each ion gate width had an optimal operational drift voltage where R_p was maximized, with larger ion gate widths (top panels) performing better at lower drift voltages and smaller ion gate widths (bottom panels) performing better at higher drift voltages. However, the difference between theoretical and experimental R_p for TEA were, on average, smaller

(28, 34, 46, and 52 % for ion gate widths of 800, 400, 200, and 100 μs , respectively). The maximum R_p obtained for the 0.7 mm AG distance was 94 ms/ms, using a 100 μs gate width, which compared favorably with the best R_p values obtained for the 5.0 mm AG distance.

Measurements of R_p with a 30 mm anode were also performed with a 5.0 mm and 0.7 mm AG distance, and also with a $1.5 \text{ L}\cdot\text{min}^{-1}$ drift gas flow rate (Figure 5-3 for TEA and Figure 5-4 for TBA). The 10 mm anode diameter data shown in Figures 5-1 and 5-2 is plotted again in these graphs for comparison purposes. It was observed that the larger anode provided a more intense signal due to the larger ion sampling area, allowing the use of smaller ion gate widths, and that for the smaller ion gate widths, the data collected with the 10 mm anode showed a 5 - 10 % higher resolving power due to sampling of only the most homogeneous portion of the ion packet.

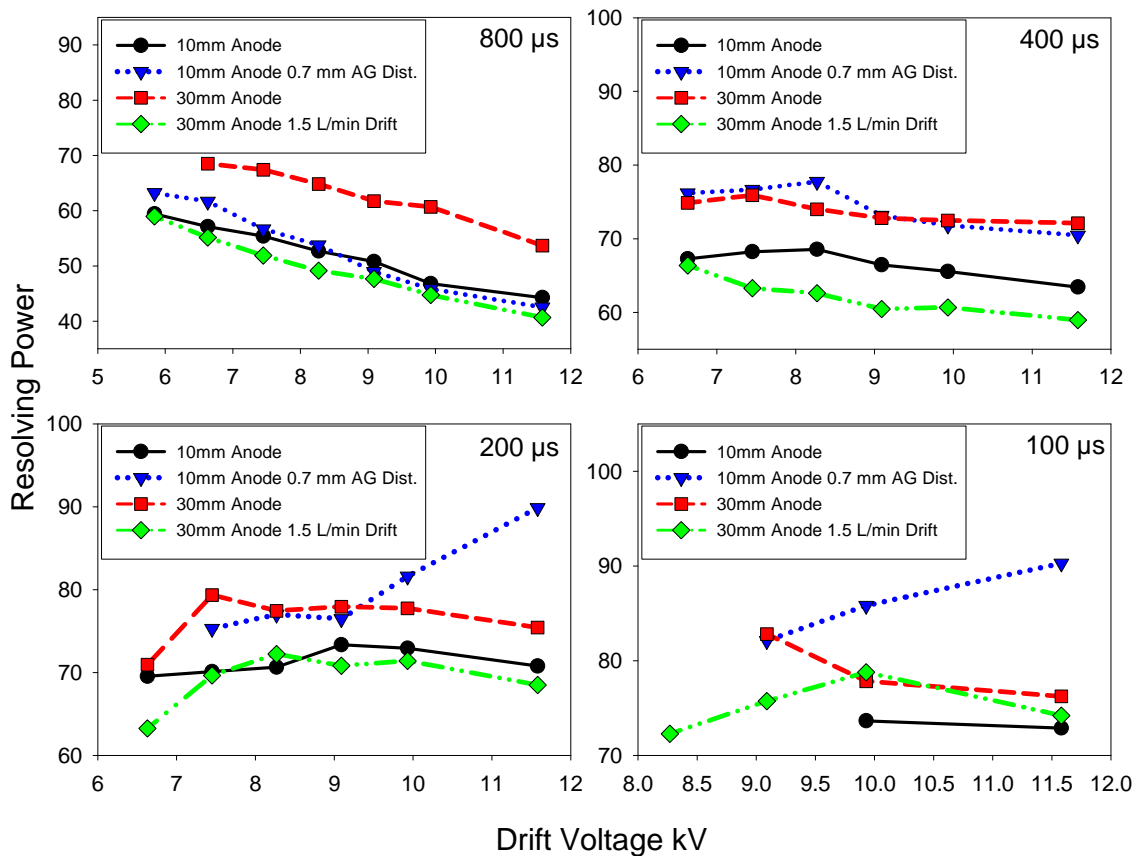


Figure 5-3 Experimental resolving power obtained for TEA using 800, 400, 200, and 100 μs ion gate widths and drift voltages in the range 5.84 - 11.58 kV for the following instrumental parameters: (black) 10 mm anode, 5.0 mm AG distance, 0.2 L·min⁻¹ N₂; (blue) 10 mm anode, 0.7 mm AG distance, 0.2 L·min⁻¹ N₂; (red) 30 mm anode, 5.0 mm AG distance, 0.2 L·min⁻¹ N₂; (green) 30 mm anode, 5.0 mm AG distance, 1.5 L·min⁻¹ N₂.

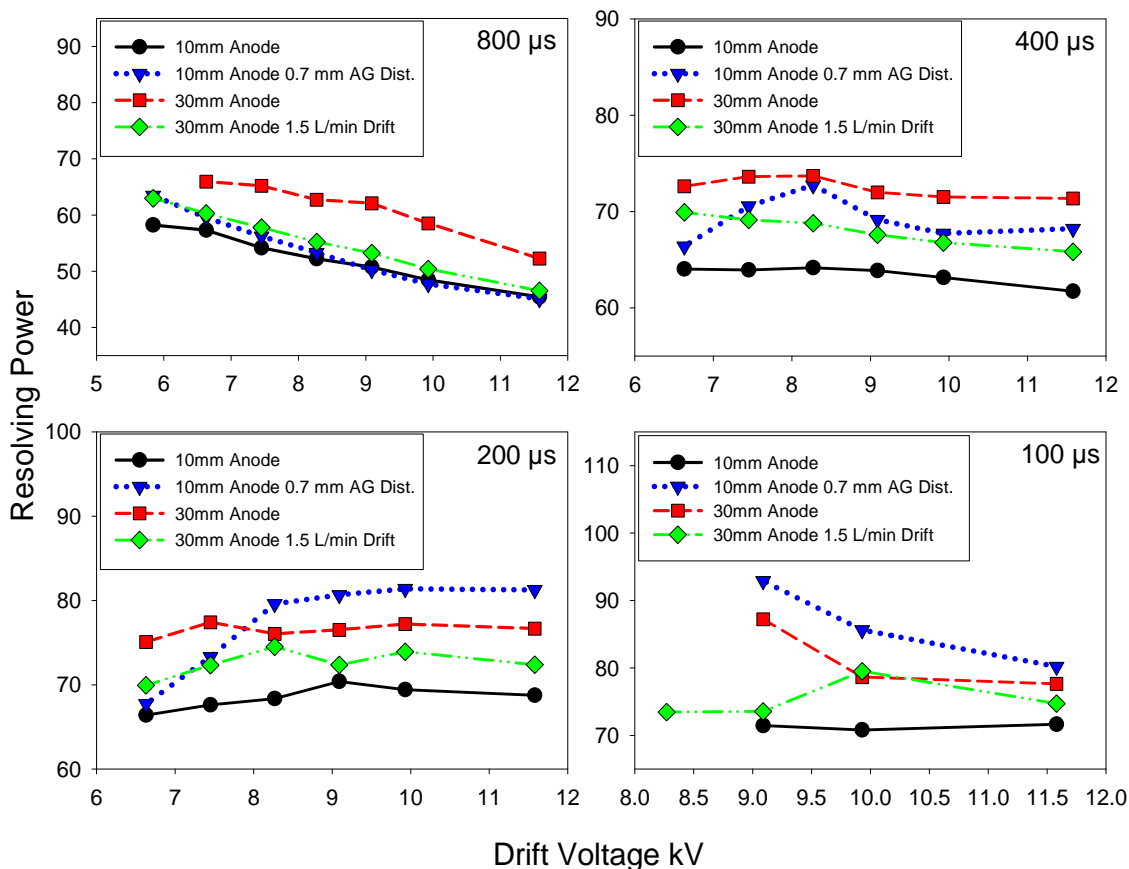


Figure 5-4 Experimental resolving power obtained for TBA using 800, 400, 200, and 100 μs ion gate widths and drift voltages in the range 5.84 - 11.58 kV for the following instrumental parameters: (black) 10 mm anode, 5.0 mm AG distance, $0.2 \text{ L}\cdot\text{min}^{-1} \text{ N}_2$; (blue) 10 mm anode, 0.7 mm AG distance, $0.2 \text{ L}\cdot\text{min}^{-1} \text{ N}_2$; (red) 30 mm anode, 5.0 mm AG distance, $0.2 \text{ L}\cdot\text{min}^{-1} \text{ N}_2$; (green) 30 mm anode, 5.0 mm AG distance, $1.5 \text{ L}\cdot\text{min}^{-1} \text{ N}_2$.

5.4.2. Evaluation of Parameters Affecting Separation Power

Once the performance of the resistive-glass IMS in terms of R_p was investigated, the separation power in terms of chromatographic resolution was evaluated under identical conditions. Equation 5.2 indicates that the diffusional contribution to peak width is expected to decrease as the voltage on the drift tube is increased. At high drift voltages, the ion packet should experience less diffusional broadening and become progressively

more similar in peak width to the initial ion packet. This is advantageous in terms of R_p , but this rapid transit through the drift region also decreases the extent of the interactions with the drift gas, negatively affecting the chemical separation power if two or more different ionic species are contained within the ion packet.

Figure 5-5 shows the chromatographic resolution obtained for a mixture of TBA and TEA using 800, 400, 200, and 100 μs ion gate widths with drift voltages in the range 6.63 - 11.58 kV for a 30 mm anode, 1.5 $\text{L}\cdot\text{min}^{-1}$ N_2 drift gas configuration. For an 800 μs ion gate width, resolution increased with decreasing voltage, with a maximum resolution of 11.1 obtained at a drift voltage of 6.63 kV. This same trend was observed for an ion gate width of 400 μs , with a maximum resolution of 12.4 and 12.5, obtained at a drift voltage of 6.63 and 7.45 kV, respectively. At smaller ion gate widths, an optimum voltage appears around 10 - 11 kV producing a maximum resolution of 13.3 for a 200 μs ion gate width, and 15.2 for the 100 μs ion gate width. Resolution is well suited when evaluating the chromatographic conditions that lead to unit resolution ($R = 1$), baseline-resolved peaks ($R = 1.5$), or the minimum acceptable resolution ($1.75 < R < 2.0$).^{60, 61} Although all investigated gates and voltages provide more than the minimum acceptable resolution, when analyzing a complex mixture, it is preferable to operate with smaller gates and higher drift voltages to maximize the separation capabilities of the instrument. The chromatographic resolution values obtained using a 0.2 $\text{L}\cdot\text{min}^{-1}$ N_2 drift gas flow rate and various anode configurations were lower on average than when 1.5 $\text{L}\cdot\text{min}^{-1}$ flow rates were used to produce the data in Figure 5-5, and showed less marked trends (Figure 5-6).

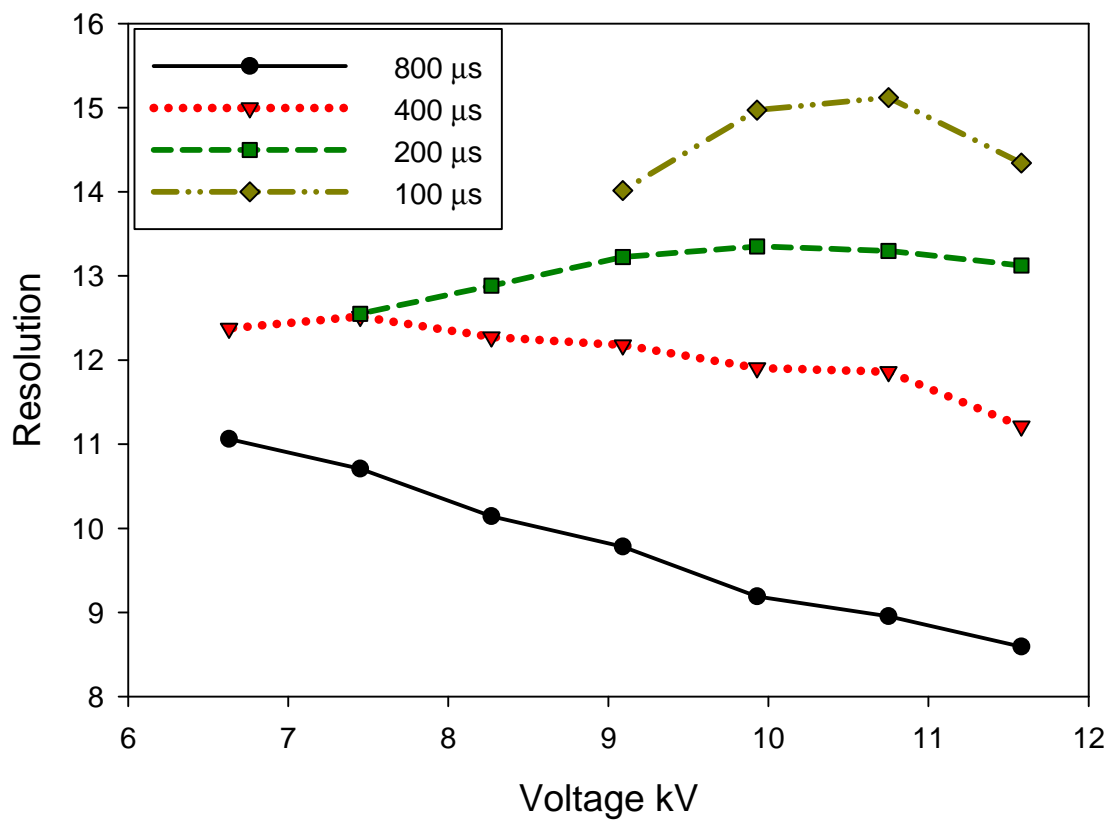


Figure 5-5 Chromatographic resolution obtained for an equimolar mixture of TBA and TEA using 800, 400, 200, and 100 μs ion gate widths and drift voltages in the range 6.63 - 11.58 kV for a 30 mm anode configuration employing a drift gas flow rate of 1.5 L·min⁻¹ N₂.

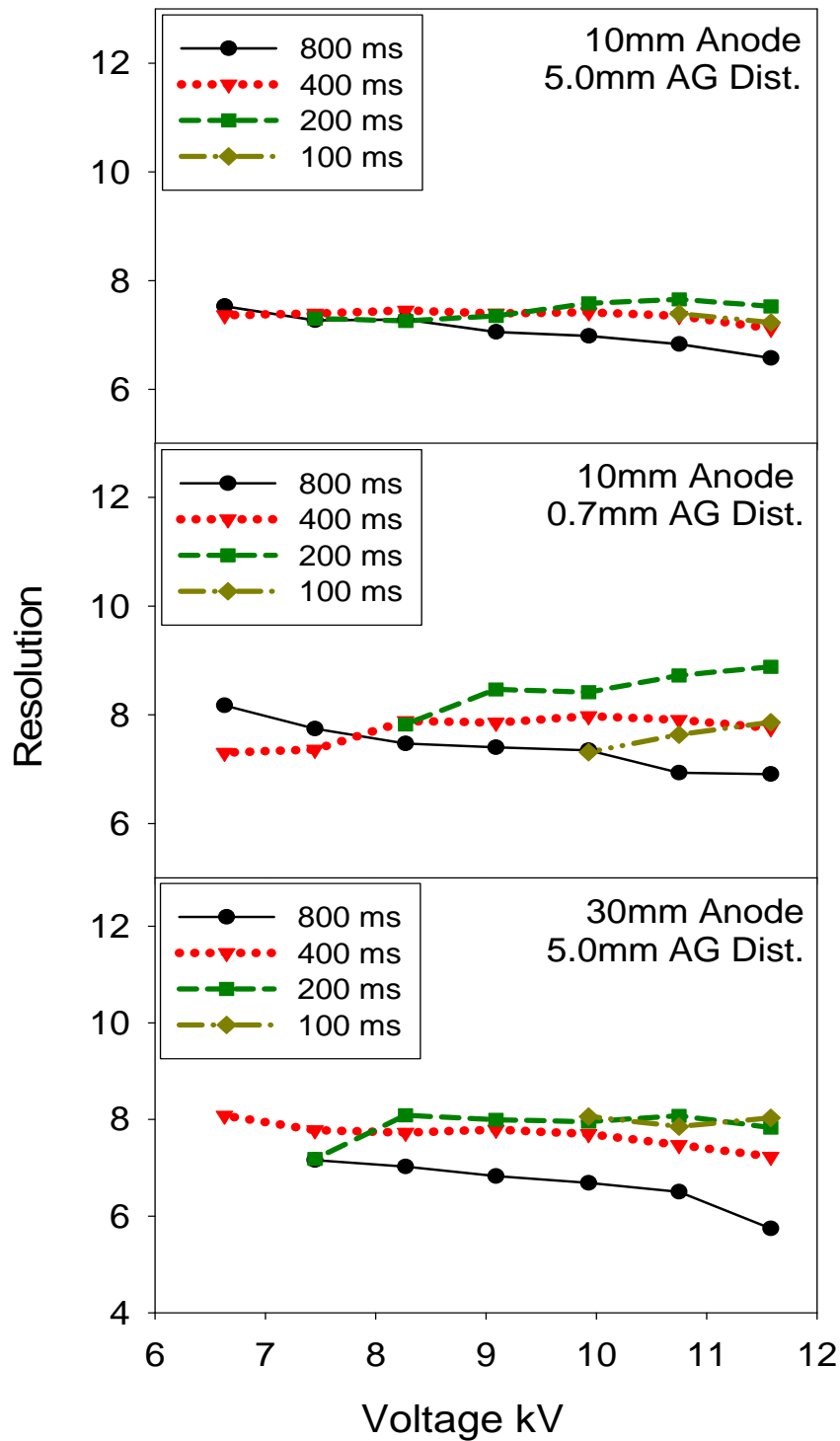


Figure 5-6 Chromatographic resolution obtained for an equimolar mixture of TBA and TEA using a drift gas flow rate of $0.2 \text{ L}\cdot\text{min}^{-1} \text{ N}_2$, 800, 400, 200, and 100 μs ion gate widths and drift voltages in the range 6.63 - 11.58 kV for a 10 mm anode, 5.0 mm AG distance (top panel); 10 mm anode, 0.7 mm AG distance (center panel), and a 30 mm anode, 5.0 mm AG distance configuration (bottom panel).

Of the different configurations investigated thus far, the 30 mm anode configuration using a drift gas flow rate of $1.5 \text{ L}\cdot\text{min}^{-1} \text{ N}_2$ produced the largest resolution, especially at smaller ion gates, and highest sensitivities. This configuration, however, produced relatively lower R_p values in almost all scenarios (Figs. 5-3 and 5-4). In practical terms, however it is preferable to operate in conditions that maximize resolution of pairs of chemically related species. As such, R_p only provides a simple assessment of the peak capacity of the system based on peak width measurements for a single compound.

5.4.3. Theoretical Evaluation of Factors Affecting Instrumental Performance

To investigate the contributions to the experimental pulse width from factors such as field inhomogeneity and non-ideal gate performance in our resistive-glass IM spectrometer, we applied Equation 5.3 to our voltage-dependent experimental data. First, we investigated the diffusional contribution to the final experimental pulse width observed at the detector, represented by the “ α ” parameter. This parameter also models other effects that could lead to peak broadening when a fraction of the ions spend more time in the drift tube than expected. An example of this type of would be that caused by field inhomogeneity within the drift tube, which results in a distortion of the ion packet. Another possibility would be interaction of the edges of the ion packet with internal components of the IMS such as the ion gate mask. These types of interactions would not have a constant voltage dependence and would also affect α .

Figure 5-7 (top panel for TEA and bottom panel for TBA) shows plots of squared experimental peak width (w^2) as a function of the diffusion-dependent parameter (Tt_d/V) collected with a 30 mm anode, $1.5\text{L}\cdot\text{min}^{-1}$ N_2 drift gas configuration. The color-coded lines represent the least-squares fit of the experimental data for ion gate widths of 800, 400, 200 and 100 μs . The slope for each individual gate width gives an estimate of α , shown as the slope of the linear equation fitting each data subset. At each gate width, obtained α values for both TEA and TBA were very similar, as expected. However, all experimental α values were larger than the expected “ideal” value of 0.9×10^{-3} predicted by Equation 5.3 indicating that uncontrolled “diffusion-like” effects made peaks wider than expected from theory. One hypothesis to explain these results would be that the electric field within the resistive-glass is less homogeneous than initially thought. Batch-to-batch performance comparisons and long-term mechanical stress and temperature stability investigations of the resistive-glass material used in this spectrometer should shed more light into this matter. These investigations may be complicated by the fact that electric field inhomogeneity in resistive-glass tubes would not take a periodical function form, as in stacked ring electrode spectrometers, but a much more complex three-dimensional shape.

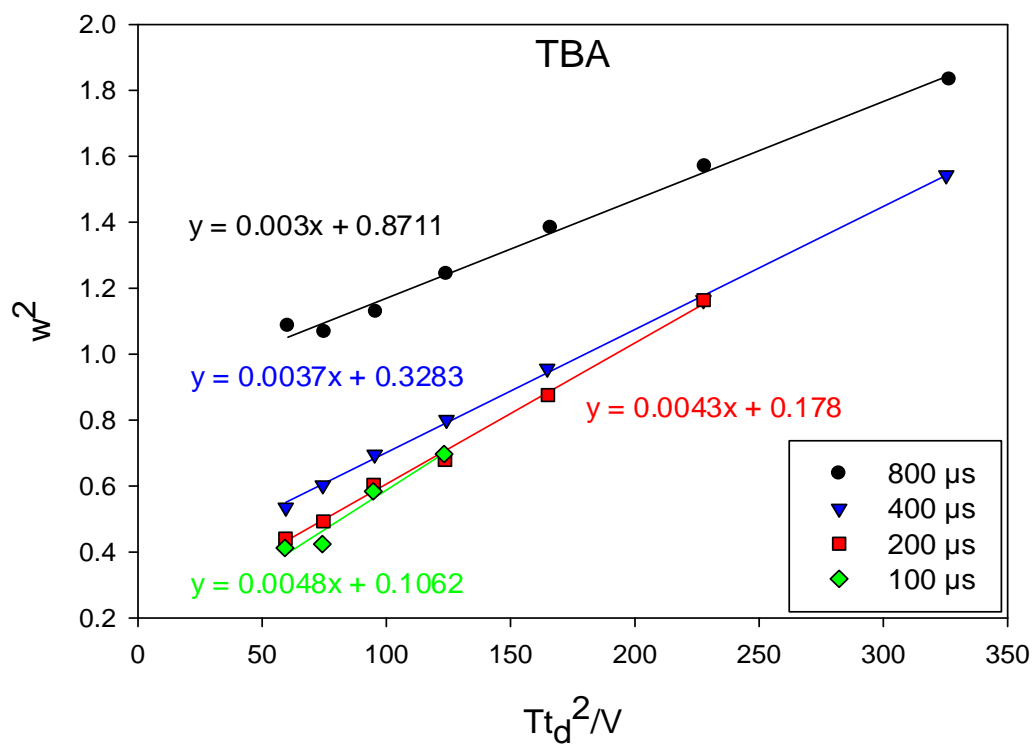
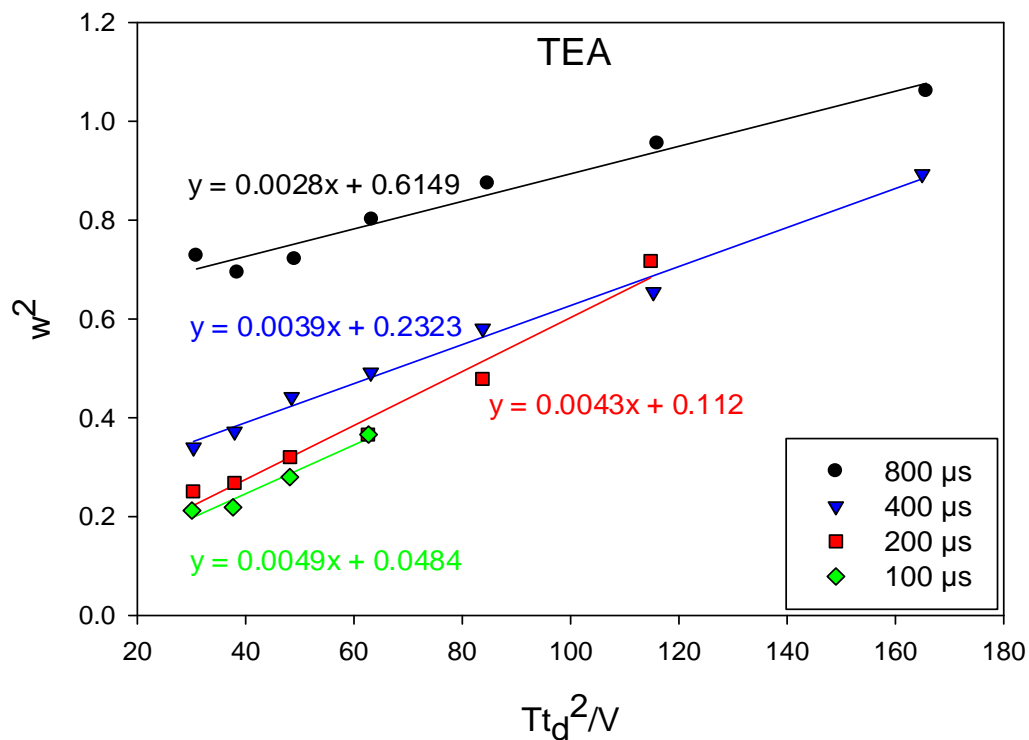


Figure 5-7 Measured peak width squared as a function of the diffusion-dependent parameter for ion gate widths of 800, 400, 200, and 100 μs . The top panel shows results for TEA and the bottom panel shows results obtained for TBA. Alpha values are obtained from the slope of each trend line.

The data shown in Figure 5-7 also displayed an unexpected dependence on initial ion gate width, with smaller ion gates having progressively larger α values of 3.9×10^{-3} , 4.3×10^{-3} , and 4.9×10^{-3} V/K for gates of 400, 200 and 100 μ s, respectively. We suggest that this dependence on initial ion gate width is caused by the non-ideal performance of the gating pulse shape during the opening and closing of the gate, also referred to as the leading and trailing edges of the pulse. These opening and closing events not only caused a deflection of the ion cloud away from the center of the drift space and out toward the periphery of the drift tube, but also altered the momentum of the ions at the leading and trailing edges of the ion packet causing multiple “diffusion like” effects. Work by Puton et al.^{72, 73} showed that as the voltage on a BNG was rapidly increasing or decreasing, the electric field lines slowly shifted from perfectly parallel “gate open” through an almost 45 degree angle, until the field lines joined the respective positive and negative wire sets of their successive electrodes, resulting in a “closed gate.” Ions encountering these 45 degree angle field lines would be forced into a different path than the rest of the ion packet. This distortion of the injected ion packet at the leading and trailing edges would add an α contribution to each individual gating event. When employing smaller ion gate pulse widths for ion injection, these leading and trailing edge distortions are relatively more significant, becoming a greater percent of the total ion gate width and resulting in a more distorted ion packet. Non-ideal BNG behavior is a well-known phenomenon and has been studied experimentally^{102, 199, 201} and via simulations.^{71, 203} A summary of α values for all other experimental conditions tested is presented in Table 5-1 together with the corresponding 95 % confidence intervals obtained from the least squares trend lines. Although α values were different for different experimental setups, A similar gate

dependence on initial ion gate width was observed for all investigated configurations, reinforcing the idea of a gating contribution to diffusion-like peak broadening.

Table 5-1 Summary of α values for all experimental conditions and ion gate widths reported with a 95 % confidence interval (confidence intervals not calculated for data sets with ≤ 4 points). Alpha values reported as $\times 10^2$ (V/K).

TEA

Starting Condition	800μs Gate	400μs Gate	200μs Gate	100μs Gate
30 mm Anode	0.285 \pm 0.024	0.328 \pm 0.030	0.451 \pm 0.110	0.201
30 mm Anode 1.5 L\cdotmin⁻¹	0.279 \pm 0.058	0.395 \pm 0.046	0.546 \pm 0.128	0.495
10 mm Anode	0.381 \pm 0.027	0.418 \pm 0.015	0.439 \pm 0.039	0.410
10mm Anode 0.7 mm AG	0.272 \pm 0.033	0.309 \pm 0.020	0.476 \pm 0.133	0.519

TBA

Starting Condition	800μs Gate	400μs Gate	200μs Gate	100μs Gate
30 mm Anode	0.316 \pm 0.031	0.345 \pm 0.018	0.359 \pm 0.029	0.101
30 mm Anode 1.5 L\cdotmin⁻¹	0.298 \pm 0.029	0.373 \pm 0.014	0.428 \pm 0.038	0.482
10 mm Anode	0.408 \pm 0.035	0.427 \pm 0.041	0.483 \pm 0.024	0.487
10mm Anode 0.7 mm AG	0.287 \pm 0.041	0.418 \pm 0.059	0.553 \pm 0.078	0.065

In order to better understand the contribution to peak width caused by any non-ideal performance of the ion gate, the experimentally-observed β parameters in Equation 5.3 were investigated. As mentioned earlier, β represents the contribution from the initial ion gate width to the final peak width measured at the detector and includes factors that would cause changes in the behavior of the ion packet dependent on the amount of ions injected. For example, β values greater than 1 would point at Coulombic repulsion or other electrostatic interactions caused by increased charge density in the

injected ion packet when using wider ion gate pulses. Beta would have a theoretical value of 1 only if the size of the final measured ion packet was equal in width to the initial ion packet.

Figure 5-8 (top TEA, bottom TBA) shows a plot of experimental squared peak width (w^2) as a function of the nominal squared ion gate width (t_g^2) collected with a 10 mm anode configuration. The color coded trend lines represent the least-squares fit of the experimental data for ion gate widths of 800, 400, 200 and 100 μs , the slope for each individual gate being an estimation of β in each case. All observed β values were lower than unity, but behaved more ideally for TBA than for TEA. The smaller than expected values of β obtained with our resistive-glass IMS indicate that the peak width measured at the detector is narrower than the width of the initially injected ion packet. Previous work by Siems et al.⁶³ and Spangler and Collins¹⁴⁰ showed an opposite effect, with β values of 1.13 - 1.24 and 1.15, respectively. In addition to these general trends, β values for both TEA and TBA showed an unexpected dependence with drift voltage. The largest value of $\beta = 0.547$ for TEA was observed at a drift voltage of 11.6 kV with progressively smaller values occurring at lower voltages. For TBA, the largest value of $\beta = 0.929$ was obtained at a drift voltage of 11.6 kV, with the smallest value of $\beta = 0.729$ obtained at a drift voltage of 8.3 kV.

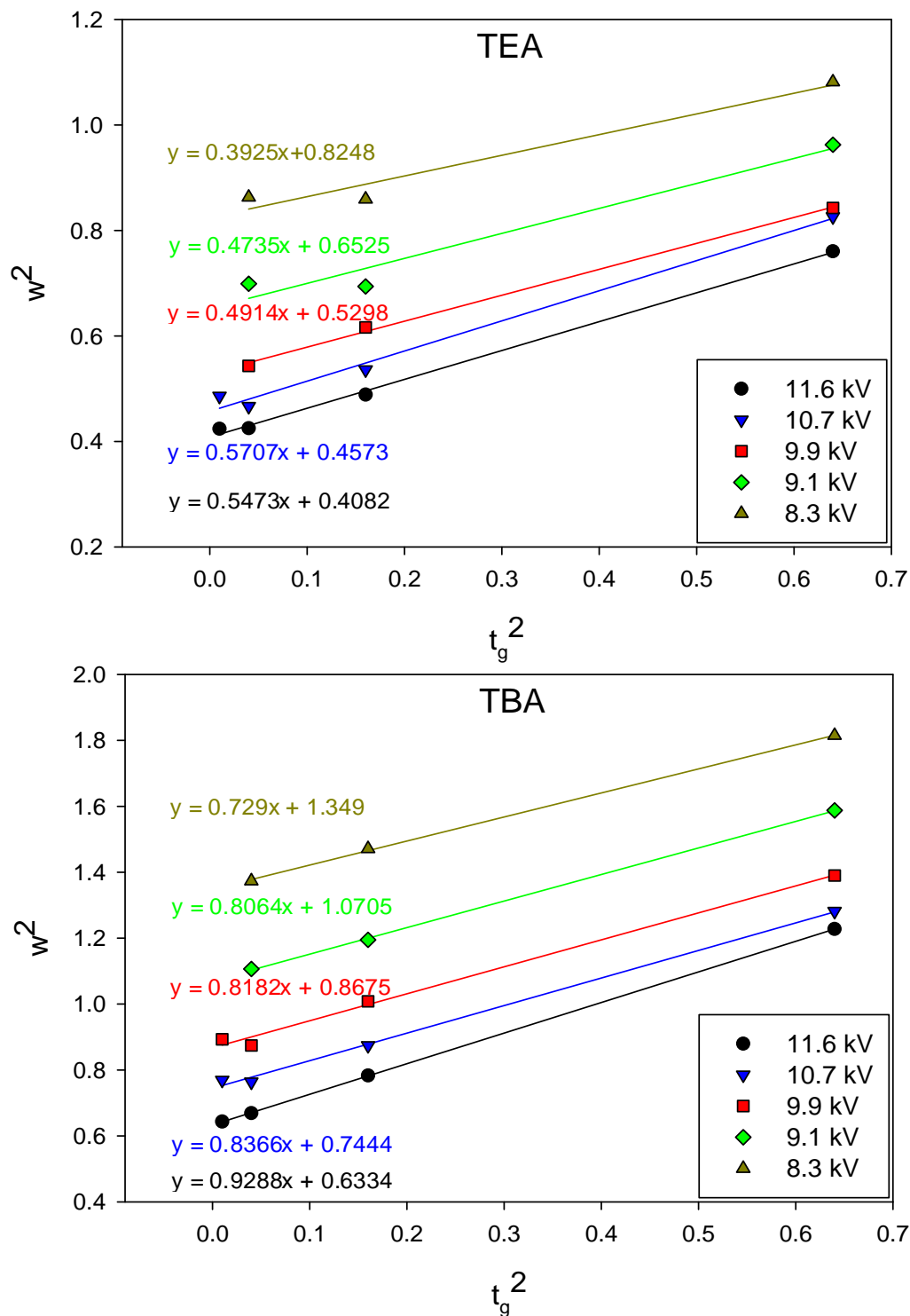


Figure 5-8 Measured peak width squared as a function of the ion gate width at voltages of 11.6, 10.7, 9.9, 9.1, and 8.3 kV. The top panel shows results obtained for TEA and the bottom panel shows results obtained for TBA. Beta values are obtained from the slope of each trend line.

In our setup, the ion gate is closed by applying ± 35 V to the adjacent ion gate wire sets floating at the drift tube entrance voltage. During the time period when the ion gate is closed, depletion of the incoming ion cloud in the area immediately behind the gate occurs. When employing smaller ion gate pulse widths, this ion-depleted area in space becomes relatively more significant because the proportion of depleted ions becomes a greater percent of the total amount of ions to be injected, reducing β . Because the voltage drop in the desolvation chamber preceding the ion gate increases when drift voltage is increased, it is expected that the depletion region will be replenished faster at higher drift voltage settings, explaining the trend towards higher β values. We also hypothesize that the observed differences between ions with different m/z is related to the voltage used to close the ion gate. It appears as if the ± 35 V applied to the BNG are insufficient to deflect all ionic species in the incoming ion beam correctly. This would explain why the β value from the smaller, faster-moving TEA species is approximately half of the β value associated with the larger and slower moving TBA, which behaves almost ideally at higher drift voltages. Limitations in the ion gate pulsing electronics prevented us from applying higher gating voltages to further test this hypothesis.

5.5. Conclusions

Our studies have shown that the optimum resolving power in the prototype resistive-glass in mobility instrument discussed here is dependent on voltage and initial ion gate pulse width, with values that are lower than that predicted by theory by 25 - 48 %, and larger deviations occurring at smaller ion gate widths. The performance of the resistive-glass spectrometer was found to be comparable to other standalone stacked

ring spectrometers reported in the literature, which typically produce resolving powers approximately 26 - 46 % lower than that predicted by theory.²⁰⁴ The anode grid to anode distance has a major effect on resolving power, as decreasing this distance from 5.0 to 0.7 mm produced an average increase in resolving power of 20 ms/ms, with larger gains at smaller ion gate pulse widths, due to the decoupling of the image current from ion detection.

The separation power in terms of chromatographic resolution showed that a high drift gas flow rate was the most important factor benefitting separation. Our results also showed that at large initial ion gate pulse widths, better separations could be obtained at lower drift voltage. However, as the size of the ion gate pulse decreased to values $\leq 200 \mu\text{s}$, a voltage-dependent optimum appears at a drift voltage between 10 and 11 kV. Through an analysis of both the initial ion gate pulse width dependence of the α value, and the smaller than expected β values obtained with our instrument, we have discovered imperfections in the behavior of our current ion gating system which will be addressed in future instrument versions.

CHAPTER 6. CONCLUSIONS AND OUTLOOK

6.1. Abstract

This chapter presents a summary of the results of my characterization and investigations with the prototype high-resolution resistive-glass atmospheric pressure drift tube ion mobility spectrometer. This chapter concludes with a discussion of potential future directions to further expand this work.

6.2. Accomplishments in the Development and Characterization of a Monolithic DTIMS

Ion mobility spectrometry is a rapid gas-phase separation technique that has been around for over 40 years however, it has only come of age as an analytical method during the past decade. With well over 50,000 stand-alone ion mobility spectrometers currently employed throughout the world⁵⁸ for the detection of explosives,^{1, 2} drugs,¹⁹ and chemical-warfare agents.^{17, 18} The coupling of IMS to MS (IM-MS)^{23, 205, 206} has enabled the performance of time-nested multidimensional separations with high sample throughput and enhanced peak capacity²⁰⁷⁻²⁰⁹ and has transformed IM-MS applications and instrumental designs to one of the most rapidly growing areas of mass spectrometry.⁵⁸ The results presented here demonstrate the potential and advantages of using resistive glass as an alternative construction material to the typically design consisting of a stack of ring electrodes, with each pair separated by insulating spacers and connected to a resistor network. These stacked-ring mobility cells are known to suffer from electric field inhomogeneities that limit the resolving power of the instrument.

Resistive-glass was chosen as an alternative construction material in an attempt to minimize radial electrical field variations within the ion mobility drift tube and improve the resolving power of the instrument. The design and construction of both the hardware and software for the prototype high-resolution resistive-glass atmospheric pressure drift tube ion mobility spectrometer with interchangeable corona discharge and nanoelectrospray ion sources was extensively described. This included a description of the timing scheme for synchronizing ion gating and data acquisition when operating in both standalone mode and when coupled to a TOF-MS as well as a detailed description of the design and operation of the software used to control operation of the DTIMS and all related data acquisition and processing software. For the coupling of the DTIMS to our TOF-MS, preliminary IM-MS data was presented along with an analysis of the packet spreading observed in the current configuration and initial attempts to correct this problem. Possible solutions for eliminating this packet spreading for successful operation in IM-MS mode will be presented in the following section.

Initial operation and characterization of the effects of instrumental parameters such as temperature, drift gas flow rate, and anode-to-anode grid distance were investigated to study and optimize the operating conditions of our prototype monolithic DTIMS. These preliminary studies allowed for an optimization of the instrument and demonstrated an average resolving power of 68 ms/ms, which was comparable, or better, than other standalone stacked-ring type atmospheric pressure DTIMS reported in the literature. The radial distribution of ion density in the drift region of the spectrometer was extensively characterized and revealed that greater than 98 % of the ions reached the

detector indicating almost no ions were lost by collision with the drift tube walls and demonstrated optimum ion densities for coupling to the DTIMS to a mass spectrometer.

Once the affects of instrumental conditions were understood and optimized, the potential for the DTIMS for the analysis of environmental samples was demonstrated by the analysis and successful separation of marine siderophores in both the iron-bound and free ligand states. Although the instrument was successfully able to separate a solution of marine siderophores, these preliminary studies also revealed that our DTIMS was insufficiently sensitive for the trace analysis of these siderophores in seawater samples. To overcome this lack of sensitivity we developed a novel multiplexing method that we named “digital multiplexing”

All DTIMS suffer from an intrinsically low duty cycle ($\sim 0.04 - 1\%$) caused by the rapid pulsing of the ion gate (25 - 400 μs) followed by a comparatively long drift time (25 - 100 ms), which translates into a loss of sensitivity. In order to increase the sensitivity we developed and implemented an extended multiplexing approach that encompasses arbitrary binary ion injection waveforms with variable duty cycles ranging from 0.5 to 50 %. With these waveforms, the performance of the instrument in terms of signal-to-noise gains, was improved between 2 - 7-fold. In terms of the marine siderophores, concentration detection limits were improved from 100 μM DFOB, when operated in conventional signal-averaging mode to 2 μM DFOB, when operating in digital multiplexing mode. An additional advantage of the digital multiplexing over other traditional multiplexing methods was that it does not suffer from false spectral echoes which can be easily confused for a real chemical species when unknown samples are analyzed.

Although the sensitivity of the instrument had been greatly improved and preliminary studies demonstrated the potential of resistive glass as an alternative building material for DTIMS, there were still many unanswered questions regarding this prototype. Information about the homogeneity of the electric fields generated by the resistive glass, the performance of the Bradbury-Nielsen ion gate and respective pulsing electronics were investigated in-depth to further understand and improve the prototype DTIMS. The affects of previously uninvestigated instrumental parameters on the performance and separation power of our prototype resistive-glass DTIMS were also examined. These new optimization studies helped to improve the resolving power of our DTIMS from the previously observed maximum of 68 ms/ms, up to a new maximum of 94 ms/ms. The theoretical analysis of the data from these optimization studies also revealed imperfections in the behavior of our current ion gating system which will be addressed in future instrument versions to further improve the performance of our DTIMS.

6.3. Proposed Future Directions

6.3.1. DTIMS-MS

Considerably more work needs to be done in order to overcome the observed limitations when operating in IM-MS mode. Our initial coupling of our DTIMS to our JEOL TOF mass spectrometer revealed that collisional cooling within ion guide was causing packet spreading and resulting in a loss of the information obtained in IMS dimension. These initial studies also revealed a lack of sensitivity when operated in IM-MS mode, presumably due to a combination of the low duty cycle of the DTIMS and

the sampling of only a small portion of the ion cloud. The following studies are recommended for future research:

1. Collisional cooling within an ion guide occurs because an ion beam loses energy from collisions with neutral gas molecules present in the ion guide. The degree of collisional cooling can therefore be reduced by either reducing the amount of neutral gas molecules present in the ion guide, or by reducing the amount of time the ions spend within the ion guide. To this end, installing a segmented ion guide to allow for application of stronger axial electric fields via variable-voltage potentials on the different segments of the ion guide to reduce the residence time of the ions further and “shotgun” them through the ion guide should mitigate the problem of packet spreading. Additionally the pressure in the first and second regions of the ion guide could be reduced by modifying the vacuum system. Initial results have shown that reducing the pressure in the first region reduced collisional cooling and resulted in reduction in the peak spreading in the mobility dimension. Further reducing the pressure in the first region of the ion guide with a stronger pump and modifying the vacuum system to allow access to the second region of the ion guide would be a complementary solution to the segmented ion guide.
2. As mention previously sensitivity in DTIMS is limited by the low duty cycle in conventional signal averaging mode. This lack of sensitivity is further compounded when an atmospheric pressure DTIMS, is coupled to a mass spectrometer. Of the 0.04 - 1.0 % of the initial ions that are injected into the mobility cell, > 99% of them are lost before they are detected by the mass

analyzer.^{41, 97} This lack of sensitivity could be approached from a two pronged solution.

- a. The digital multiplexing method that was developed for standalone DTIMS could be applied to IM-MS. This would involve modification of the triggering and data acquisition system for successfully deconvolution the multiplexed data. To further increase the sensitivity and duty cycle of the IM-MS analysis, the TOF mass spectrometer could be multiplexed. This would involve a sufficiently more complex instrumental modification including replacing the original TOF pulser with a faster high-voltage pulser capable of high-frequency operation, and a redesign of the timing and triggering schemes. Once instrumental modifications are completed, both the DTIMS and the MS can be simultaneously multiplexing by modulating both ion injection events. This would theoretically develop what could be described as an “imaging” IMS-TOF with full encoding of the signal. The use of the term “imaging” derives from the nomenclature by Harwit and Sloane¹⁴⁴ used in optical spectroscopies, and should not be confused with imaging mass spectrometric techniques used for collecting mass spectra in an x-y plane and assembling those into a molecular image.
- b. An alternative approach would be to take a look at the inlet aperture of the first orifice in the mass spectrometer. This 0.4 mm sampling orifice aperture is only sampling a very small percentage of the approximately 25 mm ion cloud exiting the DTIMS. A Glass Capillary Array could be used to replace this limiting sampling orifice. Glass Capillary Arrays

consist of millions of precision glass capillary tubes fused together to produce a uniform and mechanically rigid structure. These arrays have been successfully utilized as inlets for sector mass spectrometers.²¹⁰ Glass Capillary Arrays are superior to single apertures owing to their jet disruption capabilities and should dramatically increase the amount of ions transferred from the DTIMS to the mass spectrometer without increasing the load on the vacuum system.

6.3.2. DTIMS Instrumental Modifications

The monolithic resistive glass drift region was shown by the theoretical modeling performed in chapter 5 to produce less homogeneous electric fields than previously though. A more detailed analysis of the electric fields generated by the resistive-glass would lead to better understanding of factors effecting resolving power and how to mitigate them.

1. Recent communication with the manufacturer of the resistive glass, it was revealed that their “might have been some technical difficulties during the manufacturing of the 1st generation resistive glass tubes.” By replacing the existing drift tube with a new 2nd generation resistive glass tube, the homogeneity of the original tube could be evaluate and compared to this new batch. Even if there were no problems with the 1st generation tubes, the resistive properties of the material might have changed with time, due to repeated use and mechanical stress. These effects could be evaluated with a new set resistive glass tubes and a thorough study of how instrumental

conditions such as temperature and accumulation of contaminants affect the properties of the material.

2. The theoretical studies performed in chapter 5 revealed that our current ion gating system performs non-ideally. Defects in the shape of the ion gate not only reduce the resolving power of the instrument but also lead to the generation of spectral echoes when operating the instrument in multiplexed mode. It is recommended that the pulsing electronics be re-designed to allow for the application for gate operating voltages of up to ± 50 V, which should be sufficient for deflection of ions over a wide range of sizes. In addition, the wires of the current interleaved ion gate could be replaced with thinner and more closely spaced wires. Although this would reduce the mechanical stability of the gate, it would also reduce the defects associated with the rising and falling edges of the ion gate pulse that lead to distorted leading and tailing edges of the injected ion packets.

6.3.3. Multiplexed DTIMS Work

1. Studies of the arbitrary multiplexing sequences revealed that the position of the open “1” and closed “0” elements in the sequence played a vital role in the performance of the sequence however, insufficient data was available to identify which characteristics of a sequence produced favorable results. I propose a thorough evaluation of the effects of different sequence constructions such as; spacing between open events, frequency of adjacent open events, randomness of

gating events, and different types of mathematically based sequence constructions.

2. Recent work by Tabrizchi et al.²¹¹ described a new method called “Inverse Ion Mobility Spectrometry” where the ion gate is always open and dip is created in the ion beam by rapidly closing the ion gate through the application of an inverse pulse. This technique has been shown to produce resolving powers 30 - 60 % higher than operation in conventional mode. I propose that this inverse pulsing technique be applied to our digital multiplexing method. This would not only increase the resolving power obtained with the method but should also mitigate, or fully eliminate, any contributions from imperfect modulation of the ion beam, resulting in a deconvoluted spectrum without spectral echoes.

REFERENCES

- (1) Ewing, R. G.; Atkinson, D. A.; Eiceman, G. A.; Ewing, G. J. (2001). "A Critical Review of Ion Mobility Spectrometry for the Detection of Explosives and Explosive Related Compounds", *Talanta*, 54(3), pp. 515-529.
- (2) Wu, C.; Steiner, W. E.; Tornatore, P. S.; Matz, L. M.; Siems, W. F.; Atkinson, D. A.; Hill, H. H. (2002). "Construction and Characterization of a High-Flow, High-Resolution Ion Mobility Spectrometer for Detection of Explosives after Personnel Portal Sampling", *Talanta*, 57(1), pp. 123-134.
- (3) Cohen, M. J.; Karasek, F. W. (1970). "Plasma Chromatography - a New Dimension for Gas Chromatography and Mass Spectrometry", *Journal of Chromatographic Science*, 8(6), pp. 330-337.
- (4) Eiceman, G. A.; Karpas, Z. *Ion Mobility Spectrometry, 2nd ed.*; CRC Press: Boca Raton, 2005.
- (5) McAfee, K. B.; Edelson, D. (1963). "Identification and Mobility of Ions in a Townsend Discharge by Time-Resolved Mass Spectrometry", *Proceedings of the Physical Society of London*, 81(520), pp. 382-&.
- (6) McAfee, K. B.; Sipler, D.; Edelson, D. (1967). "Mobilities and Reactions of Ions in Argon", *Physical Review*, 160(1), pp. 130-&.
- (7) Edelson, D.; Morrison, J. A.; McKnight, L. G.; Sipler, D. P. (1967). "Interpretation of Ion-Mobility Experiments in Reacting Systems", *Physical Review*, 164(1), pp. 71-&.
- (8) Guharay, S. K.; Dwivedi, P.; Hill, H. H. (2008). "Ion Mobility Spectrometry: Ion Source Development and Applications in Physical and Biological Sciences", *Ieee Transactions on Plasma Science*, 36(4), pp. 1458-1470.
- (9) Cram, S. P.; Chesler, S. N. (1973). "Coupling of High-Speed Plasma Chromatography with Gas-Chromatography", *Journal of Chromatographic Science*, 11(8), pp. 391-401.
- (10) Karasek, F. W. (1971). "Plasma Chromatography of Polychlorinated Biphenyls", *Analytical Chemistry*, 43(14), pp. 1981-&.
- (11) Karasek, F. W.; Cohen, M. J. (1971). "Molecular Weight Determination by Plasma Chromatography", *Abstracts of Papers of the American Chemical Society*, (Nsep), pp. 43-&.

- (12) Carroll, D. I. L., (FL), Cohen, Martin J. (West Palm Beach, FL), Wernlund, Roger F. (Lake Worth, FL) *Apparatus and Methods for Separating, Detecting, and Measuring Trace Gases with Enhanced Resolution*,
- (13) Revercomb, H. E.; Mason, E. A. (1975). "Theory of Plasma Chromatography Gaseous Electrophoresis - Review", *Analytical Chemistry*, 47(7), pp. 970-983.
- (14) Baumbach, J. I.; Eiceman, G. A. (1999). "Ion Mobility Spectrometry: Arriving on Site and Moving Beyond a Low Profile", *Applied Spectroscopy*, 53(9), pp. 338a-355a.
- (15) Borsdorf, H.; Eiceman, G. A. (2006). "Ion Mobility Spectrometry: Principles and Applications", *Applied Spectroscopy Reviews*, 41(4), pp. 323-375.
- (16) Jones, D.; Brenton, A. G.; Games, D. E.; Brittain, A. H.; Taylor, S.; Kennedy, D.; Smith, P. (1993). "Ion Mobility Spectrometry as a Detection Technique for the Separation Sciences", *Rapid Communications in Mass Spectrometry*, 7(6), pp. 561-566.
- (17) Steiner, W. E.; Clowers, B. H.; Matz, L. M.; Siems, W. F.; Hill, H. H. (2002). "Rapid Screening of Aqueous Chemical Warfare Agent Degradation Products: Ambient Pressure Ion Mobility Mass Spectrometry", *Analytical Chemistry*, 74(17), pp. 4343-4352.
- (18) Steiner, W. E.; Harden, C. S.; Hong, F.; Klopsch, S. J.; Hill, H. H.; McHugh, V. M. (2006). "Detection of Aqueous Phase Chemical Warfare Agent Degradation Products by Negative Mode Ion Mobility Time-of-Flight Mass Spectrometry [Im(Tof)Ms]", *Journal of the American Society for Mass Spectrometry*, 17(2), pp. 241-245.
- (19) Lawrence, A. H.; Elias, L. (1985). "Application of Air Sampling and Ion-Mobility Spectrometry to Narcotics Detection - a Feasibility Study", *Bulletin on Narcotics*, 37(1), pp. 3-16.
- (20) Kanu, A. B.; Hill, H. H.; Gribb, M. M.; Walters, R. N. (2007). "A Small Subsurface Ion Mobility Spectrometer Sensor for Detecting Environmental Soil-Gas Contaminants", *Journal of Environmental Monitoring*, 9(1), pp. 51-60.
- (21) Shumate, C. B.; Hill, H. H. (1989). "Coronaspray Nebulization and Ionization of Liquid Samples for Ion Mobility Spectrometry", *Analytical Chemistry*, 61(6), pp. 601-606.
- (22) Wittmer, D.; Luckenbill, B. K.; Hill, H. H.; Chen, Y. H. (1994). "Electrospray-Ionization Ion Mobility Spectrometry", *Analytical Chemistry*, 66(14), pp. 2348-2355.
- (23) Gillig, K. J.; Ruotolo, B.; Stone, E. G.; Russell, D. H.; Fuhrer, K.; Gonin, M.; Schultz, A. J. (2000). "Coupling High-Pressure Maldi with Ion

- Mobility/Orthogonal Time-of Flight Mass Spectrometry", *Analytical Chemistry*, 72(17), pp. 3965-3971.
- (24) Chapman, S. (1937). "Carrier Mobility Spectra of Spray Electrified Liquids", *Physical Review*, 52(3), pp. 0184-0190.
 - (25) Chapman, S. (1938). "Interpretation of Carrier Mobility Spectra of Liquids Electrified by Bubbling and Spraying", *Physical Review*, 54(7), pp. 528-533.
 - (26) Dole, M.; Mack, L. L.; Hines, R. L. (1968). "Molecular Beams of Macroions", *Journal of Chemical Physics*, 49(5), pp. 2240-&.
 - (27) Whitehouse, C. M.; Dreyer, R. N.; Yamashita, M.; Fenn, J. B. (1985). "Electrospray Interface for Liquid Chromatographs and Mass Spectrometers", *Analytical Chemistry*, 57(3), pp. 675-679.
 - (28) Fenn, J. B.; Mann, M.; Meng, C. K.; Wong, S. F.; Whitehouse, C. M. (1989). "Electrospray Ionization for Mass-Spectrometry of Large Biomolecules", *Science*, 246(4926), pp. 64-71.
 - (29) Fenn, J. B.; Mann, M.; Meng, C. K.; Wong, S. F.; Whitehouse, C. M. (1990). "Electrospray Ionization-Principles and Practice", *Mass Spectrometry Reviews*, 9(1), pp. 37-70.
 - (30) Aleksandrov, M. L.; Gall, L. N.; Krasnov, N. V.; Nikolaev, V. I.; Pavlenko, V. A.; Shkurov, V. A.; Baram, G. I.; Grachev, M. A.; Knorre, V. D.; Kusner, Y. S. (1984). "Direct Coupling of a Microcolumn Liquid Chromatograph and a Mass-Spectrometer", *Bioorganicheskaya Khimiya*, 10(5), pp. 710-712.
 - (31) Aleksandrov, M. L.; Gall, L. N.; Krasnov, N. V.; Nikolaev, V. I.; Pavlenko, V. A.; Shkurov, V. A. (1984). "Mechanism of Ion Formation During the Electrohydrodynamic Sputtering of a Liquid into a Vacuum", *Journal of Analytical Chemistry of the Ussr*, 39(9), pp. 1268-1274.
 - (32) Aleksandrov, M. L.; Gall, L. N.; Krasnov, N. V.; Nikolaev, V. I.; Shkurov, V. A. (1985). "Mass-Spectrometric Analysis of Thermally Unstable Compounds of Low Volatility by the Extraction of Ions from Solution at Atmospheric-Pressure", *Journal of Analytical Chemistry of the Ussr*, 40(9), pp. 1227-1236.
 - (33) Taylor, G. (1964). "Disintegration of Water Drops in an Electric Field", *Proceedings of the Royal Society of London. Series A, Mathematical and Physical Sciences*, 280 pp. 383-397
 - (34) Meng, C. K.; Mann, M.; Fenn, J. B. (1988). *Proceedings of the 36th ASMS Conference on Mass Spectrometry and Allied Topics, June 5-10, San Francisco, CA* pp. 771-772.

- (35) Thomson, B. A.; Iribarne, J. V. (1979). "Field-Induced Ion Evaporation from Liquid Surfaces at Atmospheric-Pressure", *Journal of Chemical Physics*, 71(11), pp. 4451-4463.
- (36) Karas, M.; Bahr, U.; Dulcks, T. (2000). "Nano-Electrospray Ionization Mass Spectrometry: Addressing Analytical Problems Beyond Routine", *Fresenius Journal of Analytical Chemistry*, 366(6-7), pp. 669-676.
- (37) Graham, T. T. G.; Samuel, M. M.; Richard, D. O. (2009). "Nanoelectrospray Emitters: Trends and Perspective", *Mass Spectrometry Reviews*, 28(6), pp. 918-936.
- (38) Khayamian, T.; Jafari, M. T. (2007). "Design for Electrospray Ionization-Ion Mobility Spectrometry", *Analytical Chemistry*, 79(8), pp. 3199-3205.
- (39) Bramwell, C. J.; Colgrave, M. L.; Creaser, C. S.; Dennis, R. (2002). "Development and Evaluation of a Nano-Electrospray Ionisation Source for Atmospheric Pressure Ion Mobility Spectrometry", *Analyst*, 127(11), pp. 1467-1470.
- (40) Colgrave, M. L.; Bramwell, C. J.; Creaser, C. S. (2003). "Nanoelectrospray Ion Mobility Spectrometry and Ion Trap Mass Spectrometry Studies of the Non-Covalent Complexes of Amino Acids and Peptides with Polyethers", *International Journal of Mass Spectrometry*, 229(3), pp. 209-216.
- (41) Wu, C.; Siems, W. F.; Asbury, G. R.; Hill, H. H. (1998). "Electrospray Ionization High-Resolution Ion Mobility Spectrometry - Mass Spectrometry", *Analytical Chemistry*, 70(23), pp. 4929-4938.
- (42) Dugourd, P.; Hudgins, R. R.; Clemmer, D. E.; Jarrold, M. F. (1997). "High-Resolution Ion Mobility Measurements", *Review of Scientific Instruments*, 68(2), pp. 1122-1129.
- (43) Merenbloom, S. I.; Glaskin, R. S.; Henson, Z. B.; Clemmer, D. E. (2009). "High-Resolution Ion Cyclotron Mobility Spectrometry", *Analytical Chemistry*, 81(4), pp. 1482-1487.
- (44) Asbury, G. R.; Hill, H. H. (2000). "Using Different Drift Cases to Change Separation Factors (Alpha) in Ion Mobility Spectrometry", *Analytical Chemistry*, 72(3), pp. 580-584.
- (45) Hagen, D. F. (1979). "Characterization of Isomeric Compounds by Gas and Plasma Chromatography", *Analytical Chemistry*, 51(7), pp. 870-874.
- (46) Wu, C.; Siems, W. F.; Klasmeier, J.; Hill, H. H. (2000). "Separation of Isomeric Peptides Using Electrospray Ionization/High-Resolution Ion Mobility Spectrometry", *Analytical Chemistry*, 72(2), pp. 391-395.

- (47) Clemmer, D. E.; Hudgins, R. R.; Jarrold, M. F. (1995). "Naked Protein Conformations - Cytochrome-C in the Gas-Phase", *Journal of the American Chemical Society*, 117(40), pp. 10141-10142.
- (48) Dwivedi, P.; Wu, C.; Matz, L. M.; Clowers, B. H.; Siems, W. F.; Hill, H. H. (2006). "Gas-Phase Chiral Separations by Ion Mobility Spectrometry", *Analytical Chemistry*, 78(24), pp. 8200-8206.
- (49) Ruotolo, B.; Verbeck, G. F.; Thomson, L. M.; Gillig, K. J.; Russell, D. H. (2002). "Observation of Conserved Solution-Phase Secondary Structure in Gas-Phase Tryptic Peptides", *Journal of the American Chemical Society*, 124 pp. 4214-4215.
- (50) Wyttenbach, T.; Paizs, B.; Barran, P.; Brechi, L.; Liu, D.; Suhai, S.; Wysocki, V. H.; Bowers, M. T. (2003). "The Effect of the Initial Water of Hydration on the Energetics, Structures, and H/D Exchange Mechanism of a Family of Pentapeptides: An Experimental and Theoretical Study", *Journal of the American Chemical Society*, 125(45), pp. 13768-13775.
- (51) Badman, E. R.; Hoaglund-Hyzer, C. S.; Clemmer, D. E. (2001). "Monitoring Structural Changes of Proteins in an Ion Trap over Similar to 10-200 Ms: Unfolding Transitions in Cytochrome C Ions", *Analytical Chemistry*, 73(24), pp. 6000-6007.
- (52) Barran, P. E.; Polfer, N. C.; Campopiano, D. J.; Clarke, D. J.; Langridge-Smith, P. R. R.; Langley, R. J.; Govan, J. R. W.; Maxwell, A.; Dorin, J. R.; Millar, R. P.; Bowers, M. T. (2005). "Is It Biologically Relevant to Measure the Structures of Small Peptides in the Gas-Phase?", *International Journal of Mass Spectrometry*, 240(3), pp. 273-284.
- (53) Clowers, B. H.; Dwivedi, P.; Steiner, W. E.; Hill, H. H.; Bendiak, B. (2005). "Separation of Sodiated Isobaric Disaccharides and Trisaccharides Using Electrospray Ionization-Atmospheric Pressure Ion Mobility-Time of Flight Mass Spectrometry", *Journal of the American Society for Mass Spectrometry*, 16(5), pp. 660-669.
- (54) Liu, X. Y.; Valentine, S. J.; Plasencia, M. D.; Trimpin, S.; Naylor, S.; Clemmer, D. E. (2007). "Mapping the Human Plasma Proteome by Scx-Lc-IMS-Ms", *Journal of the American Society for Mass Spectrometry*, 18(7), pp. 1249-1264.
- (55) Valentine, S. J.; Plasencia, M. D.; Liu, X. Y.; Krishnan, M.; Naylor, S.; Udseth, H. R.; Smith, R. D.; Clemmer, D. E. (2006). "Toward Plasma Proteome Profiling with Ion Mobility-Mass Spectrometry", *Journal of Proteome Research*, 5(11), pp. 2977-2984.
- (56) McLean, J. A.; Ruotolo, B. T.; Gillig, K. J.; Russell, D. H. (2005). "Ion Mobility-Mass Spectrometry: A New Paradigm for Proteomics", *International Journal of Mass Spectrometry*, 240(3), pp. 301-315.

- (57) Dwivedi, P.; Wu, P.; Klopsch, S. J.; Puzon, G. J.; Xun, L.; Hill, H. H. (2008). "Metabolic Profiling by Ion Mobility Mass Spectrometry (Imms)", *Metabolomics*, 4(1), pp. 63-80.
- (58) Kanu, A. B.; Dwivedi, P.; Tam, M.; Matz, L.; Hill, H. H. (2008). "Ion Mobility-Mass Spectrometry", *Journal of Mass Spectrometry*, 43(1), pp. 1-22.
- (59) Grob, R. L. *Modern Practice of Gas Chromatography, 3rd ed.*; Wiley, New York, 1995.
- (60) Matz, L. M.; Hill, H. H. (2002). "Evaluating the Separation of Amphetamines by Electrospray Ionization Ion Mobility Spectrometry/Ms and Charge Competition within the Esi Process", *Analytical Chemistry*, 74(2), pp. 420-427.
- (61) Hall, G.; Dolan, J. W. (2002). "Performance Qualification of Lc Systems", *LCGC North America*, 20(9), pp. 842-+.
- (62) Rokushika, S.; Hatano, H.; Baim, M. A.; Hill, H. H. (1985). "Resolution Measurement for Ion Mobility Spectrometry", *Analytical Chemistry*, 57(9), pp. 1902-1907.
- (63) Siems, W. F.; Wu, C.; Tarver, E. E.; Hill, H. H.; Larsen, P. R.; McMinn, D. G. (1994). "Measuring the Resolving Power of Ion Mobility Spectrometers", *Analytical Chemistry*, 66(23), pp. 4195-4201.
- (64) Carrico, J. P.; Sickenberger, D. W.; Spangler, G. E.; Vora, K. N. (1983). "Simple Electrode Design for Ion Mobility Spectrometer", *Journal of Physics E. Scientific Instruments*, 16(11), pp. 1058-1062.
- (65) Spangler, G. E.; Vora, K. N.; Carrico, J. P. (1986). "Miniature Ion Mobility Spectrometer Cell", *Journal of Physics E. Scientific Instruments*, 19(3), pp. 191-198.
- (66) Bradbury, N. E.; Nielsen, R. A. (1936). "Absolute Values of the Electron Mobility in Hydrogen", *Physical Review*, 49(5), pp. 388.
- (67) Spangler, G. E.; Collins, C. I. (1975). "Peak Shape Analysis and Plate Theory for Plasma Chromatography", *Analytical Chemistry*, 47(3), pp. 403-407.
- (68) Xu, J.; Whitten, W. B.; Ramsey, J. M. (2000). "Space Charge Effects on Resolution in a Miniature Ion Mobility Spectrometer", *Analytical Chemistry*, 72(23), pp. 5787-5791.
- (69) Eiceman, G. A.; Vandiver, V. J.; Chen, T.; Ricomartinez, G. (1989). "Electrical Parameters in Drift Tubes for Ion Mobility Spectrometry", *Analytical Instrumentation*, 18(3-4), pp. 227-242.

- (70) Dahl, D. A.; McJunkin, T. R.; Scott, J. R. (2007). "Comparison of Ion Trajectories in Vacuum and Viscous Environments Using Simion: Insights for Instrument Design", *International Journal of Mass Spectrometry*, 266(1-3), pp. 156-165.
- (71) Lai, H.; McJunkin, T. R.; Miller, C. J.; Scott, J. R.; Almirall, J. R. (2008). "The Predictive Power of Simion/Sds Simulation Software for Modeling Ion Mobility Spectrometry Instruments", *International Journal of Mass Spectrometry*, 276(1), pp. 1-8.
- (72) Puton, J.; Knap, A.; Siodlowski, B. (2008). "Modelling of Penetration of Ions through a Shutter Grid in Ion Mobility Spectrometers", *Sensors and Actuators, B: Chemical*, 135(1), pp. 116-121.
- (73) Tadjimukhamedov, F. K.; Puton, J.; Stone, J. A.; Eiceman, G. A. (2009). "A Study of the Performance of an Ion Shutter for Drift Tubes in Atmospheric Pressure Ion Mobility Spectrometry: Computer Models and Experimental Findings", *Review of Scientific Instruments*, 80(10), pp. -.
- (74) Moseley, J. T.; Snuggs, R. M.; Martin, D. W.; Mcdaniel, E. W.; Miller, T. M. (1969). "Mobilities and Longitudinal Diffusion Coefficients of Mass-Identified Nitrogen and Potassium Ions in Nitrogen", *Bulletin of the American Physical Society*, 14(2), pp. 264-&.
- (75) Moseley, J. T.; Snuggs, R. M.; Martin, D. W.; Mcdaniel, E. W. (1969). "Mobilities Diffusion Coefficients and Reaction Rates of Mass-Identified Nitrogen Ions in Nitrogen", *Physical Review*, 178(1), pp. 240-&.
- (76) Mason, E. A.; Mcdaniel, E. W. *Transport Properties of Ions in Gases*; Wiley: New York, 1988.
- (77) Spangler, G. E. (1992). "Space-Charge Effects in Ion Mobility Spectrometry", *Analytical Chemistry*, 64(11), pp. 1312-1312.
- (78) Eiceman, G. A.; Nazarov, E. G.; Rodriguez, J. E.; Stone, J. A. (2001). "Analysis of a Drift Tube at Ambient Pressure: Models and Precise Measurements in Ion Mobility Spectrometry", *Review of Scientific Instruments*, 72(9), pp. 3610-3621.
- (79) Tolmachev, A. V.; Clowers, B. H.; Belov, M. E.; Smith, R. D. (2009). "Coulombic Effects in Ion Mobility Spectrometry", *Analytical Chemistry*, 81(12), pp. 4778-4787.
- (80) Graham, E.; James, D. R.; Kever, W. C.; Albritto, D.I.; Mcdaniel, E. W. (1973). "Mobilities and Longitudinal Diffusion-Coefficients of Mass-Identified Hydrogen-Ions in H₂ and Deuterium Ions in D₂ Gas", *Journal of Chemical Physics*, 59(7), pp. 3477-3481.
- (81) Rusyniak, M. J.; Ibrahim, Y. M.; Wright, D. L.; Khanna, S. N.; El-Shall, M. S. (2003). "Gas-Phase Ion Mobilities and Structures of Benzene Cluster Cations

(C₆H₆)N(+), N=2-6", *Journal of the American Chemical Society*, 125(39), pp. 12001-12013.

- (82) Rusyniak, M.; Ibrahim, Y.; Alsharaeh, E.; Meot-Ner, M.; El-Shall, M. S. (2003). "Mass-Selected Ion Mobility Studies of the Isomerization of the Benzene Radical Cation and Binding Energy of the Benzene Dimer Cation. Separation of Isomeric Ions by Dimer Formation", *Journal of Physical Chemistry A*, 107(38), pp. 7656-7666.
- (83) Creaser, C. S.; Benyazzar, M.; Griffiths, J. R.; Stygall, J. W. (2000). "A Tandem Ion Trap/Ion Mobility Spectrometer", *Analytical Chemistry*, 72(13), pp. 2724-2729.
- (84) Zhao, Q.; Soyk, M. W.; Schieffer, G. M.; Fuhrer, K.; Gonin, M. M.; Houk, R. S.; Badman, E. R. (2009). "An Ion Trap-Ion Mobility-Time of Flight Mass Spectrometer with Three Ion Sources for Ion/Ion Reactions", *Journal of the American Society for Mass Spectrometry*, 20(8), pp. 1549-1561.
- (85) Bagal, D.; Zhang, H.; Schnier, P. D. (2008). "Gas-Phase Proton-Transfer Chemistry Coupled with ToF Mass Spectrometry and Ion Mobility-MS for the Facile Analysis of Poly(Ethylene Glycols) and Pegylated Polypeptide Conjugates", *Analytical Chemistry*, 80(7), pp. 2408-2418.
- (86) Buryakov, I. A.; Kolomiets, Y. N. (2003). "Rapid Determination of Explosives and Narcotics Using a Multicapillary-Column Gas Chromatograph and an Ion-Mobility Spectrometer", *Journal of Analytical Chemistry*, 58(10), pp. 944-950.
- (87) Oxley, J. C.; Smith, J. L.; Kirschenbaum, L. J.; Marimnganti, S.; Vadlamannati, S. (2008). "Detection of Explosives in Hair Using Ion Mobility Spectrometry", *Journal of Forensic Sciences*, 53(3), pp. 690-693.
- (88) Tarver, E. E. (2004). "External Second Gate, Fourier Transform Ion Mobility Spectrometry: Parametric Optimization for Detection of Weapons of Mass Destruction", *Sensors*, 4(1-3), pp. 1-13.
- (89) Budimir, N.; Weston, D. J.; Creaser, C. S. (2007). "Analysis of Pharmaceutical Formulations Using Atmospheric Pressure Ion Mobility Spectrometry Combined with Liquid Chromatography and Nano-Electrospray Ionisation", *Analyst*, 132 pp. 34-40.
- (90) Harry, E. L.; Reynolds, J. C.; Bristow, A. W. T.; Wilson, I. D.; Creaser, C. S. (2009). "Direct Analysis of Pharmaceutical Formulations from Non-Bonded Reversed-Phase Thin-Layer Chromatography Plates by Desorption Electrospray Ionisation Ion Mobility Mass Spectrometry", *Rapid Communications in Mass Spectrometry*, 23(17), pp. 2597-2604.
- (91) Rezaei, B.; Jafari, M. T.; Khademi, R. (2009). "Selective Separation and Determination of Primidone in Pharmaceutical and Human Serum Samples Using

Molecular Imprinted Polymer-Electrospray Ionization Ion Mobility Spectrometry (Mip-Esi-IMS)", *Talanta*, 79(3), pp. 669-675.

- (92) Rezaei, B.; Mallakpour, S.; Majidi, N. (2009). "Solid-Phase Molecularly Imprinted Pre-Concentration and Spectrophotometric Determination of Isoxicam in Pharmaceuticals and Human Serum", *Talanta*, 78(2), pp. 418-423.
- (93) Creaser, C. S.; Griffiths, J. R.; Bramwell, C. J.; Noreen, S.; Hill, C. A.; Thomas, C. L. P. (2004). "Ion Mobility Spectrometry: A Review. Part 1. Structural Analysis by Mobility Measurement", *Analyst*, 129(11), pp. 984-994.
- (94) Matz, L. M.; Dion, H. M.; Hill, H. H. (2002). "Evaluation of Capillary Liquid Chromatography-Electrospray Ionization Ion Mobility Spectrometry with Mass Spectrometry Detection", *Journal of Chromatography A*, 946(1-2), pp. 59-68.
- (95) Bruins, A. P. (1991). "Mass-Spectrometry with Ion Sources Operating at Atmospheric-Pressure", *Mass Spectrometry Reviews*, 10(1), pp. 53-77.
- (96) Huang, E. C.; Wachs, T.; Conboy, J. J.; Henion, J. D. (1990). "Atmospheric-Pressure Ionization Mass-Spectrometry - Detection for the Separation Sciences", *Analytical Chemistry*, 62(13), pp. A713-&.
- (97) Collins, D. C.; Lee, M. L. (2002). "Developments in Ion Mobility Spectrometry-Mass Spectrometry", *Analytical and Bioanalytical Chemistry*, 372(1), pp. 66-73.
- (98) Tyndall, A. M. *The Mobility of Positive Ions in Gases*; University Press: Cambridge [Eng.], 1938.
- (99) Henderson, S. C.; Valentine, S. J.; Counterman, A. E.; Clemmer, D. E. (1999). "Esi/Ion Trap/Ion Mobility/Time-of-Flight Mass Spectrometry for Rapid and Sensitive Analysis of Biomolecular Mixtures", *Analytical Chemistry*, 71(2), pp. 291-301.
- (100) Myung, S.; Lee, Y. J.; Moon, M. H.; Taraszka, J. A.; Sowell, R.; Koeniger, S.; Hilderbrand, A. E.; Valentine, S. J.; Cherbas, L.; Cherbas, P.; Kaufmann, T. C.; Miller, D. F.; Mechref, Y.; Novotny, M. V.; Ewing, M. A.; Sporleder, C. R.; Clemmer, D. E. (2003). "Development of High-Sensitivity Ion Trap Ion Mobility Spectrometry Time-of-Flight Techniques: A High-Throughput Nano-Lc-IMS-Tof Separation of Peptides Arising from a Drosophila Protein Extract", *Analytical Chemistry*, 75(19), pp. 5137-5145.
- (101) Wytttenbach, T.; Kemper, P. R.; Bowers, M. T. (2001). "Design of a New Electrospray Ion Mobility Mass Spectrometer", *International Journal of Mass Spectrometry*, 212(1-3), pp. 13-23.
- (102) Clowers, B. H.; Siems, W. F.; Hill, H. H.; Massick, S. M. (2006). "Hadamard Transform Ion Mobility Spectrometry", *Analytical Chemistry*, 78(1), pp. 44-51.

- (103) Szumlas, A. W.; Ray, S. J.; Hieftje, G. M. (2006). "Hadamard Transform Ion Mobility Spectrometry", *Analytical Chemistry*, 78(13), pp. 4474-4481.
- (104) Knorr, F. J.; Eatherton, R. L.; Siems, W. F.; Hill, H. H. (1985). "Fourier-Transform Ion Mobility Spectrometry", *Analytical Chemistry*, 57(2), pp. 402-406.
- (105) Zimmermann, S.; Abel, N.; Baether, W.; Barth, S. (2007). "An Ion-Focusing Aspiration Condenser as an Ion Mobility Spectrometer", *Sensors and Actuators B: Chemical*, 125(2), pp. 428-434.
- (106) Sacristan, E.; Solis, A. A. (1998). "A Swept-Field Aspiration Condenser as an Ion-Mobility Spectrometer", *Ieee Transactions on Instrumentation and Measurement*, 47(3), pp. 769-775.
- (107) Solis, A. A.; Sacristan, E. (2006). "Designing the Measurement Cell of a Swept-Field Differential Aspiration Condenser", *Revista Mexicana De Fisica*, 52(4), pp. 322-328.
- (108) Tammet, H.; Mirme, A.; Tamm, E. (2002). "Electrical Aerosol Spectrometer of Tartu University", *Atmospheric Research*, 62(3-4), pp. 315-324.
- (109) Guevremont, R. (2004). "High-Field Asymmetric Waveform Ion Mobility Spectrometry: A New Tool for Mass Spectrometry", *Journal of Chromatography A*, 1058(1-2), pp. 3-19.
- (110) Buryakov, I. A.; Krylov, E. V.; Nazarov, E. G.; Rasulev, U. K. (1993). "A New Method of Separation of Multi-Atomic Ions by Mobility at Atmospheric-Pressure Using a High-Frequency Amplitude-Asymmetric Strong Electric-Field", *International Journal of Mass Spectrometry and Ion Processes*, 128(3), pp. 143-148.
- (111) Buryakov, I. A.; Krylov, E. V.; Makas, A. L.; Nazarov, E. G.; Pervukhin, V. V.; Rasulev, U. K. (1991). "Ion Division by Their Mobility in High Tension Alternating Electric-Field", *Pisma V Zhurnal Tekhnicheskoi Fiziki*, 17(12), pp. 60-65.
- (112) Krylov, E. V.; Nazarov, E. G.; Miller, R. A. (2007). "Differential Mobility Spectrometer: Model of Operation", *International Journal of Mass Spectrometry*, 266(1-3), pp. 76-85.
- (113) Shvartsburg, A. A. *Differential Ion Mobility Spectrometry - Nonlinear Ion Transport and Fundamentals of Faims*; CRC Press, Florida: Boca Raton, 2008.
- (114) Giles, K.; Pringle, S. D.; Worthington, K. R.; Little, D.; Wildgoose, J. L.; Bateman, R. H. (2004). "Applications of a Travelling Wave-Based Radio-Frequency-Only Stacked Ring Ion Guide", *Rapid Communications in Mass Spectrometry*, 18(20), pp. 2401-2414.

- (115) Wildgoose, J.; McKenna, T.; Hughes, C.; Giles, K.; Pringle, S.; Campuzano, I.; Langridge, J.; Bateman, R. H. (2006). "Using a Novel Travelling Wave Ion Mobility Device Coupled with a Time-of-Flight Mass Spectrometer for the Analysis of Intact Proteins", *Molecular & Cellular Proteomics*, 5(10), pp. S14-S14.
- (116) Pringle, S. D.; Giles, K.; Wildgoose, J. L.; Williams, J. P.; Slade, S. E.; Thalassinou, K.; Bateman, R. H.; Bowers, M. T.; Scrivens, J. H. (2007). "An Investigation of the Mobility Separation of Some Peptide and Protein Ions Using a New Hybrid Quadrupole/Travelling Wave IMS/Oa-ToF Instrument", *International Journal of Mass Spectrometry*, 261(1), pp. 1-12.
- (117) Ruotolo, B. T.; Giles, K.; Campuzano, I.; Sandercock, A. M.; Bateman, R. H.; Robinson, C. V. (2005). "Evidence for Macromolecular Protein Rings in the Absence of Bulk Water", *Science*, 310(5754), pp. 1658-1661.
- (118) Ruotolo, B. T.; Benesch, J. L. P.; Sandercock, A. M.; Hyung, S. J.; Robinson, C. V. (2008). "Ion Mobility-Mass Spectrometry Analysis of Large Protein Complexes", *Nature Protocols*, 3(7), pp. 1139-1152.
- (119) Smith, D. P.; Giles, K.; Bateman, R. H.; Radford, S. E.; Ashcroft, A. E. (2007). "Monitoring Copopulated Conformational States During Protein Folding Events Using Electrospray Ionization-Ion Mobility Spectrometry-Mass Spectrometry", *Journal of the American Society for Mass Spectrometry*, 18(12), pp. 2180-2190.
- (120) Riba-Garcia, I.; Giles, K.; Bateman, R. H.; Gaskell, S. J. (2008). "Evidence for Structural Variants of a- and B-Type Peptide Fragment Ions Using Combined Ion Mobility/Mass Spectrometry", *Journal of the American Society for Mass Spectrometry*, 19(4), pp. 609-613.
- (121) Vakhrushev, S. Y.; Langridge, J.; Campuzano, I.; Hughes, C.; Peter-Katlinic, J. (2008). "Ion Mobility Mass Spectrometry Analysis of Human Glycourinome", *Analytical Chemistry*, 80(7), pp. 2506-2513.
- (122) Laprade, B. N. (2004), *The 2004 Pittsburgh Conference on Analytical Chemistry and Applied Spectroscopy*, Chicago, IL, March 7-12,.
- (123) A Direct Comparison of a Resistive Glass and Stacked Ring Reflectron.
<http://www.photonis.com/data/cms-resources/File/new/Glass%20Reflectron%20-%20ASMS%202006.pdf>
- (124) Laprade, B. *Conductive Tube for Use as a Reflectron Lens*, 7,154,086,
- (125) Laprade, B. *Use of Conductive Glass Tubes to Create Electric Fields in Ion Mobility Spectrometers*, 7,081,618,

- (126) Verbeck, G. F.; Whitten, W. B.; Moxom, J. *Controlled Kinetic Energy Ion Source for Miniature Ion Trap and Related Spectroscopy System and Method*, App. 2006273251,
- (127) Collins, D. C.; Lee, M. L. (2001). "Electrospray Ionization Gas-Phase Electrophoresis under Ambient Conditions and Its Potential for High-Speed Separations", *Fresenius' Journal of Analytical Chemistry*, 369(3-4), pp. 225-233.
- (128) Thomas, R. C.; Bruce, A. T.; Bradley, B. S. (2009). "Atmospheric Pressure Ion Sources", *Mass Spectrometry Reviews*, 28(6), pp. 870-897.
- (129) Becker, C.; Fernandez-Lima, F. A.; Gillig, K. J.; Russell, W. K.; Cologna, S. M.; Russell, D. H. (2009). "A Novel Approach to Collision-Induced Dissociation (CID) for Ion Mobility-Mass Spectrometry Experiments", *Journal of the American Society for Mass Spectrometry*, 20(6), pp. 907-914.
- (130) Baker, E. S.; Clowers, B. H.; Li, F.; Tang, K.; Tolmachev, A. V.; Prior, D. C.; Belov, M. E.; Smith, R. D. (2007). "Ion Mobility Spectrometry-Mass Spectrometry Performance Using Electrodynamic Ion Funnel and Elevated Drift Gas Pressures", *Journal of the American Society for Mass Spectrometry*, 18(7), pp. 1176-1187.
- (131) Guo, Y.; Wang, J.; Javahery, G.; Thomson, B. A.; Siu, K. W. M. (2004). "Ion Mobility Spectrometer with Radial Collisional Focusing", *Analytical Chemistry*, 77(1), pp. 266-275.
- (132) Karasek, F. W.; Kim, S. H.; Rokushika, S. (1978). "Plasma Chromatography of Alkyl Amines", *Analytical Chemistry*, 50(14), pp. 2013-2016.
- (133) Kim, S. H.; Karasek, F. W.; Rokushika, S. (1978). "Plasma Chromatography with Ammonium Reactant Ions", *Analytical Chemistry*, 50(1), pp. 152-155.
- (134) Kim, S. H.; Betty, K. R.; Karasek, F. W. (1978). "Mobility Behavior and Composition of Hydrated Positive Reactant Ions in Plasma Chromatography with Nitrogen Carrier Gas", *Analytical Chemistry*, 50(14), pp. 2006-2012.
- (135) Karasek, F. W.; Kim, S. H.; Hill, H. H. (1976). "Mass Identified Mobility Spectra of P-Nitrophenol and Reactant Ions in Plasma Chromatography", *Analytical Chemistry*, 48(8), pp. 1133-1137.
- (136) Kambara, H.; Mitsui, Y.; Kanomata, I. (1979). "Identification of Clusters Produced in an Atmospheric-Pressure Ionization Process by a Collisional Dissociation Method", *Analytical Chemistry*, 51(9), pp. 1447-1452.
- (137) Kim, S. H.; Spangler, G. E. (1985). "Ion Mobility Spectrometry Mass-Spectrometry of 2 Structurally Different Ions Having Identical Ion Mass", *Analytical Chemistry*, 57(2), pp. 567-569.

- (138) Eiceman, G. A.; Shoff, D. B.; Harden, C. S.; Snyder, A. P. (1988). "Fragmentation of Butyl Acetate Isomers in the Drift Region of an Ion Mobility Spectrometer", *International Journal of Mass Spectrometry and Ion Processes*, 85(3), pp. 265-275.
- (139) Kojiro, D. R.; Cohen, M. J.; Stimac, R. M.; Wernlund, R. F.; Humphry, D. E.; Takeuchi, N. (1991). "Determination of C1-C4 Alkanes by Ion Mobility Spectrometry", *Analytical Chemistry*, 63(20), pp. 2295-2300.
- (140) Spangler, G. E. (2002). "Expanded Theory for the Resolving Power of a Linear Ion Mobility Spectrometer", *International Journal of Mass Spectrometry*, 220(3), pp. 399-418.
- (141) Tang, X. T.; Bruce, J. E.; Hill, H. H. (2006). "Characterizing Electrospray Ionization Using Atmospheric Pressure Ion Mobility Spectrometry", *Analytical Chemistry*, 78(22), pp. 7751-7760.
- (142) Gillig, K. J.; Ruotolo, B. T.; Stone, E. G.; Russell, D. H. (2004). "An Electrostatic Focusing Ion Guide for Ion Mobility-Mass Spectrometry", *International Journal of Mass Spectrometry*, 239(1), pp. 43-49.
- (143) Tang, K.; Shvartsburg, A. A.; Lee, H. N.; Prior, D. C.; Buschbach, M. A.; Li, F. M.; Tolmachev, A. V.; Anderson, G. A.; Smith, R. D. (2005). "High-Sensitivity Ion Mobility Spectrometry/Mass Spectrometry Using Electrodynamic Ion Funnel Interfaces", *Analytical Chemistry*, 77(10), pp. 3330-3339.
- (144) Harwit, M.; Sloane, N. J. A. *Hadamard Transform Optics*; Academic Press: New York, 1979.
- (145) Zare, R. N.; Fernandez, F. M.; Kimmel, J. R. (2003). "Hadamard Transform Time-of-Flight Mass Spectrometry: More Signal, More of the Time", *Angewandte Chemie-International Edition*, 42(1), pp. 30-35.
- (146) Busch, K. W.; Benton, L. D. (1983). "Multiplexed Methods in Atomic Spectroscopy", *Analytical Chemistry*, 55(3), pp. 445A - 460A.
- (147) Chester, T. L.; Winefordner, J. D. (1976). "Evaluation of the Analytical Capabilities of Frequency Modulated Sources in Multielement Non-Dispersive Flame Atomic Fluorescence Spectrometry", *Spectrochimica Acta*, 31B pp. 21-29.
- (148) Iwata, T.; Muneshige, A.; Araki, T. (2007). "Analysis of Data Obtained from a Frequency-Multiplexed Phase-Modulation Fluorometer Using an Autoregressive Model", *Applied Spectroscopy*, 61(9), pp. 950-955.
- (149) Dong, C.; Wen-Qing, L.; Yu-Jun, Z.; Jian-Guo, L.; Qing-Nong, W.; Rui-Feng, K.; Min, W.; Yi-Ben, C.; Jiu-Ying, C. (2006). "Modulation Frequency Multiplexed Tunable Diode Laser Spectroscopy System for Simultaneous Co, Co₂ Measurements", *Chinese Physics Letters*, 23(9), pp. 2446-2449.

- (150) Oh, D. B.; Paige, M. E.; Bomse, D. S. (1998). "Frequency Modulation Multiplexing for Simultaneous Detection of Multiple Gases by Use of Wavelength Modulation Spectroscopy with Diode Lasers", *Applied Optics*, 37(12), pp. 2499-2501.
- (151) Dave, D. P.; Akkin, T.; Milner, T. E.; Rylander III, H. G. (2001). "Phase-Sensitive Frequency-Multiplexed Optical Low-Coherence Reflectometry", *Optics Communications*, 193 pp. 39-43.
- (152) Zhang, J.; Yang, G.; Lee, Y. Z.; Chang, S.; Lu, J. P.; Zhou, O. (2006). "Multiplexing Radiography Using a Carbon Nanotube Based X-Ray Source", *Applied Physics Letters*, 89(6), pp. 064106/064101-064106/064103.
- (153) Al-Qaisi, M. K.; Akkin, T. (2008). "Polarization-Sensitive Optical Coherence Tomography Based on Polarization-Maintaining Fibers and Frequency Multiplexing", *Optics Express*, 16(17), pp. 13032-13041.
- (154) Oh, W. Y.; Yun, S. H.; Vakoc, B. J.; Shishko, M.; Desjardins, A.E., P.; B.H.; de Boer, J. F.; Tearney, G. J.; Bouma, B. E. (2008). "High-Speed Polarization Sensitive Optical Frequency Domain Imaging with Frequency Multiplexing", *Optics Express*, 16(2), pp. 1096-1103.
- (155) Takeda, M.; Gu, Q.; Kinoshita, M.; Takai, H.; Takahashi, Y. (1997). "Frequency-Multiplex Fourier-Transform Profilometry: A Single-Shot Three-Dimensional Shape Measurement of Objects with Large Height Discontinuities and/or Surface Isolations", *Applied Optics*, 36(22), pp. 5347-5354.
- (156) Liu, T.; Fernando, G. F. (2000). "A Frequency Division Multiplexed Low-Finesse Fiber Optic Fabry-Perot Sensor System for Strain and Displacement Measurements", *Review of Scientific Instruments*, 71(3), pp. 1275-1278.
- (157) Stern, A.; Javidi, B. (2003). "Three-Dimensional Image Sensing and Reconstruction with Time-Division Multiplexed Computational Integral Imaging", *Applied Optics*, 42(35), pp. 7036-7042.
- (158) Stern, A.; Javidi, B. (2005). "Information Capacity Gain by Time-Division Multiplexing in Three-Dimensional Integral Imaging", *Optics Letters*, 30(10), pp. 1135-1137.
- (159) Doriese, W. B.; Beall, J. A.; Deiker, S.; Duncan, W. D.; Ferreira, L.; Hilton, G. C.; Irwin, K. D.; Reintsema, C. D.; Ullom, J. N.; Vale, L. R.; Xu, Y. (2004). "Time-Division Multiplexing of High-Resolution X-Ray Microcalorimeters: Four Pixels and Beyond", *Applied Physics Letters*, 85(20), pp. 4762-4764.
- (160) Yong-Gang, Z.; Zhao-Bing, T.; Xiao-Jun, Z.; Yi, G.; Ai-Zhen, L.; Xiang-Rong, Z.; Yan-Lan, Z.; Sheng, L. (2007). "An Innovative Gas Sensor with on-Chip Reference Using Monolithic Twin Laser", *Chinese Physics Letters*, 24(10), pp. 2839-2841.

- (161) Cooper, D. J. F.; Smith, P. W. E. (2003). "Simple High-Performance Method for Larger-Scale Time Division Multiplexing of Fibre Bragg Grating Sensors", *Measurement Science and Technology*, 14 pp. 965-974.
- (162) Santini, R. E.; Milano, M. J.; Pardue, H. L. (1973). "Rapid Scanning Spectroscopy - Prelude to a New Era in Analytical Spectroscopy", *Analytical Chemistry*, 45(11), pp. 915A-927A.
- (163) Blaedel, W. J.; Boyer, S. L. (1973). "Programmable Monochromator for Accurate High-Speed Wavelength Isolation", *Analytical Chemistry*, 45(2), pp. 425-433.
- (164) Marshall, A. G.; Comisarow, M. B. (1975). "Fourier and Hadamard Methods in Spectroscopy", *Analytical Chemistry*, 47(4), pp. 491A-504A.
- (165) Fellgett, P. (1958). "Theory of Multiplex Interferometric Spectrometry", *Journal de Physique et al Radium*, 19 pp. 187-191.
- (166) Gross, M. L.; Remperl, D. L. (1984). "Fourier Transform Mass Spectrometry", *Science*, 226(4672), pp. 261-268.
- (167) Knorr, F. J.; Eatherton, R. L.; Siems, W. F.; Hill, H. H. (1985). "Fourier Transform Ion Mobility Spectrometry", *Analytical Chemistry*, 57(2), pp. 402-406.
- (168) Lenk, R.; Lucken, E. A. C. (1974). "Nuclear Quadrupole Resonance by Fourier Transform of the Free Induction Decay", *Pure and Applied Chemistry*, 40(1), pp. 199-299.
- (169) Gestblom, B.; Noreland, E. (1976). "Fourier Transform of Dielectric Time Domain Spectroscopy Data", *Journal of Physical Chemistry*, 80(14), pp. 1631-1634.
- (170) McGurk, J. C. (1974). "Transient Emission, Off-Resonant Transient Absorption, and Fourier Transform Microwave Spectroscopy", *Journal of Chemical Physics*, 61(9), pp. 3759-3767.
- (171) Farrar, T. C. (1970). "Pulsed and Fourier Transform Nmr Spectroscopy", *Analytical Chemistry*, 42(4), pp. 109A-112A.
- (172) Glick, M. R.; Jones, B. T.; Smith, B. W.; Winefordner, J. D. (1989). "Molecular Absorption Measurements by Ft/Us-Vis Spectrometry", *Applied Spectroscopy*, 43(2), pp. 342-344.
- (173) Habib, M. A.; Bockris, J. O. M. (1984). "Ft-Ir Spectrometry for the Solid/Soluion Interface", *Journal of Electroanalytical Chemistry*, 180(1-2), pp. 287-306.
- (174) Marshall, A. G. *Fourier, Hadamrad, and Hilbert Transforms in Chemistry*; Plenum Press: New York, 1982.

- (175) St. Louis, R. H.; Siems, W. F.; Hill, H. H. (1992). "Apodization Functions in Fourier-Transform Ion Mobility Spectrometry", *Analytical Chemistry*, 64(2), pp. 171-177.
- (176) Mariano, A. V.; Su, W.; Guharay, S. K. (2009). "Effect of Space Charge on Resolving Power and Ion Loss in Ion Mobility Spectrometry", *Analytical Chemistry*, 81 pp. 3385-3391.
- (177) Kimmel, J. R.; Fernandez, F. M.; Zare, R. M. (2003). "Effects of Modulation Defects on Hadamard Transform Time-of-Flight Mass Spectrometry (Ht-Tofms)", *Journal of the American Society of Mass Spectrometry*, 14 pp. 278-286.
- (178) Hudgens, J. W.; Bergeron, D. E. (2008). "A Hadamard Transform Electron Ionization Time-of-Flight Mass Spectrometer", *Review of Scientific Instruments*, 79(1), pp. 014102-014101 - 014102-014110.
- (179) Kwasnik, M.; Caramore, J.; Fernandez, F. M. (2009). "Digitally-Multiplexed Nanoelectrospray Ionization Atmospheric Pressure Drift Tube Ion Mobility Spectrometry", *Analytical Chemistry*, 81(4), pp. 1587-1594.
- (180) Decker Jr., J. A. (1972). "Hadamard-Transform Spectrometry. New Analytical Technique", *Analytical Chemistry*, 44(2), pp. 127A-134a.
- (181) Kaiser, R. (1974). "Application of the Hadamard Transform to Nmr Spectrometry with Pseudonoise Excitation", *Journal of Magnetic Resonance*, 15 pp. 44-63.
- (182) Treado, P. J.; Morris, M. D. (1990). "Multichannel Hadamard Transform Raman Microscopy", *Applied Spectroscopy*, 44(1), pp. 1-4.
- (183) Chen, G.; Mei, E.; Gu, W.; Zeng, X.; Zeng, Y. (1995). "Instrument for Hadamard Transform Three-Dimensional Fluorescence Microscope Image Analysis", *Analytical Chimica Acta*, 3000 pp. 261-267.
- (184) Kaneta, T.; Yamaguchi, Y.; Imasaka, T. (1999). "Hadamard Transform Capillary Electrophoresis", *Analytical Chemistry*, 71(23), pp. 5444-5446.
- (185) Lin, C. H.; Kaneta, T.; Chen, H. M.; Chen, W. X.; Chang, H. W.; Liu, J. T. (2008). "Applications of Hadamard Transform to Gas Chromatography/Mass Spectrometry and Liquid Chromatography/Mass Spectrometry", *Analytical Chemistry*, 80 pp. 5755-5759.
- (186) Brock, A.; Rodriguez, N.; Zare, R. N. (1998). "Hadamard Transform Time of Flight Mass Spectrometry", *Analytical Chemistry*, 70(18), pp. 3735-3741.
- (187) Brock, A.; Rodriguez, N.; Zare, R. N. (2000). "Characterization of a Hadamard Transform Time-of-Flight Mass Spectrometer", *Review of Scientific Instruments*, 71(3), pp. 1306-1318.

- (188) Fernandez, F. M.; Vadillo, J. M.; Kimmel, J. R.; Wetterhall, M.; Markides, K.; Rodriguez, N.; Zare, R. N. (2002). "Hadamard Transform Time-of-Flight Mass Spectrometry: A High-Speed Detector for Capillary-Format Separations", *Analytical Chemistry*, 74(7), pp. 1611-1617.
- (189) Trapp, O.; Kimmel, J. R.; Yoon, O. K.; Zuleta, I. A.; Fernandez, F. M.; Zare, R. N. (2004). "Continuous Two-Channel Time-of-Flight Mass Spectrometric Detection of Electrosprayed Ions", *Angewandte Chemie*, 43 pp. 6541-6544.
- (190) Zare, R. N.; Fernandez, F. W.; Kimmel, J. R. (2003). "Hadamard Transform Time-of-Flight Mass Spectrometry: More Signal, More of the Time", *Angewandte Chemie*, 42(1), pp. 30-35.
- (191) Tarver, E. E. (2004). "External Second Gate, Fourier Transform Ion Mobility Spectrometry: Parametric Optimization for Detection of Weapons of Mass Destruction.", *Sensors*, 4(1), pp. 1-13.
- (192) McLean, J. A.; Russell, D. H. (2005). "Multiplex Data Acquisition Based on Analyte Dispersion in Two Dimensions: More Signal More of the Time", *International Journal of Ion Mobility Spectrometry*, 8 pp. 66-71.
- (193) Henderson, S. C.; Valentine, S. J.; Counterman, A. E.; Clemmer, D. E. (1999). "Esi/Ion Trap/Ion Mobility/Time-of-Flight Mass Spectrometry for Rapid and Sensitive Analysis of Biomolecular Mixtures", *Analytical Chemistry*, 71(2), pp. 291-301.
- (194) Belov, M. E.; Clowers, B. H.; Prior, D. C.; Danielson, W. F.; Liyu, A. V.; Petritis, B. O.; Smith, R. D. (2008). "Dynamically Multiplexed Ion Mobility Time-of-Flight Mass Spectrometry", *Analytical Chemistry*, 80(15), pp. 5873-5883.
- (195) Belov, M. E.; Buschbach, M. A.; Prior, D. C.; Tang, K. Q.; Smith, R. D. (2007). "Multiplexed Ion Mobility Spectrometry-Orthogonal Time-of-Flight Mass Spectrometry", *Analytical Chemistry*, 79(6), pp. 2451-2462.
- (196) Clowers, B. H.; Belov, M. E.; Prior, D. C.; William, F. D.; Ibrahim, Y.; Smith, R. D. (2008). "Pseudorandom Sequence Modifications for Ion Mobility Orthogonal Time-of-Flight Mass Spectrometry", *Analytical Chemistry*, 80(7), pp. 2464-2473.
- (197) Belov, M. E.; Nikolaev, E. N.; Harkewicz, R.; Masselon, C. D.; Alving, K.; Smith, R. D. (2001). "Ion Discrimination During Ion Accumulation in a Quadrupole Interface External to a Fourier Transform Ion Cyclotron Resonance Mass Spectrometer", *International Journal of Mass Spectrometry*, 208(1-3), pp. 205-225.
- (198) Hanley, Q. S. (2001). "Masking, Photobleaching, and Spreading Effects in Hadamard Transform Imaging and Spectroscopy Systems", *Applied Spectroscopy*, 55(3), pp. 318-330.

- (199) Kimmel, J. R.; Fernandez, F. M.; Zare, R. N. (2003). "Effects of Modulation Defects on Hadamard Transform Time-of-Flight Mass Spectrometry (Ht-Tofms)", *Journal of the American Society for Mass Spectrometry*, 14(3), pp. 278-286.
- (200) Hudgens, J. W.; Bergeron, D. E. (2008). "A Hadamard Transform Electron Ionization Time-of-Flight Mass Spectrometer", *Review of Scientific Instruments*, 79(1), pp. -.
- (201) Kwasnik, M.; Fuhrer, K.; Gonin, M.; Barbeau, K.; Fernandez, F. M. (2007). "Performance, Resolving Power, and Radial Ion Distributions of a Prototype Nanoelectrospray Ionization Resistive Glass Atmospheric Pressure Ion Mobility Spectrometer", *Analytical Chemistry*, 79(20), pp. 7782-7791.
- (202) Watts, P.; Wilders, A. (1992). "On the Resolution Obtainable in Practical Ion Mobility Systems", *International Journal of Mass Spectrometry and Ion Processes*, 112(2-3), pp. 179-190.
- (203) Xu, J.; Whitten, W. B. (2008). "Monte Carlo Simulation of Ion Transport in Ion Mobility Spectrometry", *International Journal for Ion Mobility Spectrometry*, 11(1-4), pp. 13-17.
- (204) Kanu, A. B.; Gribb, M. M.; Hill, H. H. (2008). "Predicting Optimal Resolving Power for Ambient Pressure Ion Mobility Spectrometry", *Analytical Chemistry*, 80(17), pp. 6610-6619.
- (205) Hoaglund-Hyzer, C. S.; Valentine, S. J.; Sporleder, C. R.; Reilly, J. P.; Clemmer, D. E. (1998). "Three-Dimensional Ion Mobility Tofms Analysis of Electrosprayed Biomolecules", *Analytical Chemistry*, 70(11), pp. 2236-2242.
- (206) Steiner, W. E.; Clowers, B. H.; Fuhrer, K.; Gonin, M.; Matz, L. M.; Siems, W. F.; Schultz, A. J.; Hill, H. H. (2001). "Electrospray Ionization with Ambient Pressure Ion Mobility Separation and Mass Analysis by Orthogonal Time-of-Flight Mass Spectrometry", *Rapid Communications in Mass Spectrometry*, 15(23), pp. 2221-2226.
- (207) Moon, M. H.; Myung, S.; Plasencia, M.; Hilderbrand, A. E.; Clemmer, D. E. (2003). "Nanoflow Lc/Ion Mobility/Cid/Tof for Proteomics: Analysis of a Human Urinary Proteome", *Journal of Proteome Research*, 2(6), pp. 589-597.
- (208) McLean, J. A.; Russell, D. H. (2003). "Sub-Femtomole Peptide Detection in Ion Mobility-Time-of-Flight Mass Spectrometry Measurements", *Journal of Proteome Research*, 2(4), pp. 427-430.
- (209) Woods, A. S.; Ugarov, M.; Jackson, S. N.; Egan, T.; Wang, H. Y. J.; Murray, K. K.; Schultz, J. A. (2006). "Ir-Maldi-Ldi Combined with Ion Mobility Orthogonal Time-of-Flight Mass Spectrometry", *Journal of Proteome Research*, 5(6), pp. 1484-1487.

- (210) Ma, Y.; Liu, B. Y. H.; Lee, H. S.; Mauersberger, K.; Morton, J. **(1996)**. "High Sensitivity Mass Spectrometer System for Contaminant Measurement in High Purity Gases", *Review of Scientific Instruments*, 67(10), pp. 3465-3471.
- (211) Tabrizchi, M.; Jazan, E. **(2010)**. "Inverse Ion Mobility Spectrometry", *Analytical Chemistry*, 82(2), pp. 746-750.

LIST OF PUBLICATIONS

CHAPTER 2 & 3

M. Kwasnik, K. Fuhrer, M. Gonin, K. Barbeau, F. M. Fernández. “Performance, Resolving Power, and Radial Ion Distributions of a Prototype Nanoelectrospray Ionization Resistive Glass Atmospheric Pressure Ion Mobility Spectrometer” *Analytical Chemistry* (2007), 79(20), 7782-7791.

CHAPTER 4

M. Kwasnik, J. Caramore, F. M. Fernández. “Digitally-Multiplexed Nanoelectrospray Ionization Atmospheric Pressure Drift Tube Ion Mobility Spectrometry” *Analytical Chemistry* (2009), 81(4), 1587-1594.

CHAPTER 4

M. Kwasnik*, G. A. Harris*, F. M. Fernández, "Multiplexed Ion Mobility Spectrometry and Ion Mobility-Mass Spectrometry", in *Ion Mobility Spectroscopy - Mass Spectrometry: Theory and Applications*. **2009**, Accepted.

**Authors contributed equally to this work.*

CHAPTER 5

M. Kwasnik, F. M. Fernández. “Theoretical and Experimental Study of the Achievable Separation Power in Resistive-Glass Atmospheric Pressure Ion Mobility Spectrometry” *Rapid Communications in Mass Spectrometry* (Submitted).

VITA

MARK KWASNIK

Mark Kwasnik was born in Ft. Lauderdale, Florida. He attended public school in Boynton Beach, Florida before moving to Orlando, Florida where he received his two B.S. degrees, one in Chemistry and one in Forensic science, from the University of Central Florida in 2003. In 2004, he moved to Atlanta to pursue a Doctorate in Analytical Chemistry from the Georgia Institute of Technology. When he is not working on his research (rarely happens), Mr. Kwasnik enjoys watching movies, cooking, playing with his dog, hanging out with his wife, playing video games and taking apart and fixing computers.